2-day planetary waves in the stratosphere, mesosphere and lower thermosphere

Tunbridge, Victoria

Award date:
2011

Awarding institution:
University of Bath

2-Day Planetary Waves in the Stratosphere, Mesosphere & Lower Thermosphere

Victoria M. Tunbridge

A thesis submitted for the degree of Doctor of Philosophy
University of Bath
Department of Electronic and Electrical Engineering

February 2011

To Grandpa

Abstract

This thesis presents observations of the 2-day planetary wave in the stratosphere, mesosphere and lower thermosphere. These observations were made using two ground-based meteor radars at polar latitudes and the satellite-borne microwave limb sounder (MLS) on the NASA Aura satellite.

There have been relatively few observations of the 2-day wave at polar latitudes made using ground-based radars. This is particularly so in the Antarctic. Measurements of summertime and wintertime polar 2-day waves in the mesosphere and lower thermosphere (MLT) region were made using identical meteor radars at the conjugate geographical latitudes of Rothera (68°S, 68°W) in the Antarctic and Esrange (68°N, 21°E) in Arctic Sweden. This allows accurate quantification of the differences in the nature and seasonal variability of the 2-day wave between the two polar regions. A clear seasonal variability is evident with the maximum amplitudes occurring during the summer months in both hemispheres. However, significant differences are found in the behaviour of the summertime wave between the two polar regions. In particular, wave activity is shorter lived but of larger amplitude in the Antarctic. These differences are suggested to be partly due to the different background winds of the two polar regions and possible differences in the component zonal wavenumbers in the northern and southern hemispheres.

These radar studies have excellent spatial, height and time resolution but cannot resolve the component zonal wavenumbers of the 2-day wave. Therefore, Earth Observing System (EOS) Aura Microwave Limb Sounder (MLS) measurements of atmospheric temperature were used to investigate the climatology and interhemispheric differences of the different zonal wavenumbers (westward propagating zonal wavenumbers 2, 3 and 4) that compose the 2-day wave "complex". This study demonstrates that the wave is dominated by different wavenumbers in the northern and southern hemisphere and that some of the interhemispheric differences observed in ground-based studies can be explained by the seasonal variability of these different zonal wavenumbers.

These satellite studies led to participation in a multi-technique international collaboration to study the short-term variability of the summertime 2-day wave. Observations made in the northern hemisphere at mid-latitudes revealed that there are typically three peaks of enhanced 2-day wave amplitude during the summer, probably originating from a combination of baroclinic instability and critical wind speed.

Acknowledgements

I wish to thank all my colleagues in particular Charlie and Dave for all their support and patience in answering all my awkward questions. Also my supervisor, Nick Mitchell and express my gratitude for his help and advice throughout my DPhil. I also wish to thank Manuchehr for all the advice and assistance that was given over a cup of green tea.

As to my friends in Bath: Gemma, Zama and Helen each of you has helped me in the last few years and the time here would have felt endless without you. I wish to thank Gemma for being a dear friend and all her crazy looney fun; Zama who's friendship helped endure the daily office grind, all the sensible advice and being a great cinema buddy; to Helen for her kindness and for taking me under her wing when in the first few months.

Most importantly I wish to thank my family for their continued understanding and support. I would like to thank my parents for believing that this was always an achievable goal and just being there when needed. To little sister Gem, thanks for all the cake and coffee and care you have given me, especially in the last few months. It was a blessing to have you here in Bath. James I thank you for all your patience, care and understanding for your fun loving spirit that always cheered me up, for making me laugh everyday and for supporting me throughout my DPhil.

Contents

List of Figures

List of Tables

List of Acronyms

AU Astronomical Unit

CALIPSO Cloud-Aerosol Lidar and Infrared Pathfinder Satellite

CIRA COSPAR International Reference Atmosphere

cpd cycles per day

EOS Earth Observing System

FFTs Fast Fourier transforms

FOV Field of view

GCM Global Circulation Model

GCOM-W1 Global Change Observation Mission-Water

GPH Geopotential Height

GMAO Global Modelling and Assimilation Office

HRDI High Resolution Doppler Imager

ISR Incoherent Scatter

KMCM Kühlungsborn Mechanistic general Circulation Model

LIDAR LIght Detection And Ranging

LOS Line Of Sight

LT Local Time

MF Medium Frequency

MLT Mesosphere and Lower Thermosphere

MST Mesosphere-Stratosphere-Troposphere

MSIS-E90 Global atmospheric model MSIS-E90

MLS Microwave Limb Sounder

NASA National Aeronautics and Space Administration

PV Potential Vorticity

SCR Selective Chopper Radiometer

NLC Noctilucent Clouds

OCO Orbiting Carbon Observatory

OMI Ozone Monitoring Instrument

PARASOL Polarisation & Anisotropy of Reflectances for Atmospheric Sciences coupled with Observations from a Lidar

PMR Pressure Modulator Radiometer

PMSE Polar Mesospheric Summer Echoes

QBO Quasi-Biannual Oscillation

RADAR Radio Detection And Ranging

Rx Receiver antennae

SABER Sounding of the Atmosphere using Broadband Emission Radiometry

SCR Selective Chopper Radiometer

SKiYMET All-SKy interferometric METeor Radar

TES Tropospheric Emission Spectrometer

TIMED Thermosphere, Ionosphere, Mesosphere, Energetics and Dynamics

Tx Transmitter antennae

UARS Upper Atmosphere Research Satellite

UGAMP UK Universities Global Atmospheric Modelling Programme

UK United Kingdom

UTC Co-ordinated Universal Time

VHF Very High Frequency

WINDII Wind Imaging Interferometer

W2 Westward Propagating Zonal Wavenumber 3

W3 Westward Propagating Zonal Wavenumber 3

W4 Westward Propagating Zonal Wavenumber 4

E1 Eastward Propagating Zonal Wavenumber 1

E2 Eastward Propagating Zonal Wavenumber 2

E3 Eastward Propagating Zonal Wavenumber 3

List of Symbols

a	Earth's Radius
r_E	Radius of the Earth
d	Distance
h	True height
z	Height
g	Acceleration due to gravity
H	Scale height
m	Vertical wavenumber
k	Zonal wavenumber
t	Time
r	Range to the meteor
w	Vertical velocity
$\hat{\mathbf{k}}$	Unit vertical vector
l	Meridional wavenumber
$\overline{u(z)}$	Mean winds at a height, z
C	Speed of sound
c	Phase speed of a wave with respect to the ground
$\hat{c}$	Intrinsic phase speed
ω_b	Brunt-Väisälä frequency
ω	Wave frequency
Ω	The Earth's rotational angular velocity vector
f	Coriolis parameter of planetary vorticity
R_i	Richardson number
λ	Wavelength
α	Angle between the vector between a line drawn between a meteor and the ground and a line drawn between the meteor and the radar, see Figure 3.15
$\overline{u}$	Zonal mean wind
U_c	Rossby critical velocity
ζ	Relative vorticity
ϕ	Latitude
η	Absolute vorticity
Θ_n	Hough functions
ϵ_n	Eigenvalues of Laplace's tidal equation
h_n	Equivalent depth
V_{rad}	Radial velocity
V_h	Vertical velocity

Chapter 1

Structure and Dynamics of the Middle Atmosphere

1.1 Introduction

The atmosphere is a thin envelope of gas that encircles the planet. It is divided into concentric layers or *spheres* based on the sign of the temperature gradient. Each sphere is characterised by either a uniform increase or decrease in temperature with height. The top or boundary of each sphere is defined by a reversal in the temperature gradient and is known as a *pause*. These layers are illustrated in Figure 1.1

These different temperature gradients are mainly due to changing rates of solar heating from the absorption of ultraviolet (UV) radiation by ozone (O_3) and infrared cooling by emission of infrared (IR) radiation by carbon dioxide (CO_2) and water vapour (H_2O). These chemical species are concentrated at different heights in the atmosphere and hence dominate the absorption or radiation of energy at those heights. As an example Figure 1.2 shows the heating and cooling rates calculated for several different molecular species.

1.2 The Mesosphere and Lower Thermosphere

The Mesosphere and Lower Thermosphere (MLT) region is the region of the Earth's atmosphere that is at heights between about 50 and 100 km. This part of the atmosphere remains the least explored because it is one of the most difficult to study. This is because obtaining *in situ* measurements at these heights can be difficult and costly. Only in recent years have continuous measurements through remote sensing been possible by the use of ground-based and satellite instruments.

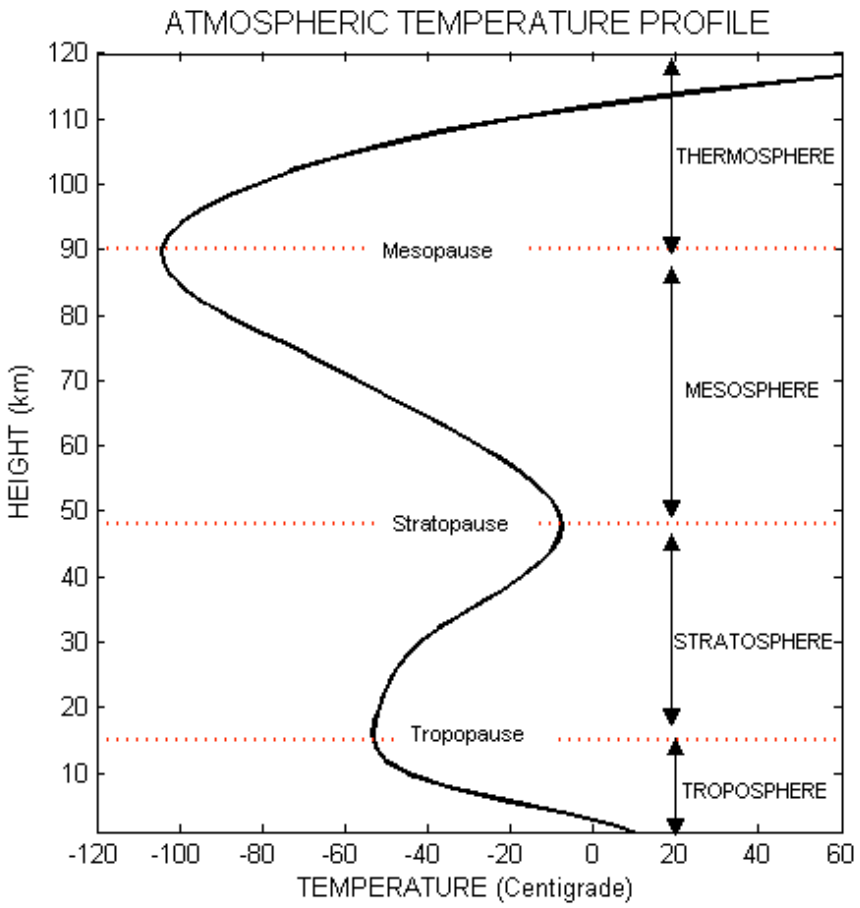

Figure 1.1: Atmospheric temperature profile from MSIS-E-90 Model for the 22^{nd} February conditions at a latitude of 68°N.

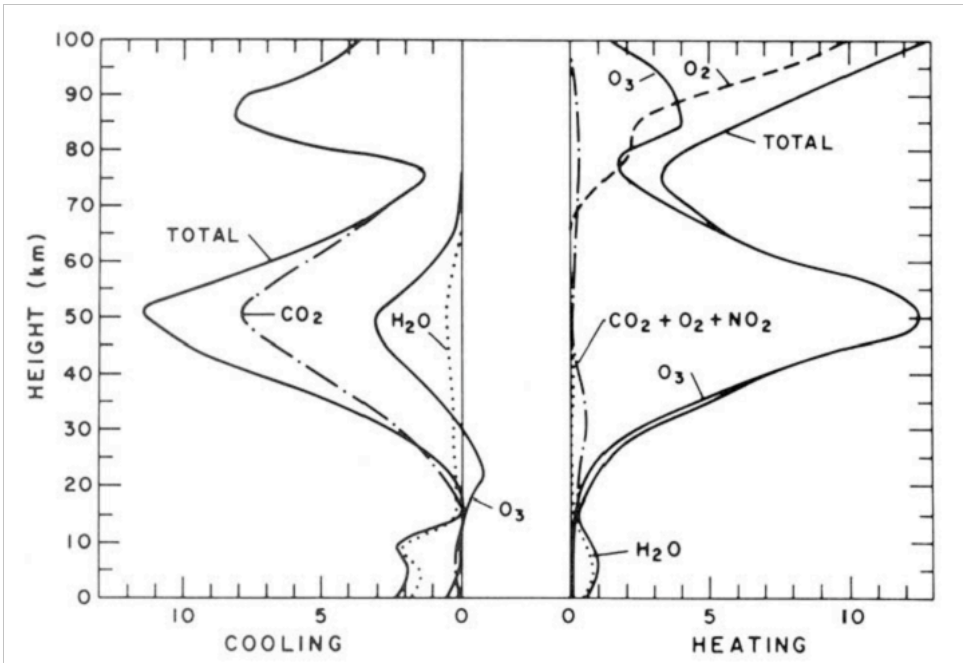

Figure 1.2: Heating and cooling rates (Kelvin) of the dominant chemical species in the Earth's atmosphere, after London (1980)

The MLT region is a host to many interesting and exotic physical phenomena. For example, the polar *summer* mesopause is the coldest naturally occurring place on the Earth at a temperature of about 130 K. These extremely cold temperatures can result in the formation of Polar Mesospheric Clouds (PMC) which can be observed from the ground as *Noctilucent clouds* (NLC). These are the highest clouds formed in the Earth's atmosphere. They can be illuminated from underneath when the Sun is below the horizon and so are seen at twilight. Polar Mesospheric Summer Echoes (PMSE) are strong radar echoes from the cold summer mesosphere at high latitudes. It is believed that nanometer sized charged particles (ice particles with radii from a few up to a few tens of nanometers) play a role in the occurrence of PMSE and that the layering of these ice-particles produces multiple PMSE layer structures. It is predicted by model investigations that the lower PMSE layers have the largest ice-particles which coincide with occurrences of NLCs (Hoffmann et al., 2003, 2005). Therefore, a connection exists between them and noctilucent clouds (e.g., Hoffmann et al., 1999; La Hoz et al., 2006). Airglow is also observed in this part of the atmosphere. Airglow is a photochemical luminescence or chemiluminescence that arises from chemical reactions in the upper atmosphere. These chemical reactions leave atoms in excited states from which they can radiate showing a layer of air that glows in the upper atmosphere at specific wavelengths. The most prominent being from molecular oxygen O_2, sodium Na and the hydroxyl radical OH. This causes the night sky to never be completely dark. Meteors also ablate in this part of the atmosphere and so this is the only part of the atmosphere where there is a direct influx of extra-terrestrial material. Meteors will be discussed in more depth in Chapter 3.

The dynamics of the MLT region are dominated by large-scale waves and tides that propagate up from below. As they propagate up through the atmosphere they interact with mean winds and other wave modes, dissipating their energy and momentum, which contributes to the wind and temperature field variability. The density in the atmosphere decreases exponentially with height. As the waves propagate upwards, energy per unit volume, is conserved in the absence of dissipation. This means that as the density of the atmosphere decreases the wave amplitude increases, producing large-amplitude waves in the MLT region. This means that small amplitude waves that are excited in the troposphere can grow to be very large as they ascend to the mesosphere. These waves can become unstable when their amplitude exceed particular instability thresholds and so they 'then' *break* transferring their energy and momentum into the mean flow. This 'dumping' of energy and momentum into this region drives the circulation in the MLT away from that predicted by radiative equilibrium alone and leads to the observed cold summer polar mesopause, as will be explained in Sections 1.3 - 1.6.

The MLT region can also be considered as a sensitive indicator of climate change where Thomas (1995) termed it the 'miners canary' of the atmosphere. This is because a signal of climate change (in terms of the change in global surface temperature) in the troposphere may be more difficult to identify, where the climate feedback processes are less understood,

than a temperature change signal occurring higher up where these feedback processes are less influential. For example, increasing carbon dioxide (CO_2) levels will have a small warming effect in the troposphere, but a much larger effect in the mesosphere. Modelling studies have suggested that a doubling in atmospheric CO_2 will result in a warming of the troposphere by $\sim$ 2-4 K and a cooling of the middle atmosphere by $\sim$ 10-12 K (Fomichev et al., 2007). This long-term cooling may be linked to the increase in numbers of noctilucent clouds observed over North-West Europe (Gadsden, 1997). Therefore, a better understanding of this region of the atmosphere is not only important in enabling us to understand the atmosphere as a whole, it is also a useful tool understanding the changes in the Earth's climate.

1.3 Radiative equilibrium and the predicted structure of the atmosphere

An atmosphere in radiative equilibrium will have no net heating or cooling and thus at all heights and latitudes the radiative heating and cooling rates must be in equilibrium. Therefore, the temperature has a steady-state structure. Knowledge of heating and cooling rates in the atmosphere (such as those shown in Figure 1.2) allow the calculation of the zonally-averaged latitudinal temperature structure of the atmosphere in this radiative equilibrium case. An example of this zonally-averaged temperature structure is shown in Figure 1.3 for solstice conditions (Geller, 1983).

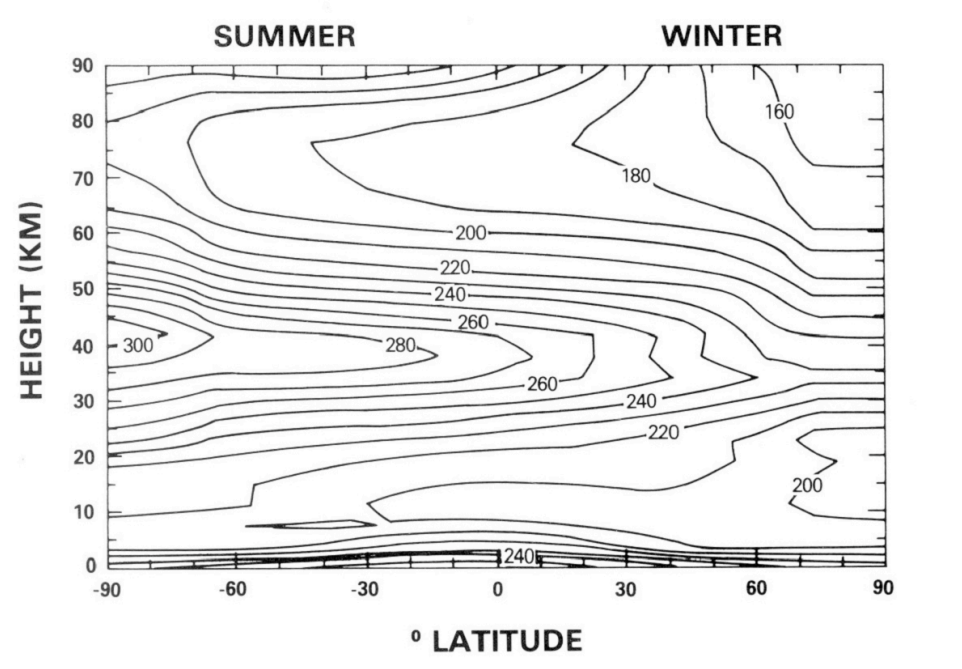

Figure 1.3: Calculated radiative equilibrium temperatures during solstice. Units are in Kelvin, after Geller (1983).

The figure shows that the temperature gradient in the stratosphere and mesosphere is from the warm summer pole to the cold winter pole. This is because the summer pole is in 24-hour sunlight and so is continually heated, whereas the winter pole is in continuous darkness and so has no solar heating at all.

The maximum temperatures occur at the stratopause at a height of $\sim$ 40 km. Here the summer polar temperatures reach $\sim$ 300 K and the the winter polar temperatures reach $\sim$ 220 K. This is expected since there is a higher concentration of ozone at these heights. The minimum temperatures of $\sim$ 160 K are predicted to occur at the mesopause over the winter pole.

The north-south temperature gradients produced by differential heating at the poles creates north-south pressure gradients, with high pressures at the summer pole and low pressures at the winter pole. This in turn produces flow in the atmosphere towards the winter pole. Because of the rotation of the Earth, as the air parcels move they will experience the *Coriolis force*. This force acts at right angles to the direction of the air parcels motion. The action from these two forces will create a steady-state circulation in the atmosphere and a *geostrophic wind* arises. Figure 1.4 presents a schematic diagram illustrating the forces acting on an air parcel and its resulting velocity for this geostrophic flow.

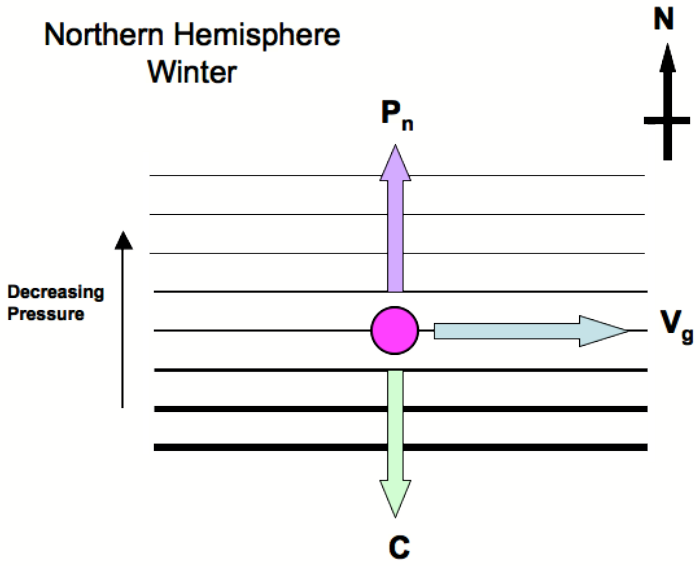

Figure 1.4: A schematic diagram illustrating the geostrophic balance of forces on an air parcel in the winter northern hemisphere. P_n is the pressure gradient, C is the Coriolis force and V_g is the resultant geostrophic velocity. The parallel horizontal lines represent isobars.

The Coriolis force pushes the flow to the right in the northern hemisphere and to the left in the southern hemisphere. Therefore, this results in westward geostrophic winds in the summer hemisphere and eastward geostrophic winds in the winter hemisphere. These geostrophic winds will thus be a non-accelerating flow in which there are no meridional or vertical winds.

Because of the horizontal temperature gradient, a vertical shear in the winds is created. From the radiative equilibrium temperature structure shown in Figure 1.3 and the *thermal wind equation*, which relates the vertical shear of the geostrophic flow to the horizontal temperature gradient, the geostrophic winds throughout the depth of the atmosphere can be calculated. This is shown in Figure 1.5. Note that the geostrophic winds cannot be determined from the thermal wind equation at the equator since the coriolis force tends to zero there and so geostrophic balance does not apply.

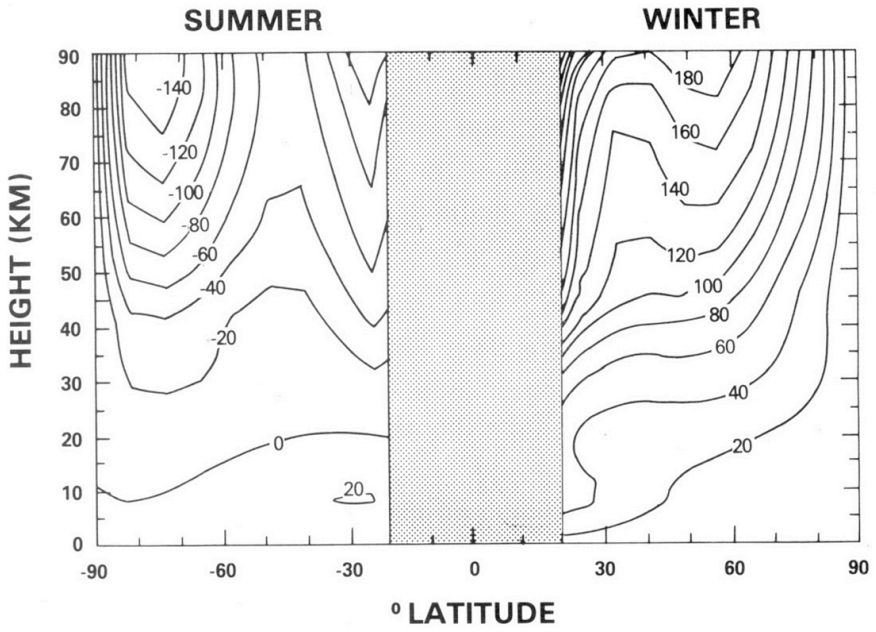

Figure 1.5: Geostrophic zonal-mean winds calculated from the radiative equilibrium temperatures shown in Figure 1.3. No predictions are made at the equator because of the near zero Coriolis force. Units are ms^{-1}. Eastward winds are positive and westward winds are negative. After Geller (1983).

Figure 1.5 shows that there are strong zonal winds throughout the atmosphere. In each hemisphere there is a zonal jet in which the zonal wind speed increases with increasing height. These jets are thus said to be 'open'. In the winter hemisphere there is a strong eastwards jet centred on $\sim 50^\circ$ latitude, in the summer hemisphere there is a jet centred on $\sim 75^\circ$ latitude, and these jets dominate the mesospheric flow. Note that under the conditions of radiative equilibrium, there are no vertical or meridional flows predicted.

1.4 The observed temperature structure and general circulation

The observed global circulation of the atmosphere is, in fact, very different to the predicted radiative equilibrium model described above in Section 1.3. Figure 1.6 presents a more realistic representation of the temperature profile of the atmosphere taken from the CIRA-86 model for solstice conditions.

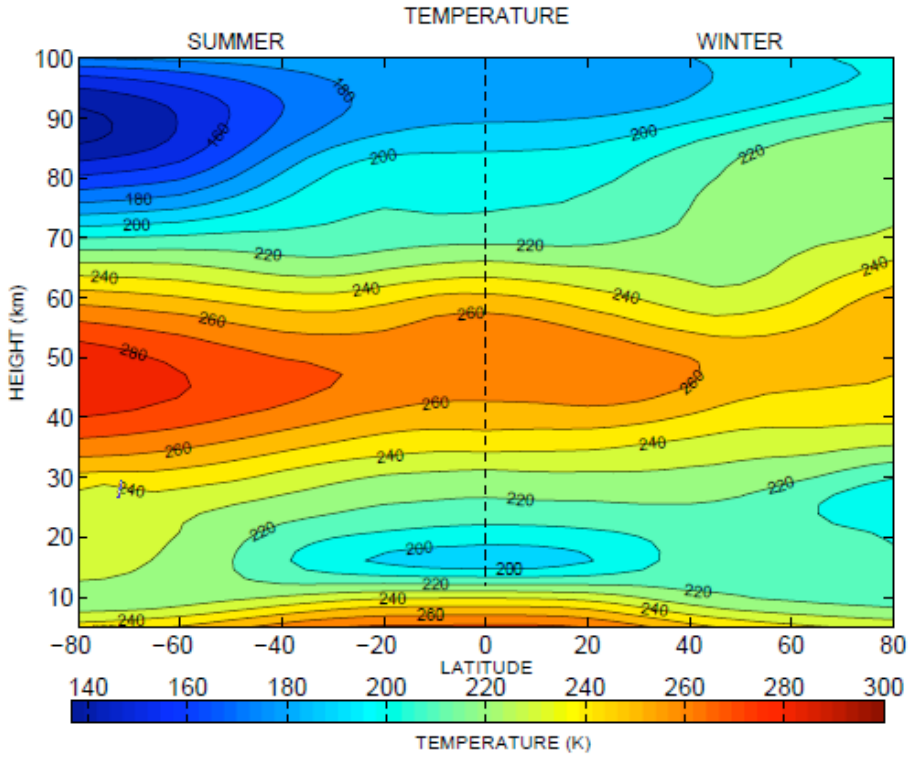

Figure 1.6: The zonally averaged temperature structure predicted by the CIRA-86 model for solstice conditions.

When these temperatures are compared to the predicted model temperatures in Figure 1.3 there are some striking differences. Firstly, above heights of $\sim$ 75 km the summer pole is no longer warmer than the winter pole. The temperature gradient observed for in the real atmosphere, is *reversed* compared to the model predictions so that the winter pole is now warmer than the summer pole. This is a counter-intuitive result.

Secondly, the predictions in a gradual increase in temperature from the winter to the summer pole at the tropopause is not observed. Instead there is a temperature minimum at the equatorial tropopause.

There are also significant differences in the zonal winds in the atmosphere compared to the predictions of radiative equilibrium model. Figure 1.7 presents zonally-averaged zonal winds taken from the CIRA-86 model for solstice conditions. At heights below $\sim$ 90 km, two pairs of jets are observed, one in the upper troposphere and one in the stratosphere/mesosphere. The tropospheric jets are both directed eastward. However, the mesospheric jets are directed westward in the summer hemisphere and eastwards in the winter hemisphere. This is seen in the radiative equilibrium model. However, unlike the radiative equilibrium model the mesospheric jets are 'closed' (i.e., their strength decreases with height) and they even reverse in direction above the mesopause at about 90 km.

The observed general circulation of the atmosphere is therefore in a state far removed from

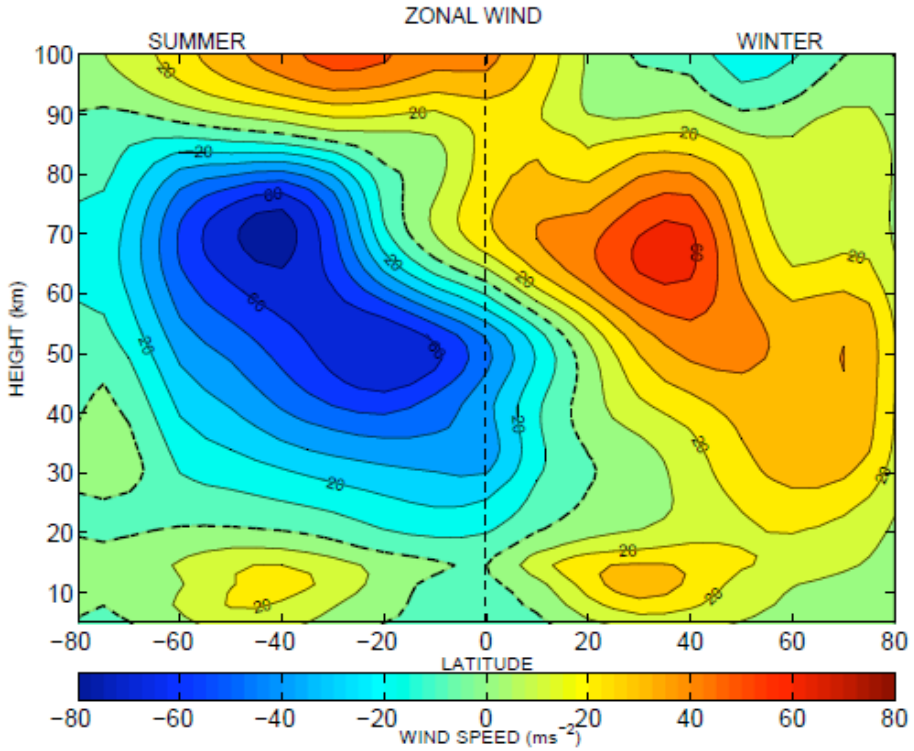

Figure 1.7: Zonal mean winds generated using the CIRA-86 model for solstice conditions. Negative (positive) values denote westward (eastward) winds.

that described by radiative equilibrium. To understand the origin of the differences observed, we must consider the effects of dynamical forcing of the atmosphere by atmospheric waves. In particular, we must consider the effect of the deposition of energy and momentum into the atmosphere by breaking waves.

1.5 Waves

Waves and tides are key driving forces of the observed dynamics of the middle atmosphere. They play a very important role in determining the observed temperature structure and winds in this region. The most dominant types of wave in the stratosphere mesosphere and lower thermosphere are gravity waves, tides and planetary waves.

Gravity waves are mesoscale oscillations with periods ranging from ~ 5 minutes up to many tens of hours (i.e., from the Brunt-Väisälä frequency to the inertial period). Their 'restoring force' is fluid buoyancy with an additional component from the Coriolis force which becomes more significant at lower periods. In the limiting case of the inertial period, the restoring force is purely the Coriolis force (Hoffmann et al., 2006). Therefore, gravity waves can only exist when the atmosphere is stably stratified. They are mostly generated in the troposphere

or lower stratosphere by sources that include convection, flow over topography, wind shear, unbalanced flows and frontal systems. They are believed to be an important mechanism for transporting energy and momentum into the middle atmosphere thus coupling together different layers of the atmosphere.

Both the Sun and the Moon produce tides in the atmosphere. These include both gravitationally excited tides and thermally excited tides. Tides are essentially forced, global-scale gravity waves with periods that are harmonics of a solar day, i.e., 6, 8, 12 and 24 hours. They are global-scale spherical harmonics with an integer number of wavelengths 'wrapped around' a circle of latitude. Thermal tides are excited by the diurnal heating of water vapour in the troposphere, ozone in the stratosphere and molecular oxygen and nitrogen in the thermosphere. These are known as solar tides. The primary generation of solar tides in the MLT region is from the solar heating of tropospheric and stratospheric water vapour and ozone.

Gravitational tides are forced by the Sun and Moon, the latter are known as lunar tides. Lunar tides have much smaller amplitudes than the thermal solar tides and they are mainly generated in the troposphere (Sandford et al., 2006; Sandford and Mitchell, 2007; Sandford et al., 2007). In the MLT region, atmospheric thermal solar tides are the largest-amplitude oscillation and the 12- and 24-hour tides can reach amplitudes of several tens of ms^{-1} and are capable of interacting strongly with other atmospheric waves.

Planetary waves are planetary-scale oscillations. They include the so-called normal modes that have discrete periods of ~ 2, ~ 4, ~ 5 and ~ 16 days. They extend coherently about a circle of latitude. They can be either stationary with respect to the Earth's surface or travelling, in which case they generally propagate westward with respect to the mean flow. The stationary waves are forced waves which are usually excited by flow over topography. Travelling planetary waves consist of free modes which may be generated by instabilities. The restoring force for planetary waves is the poleward gradient of planetary vorticity combined with the conservation of absolute vorticity. They are a dominant part of the dynamics of the stratosphere. The vertical propagation of planetary waves is very dependent on the mean zonal wind because planetary wave zonal phase speeds are often comparable to mean wind speeds, which promotes interaction. A consequence of this is that (as will be explained in Chapter 2) planetary waves generated in the summer troposphere/lower stratosphere are usually unable to propagate through the westwards stratospheric jet up to the MLT region. Hence, the planetary waves observed in the mesosphere in summer are most likely to have been generated *in situ*.

An important point about atmospheric waves is that they grow in amplitude exponentially as they ascend. The atmosphere is gravitationally bound to the Earth and therefore the

density decrease exponentially with altitude. This is shown in equation (1.1)

$$\rho = \rho_0 \exp \frac{-z}{H} \tag{1.1}$$

The rate of this decrease is determined by the *scale height*, H, which is the vertical height by which the pressure changes over a factor of e. This is determined by:

$$H = \frac{kT}{mg} \tag{1.2}$$

where k is the Boltzmann's constant, T is the temperature, m is the mean molecular mass and g is the acceleration due to gravity.

For waves travelling in the atmosphere, the kinetic energy per unit volume, E, is given by equation (1.3) where

$$E = \frac{1}{2}\rho A^2 \tag{1.3}$$

Where ρ is the density and A is the amplitude. In the absence of dissipation, this means that as the wave propagates vertically into regions of lower density, the amplitude of the wave must increase in order to conserve energy. The conservation of energy thus implies an exponential increase in wave amplitude with increasing height. This is given in equation (1.4)

$$A = A_0 \exp\left(\frac{z}{2H}\right) \tag{1.4}$$

where A_0 is the initial amplitude at a given initial height z_0. This implies that small waves of amplitude a few cms^{-1} generated in the troposphere can grow to be very large in the upper atmosphere with amplitudes of the order of tens ms^{-1} .

1.6 The effect of dynamic forcing on the middle atmosphere

The dynamics of the middle atmosphere are dominated by winds, waves and tides, which are all strongly coupled together. Gravity waves that are excited in the lower atmosphere, propagate upwards and grow in amplitude because of decreasing gas density. As they reach the middle atmosphere their amplitudes become so large that they generate instabilities and thus dissipate and deposit their energy and momentum into the atmosphere. The vertical propagation of gravity waves is affected by the background horizontal winds, in particular the zonal (East/West) background winds. During summer in the stratosphere the zonal winds are westward. Gravity waves with eastward phase speeds can propagate up to the MLT, whereas the westward waves cannot. The eastward waves can therefore dissipate in

the MLT region and here they deposit their eastward momentum. These waves thus cause the wind to become more eastward eventually reversing the direction of the zonal wind at a height of about 80 - 90 km. Likewise, during the winter when stratospheric winds are eastward, westward phase-speed gravity waves propagate to the MLT region and in turn reverse the wind direction there to become westward. This reversal in the direction of the zonal wind acts to close the mesospheric jets and reverse their direction at about 90 km, as is observed in the real atmosphere (see Figure 1.7). Figure 1.8 shows the zonal component of gravity wave drag deposited in the mesosphere. The peaks of the gravity wave drag are situated at heights of 80 - 90 km just where the mesospheric zonal jets close after Hoffmann et al. (2010).

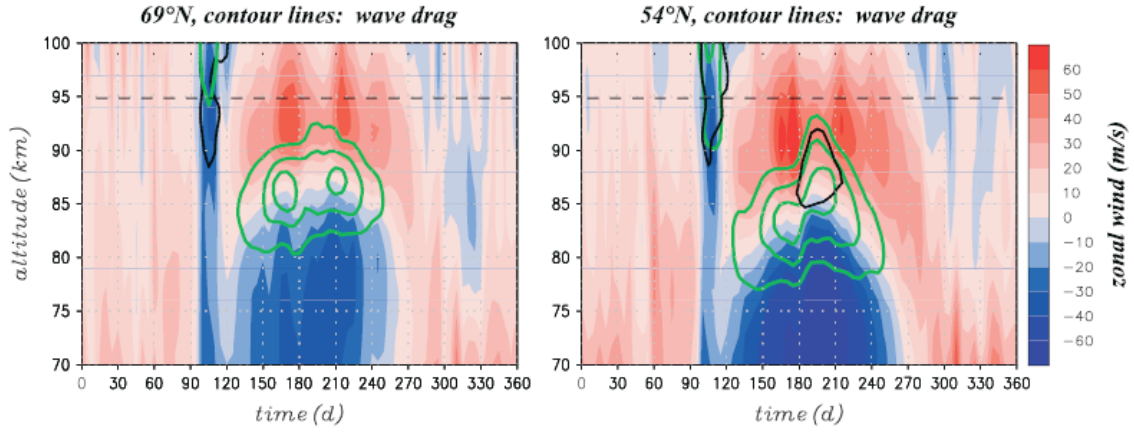

Figure 1.8: Mean zonal winds (coloured filled contours) and gravity wave drag (green contours: 50, 100, 150 $ms^{-1}d^{-1}$) at 69°N and 54°N from the simulation with the Kühlungsborn Mechanistic general Circulation Model (KMCM). In addition, the black lines show the -50 $ms^{-1}d^{-1}$ contour of the quasi-geostrophic wave drag that is cause by planetary Rossby waves. After Hoffmann et al. (2010).

The momentum deposition also acts with the pressure gradient and Coriolis forces to produce a pole-to-pole meridional circulation. The balance of forces that produce this steady state flow are shown in Figures 1.9 and 1.10. Because of the seasonal pattern in the zonal momentum deposition the meridional flow is directed from the summer pole to the winter pole. This results in a convergence of air over the winter pole and a divergence of air over the summer pole. To maintain continuity there must be vertical flows to replace the air lost at the summer pole and to remove the excess air at the winter pole. This creates a rising of air over the summer pole and a sinking of air over the winter pole. The rising air expands and cools adiabatically and the sinking air compresses and warms adiabatically. This creates the observed cooler temperatures than expected in the summer mesopause region and the warmer than expected temperatures in the winter mesopause region. This circulation is known as the Dobson-Brewer circulation and is illustrated in Figure 1.11.

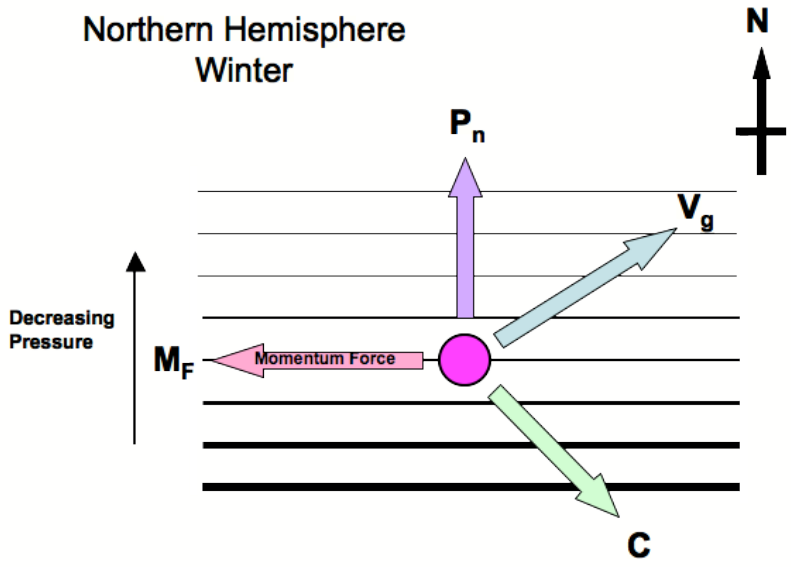

Figure 1.9: A schematic diagram illustrating the the balance of forces on an air parcel in the real atmosphere in the winter northern hemisphere. P_n is the pressure gradient, C is the Coriolis force and V_g is the resultant geostrophic velocity. The parallel horizontal lines represent isobars.

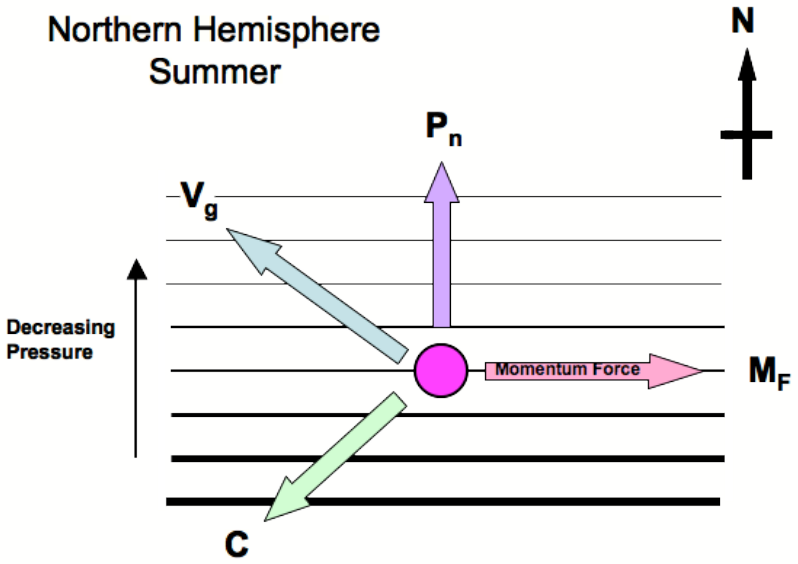

Figure 1.10: A schematic diagram illustrating the the balance of forces on an air parcel in the real atmosphere in the summer northern hemisphere. P_n is the pressure gradient, C is the Coriolis force and V_g is the resultant geostrophic velocity. The parallel horizontal lines represent isobars.

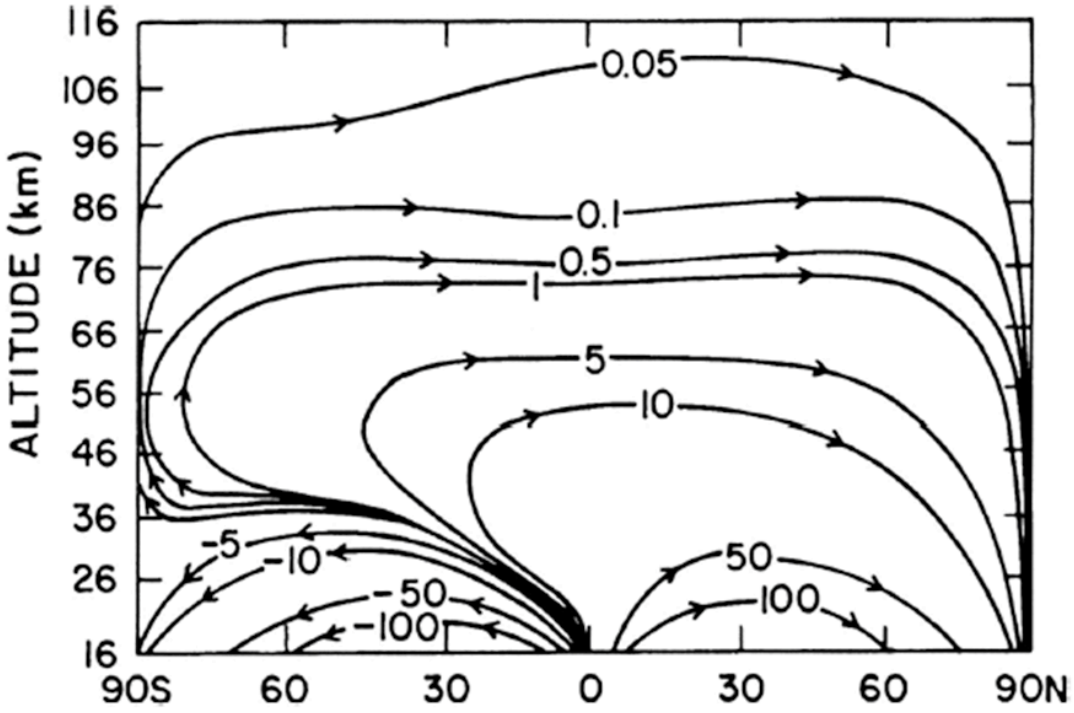

Figure 1.11: Calculated meridional stream function in units $\mathrm{kgm^{-1}s^{-1}}$ during the Northern hemisphere winter solstice. After Garcia and Solomon (1983). This is the Dobson-Brewer circulation.

1.7 Summary

This chapter gave a brief introduction to the general structure of the Earth's atmosphere in particular the mesosphere and lower thermosphere. The temperature structure and general circulation of the atmosphere was introduced and why this is removed from the predicted radiative equilibrium model is discussed. It also introduced the different types of waves that propagate within the atmosphere and the effect they have on the dynamic forcing in the middle atmosphere.

Chapter 2

Planetary Waves

2.1 Introduction

The atmosphere can support many different types of wave motion. They can be classified in various ways according to their physical characteristics. This includes their 'restoring forces', which includes buoyancy for gravity waves, buoyancy and Coriolis effects for inertio-gravity waves and the poleward gradient of planetary vorticity for planetary waves. Another classification can be between forced and free waves. Forced waves are excited by a mechanism of given phase speed and wavenumber (e.g., solar tides or stationary planetary waves) and free waves which are not. Some waves can propagate and some are evanescent and so are incapable of vertical propagation.

Planetary waves are large-scale oscillations in the atmosphere, having wavelengths of the scale of the Earth's radius. The atmosphere behaves rather like a giant wave guide and allows only certain frequencies and wavelengths to propagate. Air parcels moving in response to a planetary wave may be meridionally displaced by up to several thousand kilometres. The wave is coherent around a circle of latitude. Planetary waves can be described by spherical harmonics. Included in the category of free oscillations are the so called 'normal modes', which are natural resonances of the atmosphere. The normal modes have periods which are approximately 2, 5, 10 and 16 days (Salby, 1996). As an example of planetary wave disturbance Figure 2.1 shows a model using the UK Universities Global Atmospheric Modelling Programme (UGAMP) Global Circulation Model (GCM) of a zonal wavenumber wave 4 pattern westward travelling planetary wave with a period of 2 days after (Norton and Thuburn, 1996). The horizontal propagation of a planetary wave can either be stationary or travelling westward or eastward with respect to the background zonal flow, although the majority of waves will propagate westward with respect to the mean flow. The vertical

propagation depends heavily on the zonal flow and is governed largely by wave/mean-flow interaction (see Section 2.3). This means that in summer, waves which are generated in the troposphere are restricted by the westwards stratospheric winds above and so cannot reach the mesosphere and lower thermosphere (MLT) region. However, in winter the westward propagation of planetary waves is not inhibited, because the stratospheric winds are then eastwards, and the planetary wave thus can ascend out of the troposphere and into the stratosphere and mesosphere above.

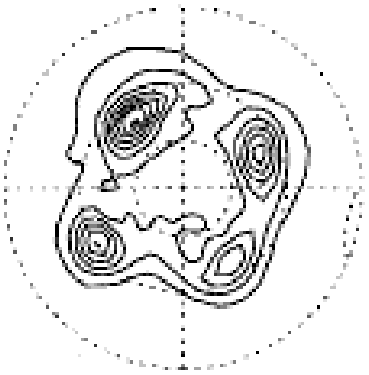

Figure 2.1: Results from the UK Universities Global Atmospheric Modelling Programme (UGAMP) Global Circulation Model (GCM), a 2-day planetary wave of zonal wavenumber 4 is shown in the Northern Hemisphere on contours of Potential Vorticity (PV) on the 300 K isentrope (near 0.1 hPa 65 km) for 7^{th} August. Contours interval 2×10^{-2} m^2 s^{-1} kg^{-1} K after (Norton and Thuburn, 1996). The figure is shown as if looking from above the North Pole down onto the Earth's atmosphere at a height of 65 km.

Planetary waves are an important feature in the atmosphere owing to the large amplitudes they can reach. For example, they are known to drive the poleward meridional flow in the lower stratosphere, in which air moves away from the equatorial region towards high latitudes. Planetary waves play a key role in the break up of the stratospheric winter polar vortex at the end of the winter season. Planetary waves in the Northern Hemisphere, forced by the underlying topography, can reach very large amplitudes. These large waves distort and then ultimately break up the polar vortex. The large amplitude waves involved in this process can result in reversals of the zonal wind as shown in Hoffmann et al. (2002) and can advect air from lower latitudes to polar latitudes, resulting in abrupt temperature changes of as much as 50 K, in the case of Hoffmann et al. (2007) there was a cooling of about 10-20 K in the 90 km region in the Northern Hemisphere following the major stratospheric warming event in January 2006. Planetary wave amplitudes tend to be larger in the Northern Hemisphere than in the Southern Hemisphere because of the different distributions of contents and orography. As a result Southern Hemisphere stratospheric temperatures are cooler and the vortex is stronger. The only major stratospheric warming observed in the Southern Hemisphere was in 2002. In the MLT region planetary waves interact strongly with tides and create a modulation of the tidal amplitudes at planetary wave periods (Pancheva et al., 2000).

2.2 Vorticity and Planetary Waves

The *relative vorticity*, ζ ,is defined as the curl of the velocity vector, i.e,

$$\zeta = \hat{\mathbf{k}} \cdot (\nabla \times \mathbf{u}) \tag{2.1}$$

where $\mathbf{u}$ is the relative vorticity (i.e., that which is seen in our rotating frame of reference and measured with respect to the Earth's surface) and $\hat{\mathbf{k}}$ is the unit vertical vector (Houghton, 1989). Therefore, the relative vorticity is perpendicular to the Earth's surface and is the measure of the local rotation of the atmosphere with respect to the surface.

The *planetary vorticity* is given by 2Ω where Ω is the Earth's rotational angular velocity vector. The vertical component of the planetary vorticity is given by the Coriolis parameter, f, where $f = 2\Omega \sin\phi$ (where ϕ is the latitude). The Coriolis parameter is a measure of the local vertical vorticity due to the the rotation of the Earth.

The absolute vorticity, η, is defined as the sum of the relative vorticity, ζ, and the vertical component of planetary vorticity, f, i.e.,

$$\eta = \zeta + f \tag{2.2}$$

Therefore the absolute vorticity is a combination of the rotation of the fluid itself and the rotation due to the Earth's spin. Planetary waves conserve absolute vorticity, therefore the time derivative of the absolute vorticity, η, must be zero. Hence:

$$\frac{d(\zeta + f)}{dt} = 0 \tag{2.3}$$

This shows that when absolute vorticity is conserved, if f increases, ζ must decrease and *vice versa*. This is the process that gives rise to planetary wave motion and is demonstrated in Figure 2.2. The horizontal line in the figure represents a material line of eastward travelling fluid parcels that are at a constant latitude in the northern hemisphere. Suppose there is some disturbance and the air parcels are displaced to the line marked $\eta(t = 0)$. As the air parcels are displaced their absolute vorticity is conserved. As an air parcel is displaced equatorward the planetary vorticity, $f = 2\Omega \sin\phi$, decreases and so the relative vorticity must increase causing the air parcel to spin anti-clockwise. The spin direction in combination with the eastward flow causes an induced northward motion ahead of the air parcel and it is deflected towards the pole back i.e., towards its original latitude. The air parcel then overshoots its equilibrium position and the reverse occurs, the planetary vorticity increases as the relative vorticity decreases. This causes the air parcel to spin clockwise inducing a

southward motion ahead of it directing it back to its equilibrium position. The air parcel will then continue to cycle back and forth. The phase of the wave itself has propagated *westwards* with respect to the mean flow, this is represented in Figure 2.2 by the dashed line marked $\eta(t > 0)$. For example, southward motion behind the anti-clockwise spinning air parcel, displaces that segment of the material line equatorward, shifting the wave trough westward (Salby, 1996).

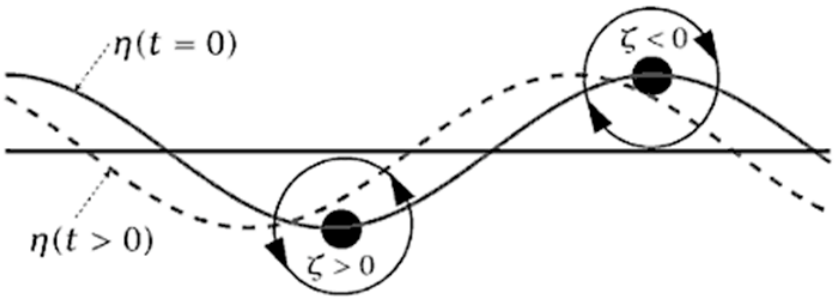

Figure 2.2: A schematic diagram showing the relationship between planetary vorticity, relative vorticity and an air parcel in the mechanism of a 2-dimensional Rossby wave, after Vallis (2010). An initial disturbance displaces the straight horizontal line which is at constant latitude to the solid line marked $\eta(t = 0)$. Conservation of absolute vorticity, leads to the production of relative vorticity and a local spin for the two parcels shown. The spin of the particles along with the eastward flow advects the fluid parcels to the dashed line marked $\eta(t > 0)$. The phase of the wave has propagated westwards.

2.3 Rossby Waves

The simplest form of planetary wave occurs because of the variation of the Coriolis parameter with latitude and are known as *Rossby waves*. Their behaviour can be better understood by deriving their dispersion relation this is shown below following Houghton (1989). The simplest Rossby wave solution is obtained for an atmosphere of constant density with a uniform zonal flow and no vertical motion. The necessary momentum equations and the continuity equation are :

$$\frac{du}{dt} + \frac{1}{\rho}\frac{\partial p}{\partial x} - fv = 0 \tag{2.4}$$

$$\frac{dv}{dt} + \frac{1}{\rho}\frac{\partial p}{\partial y} - fu = 0 \tag{2.5}$$

$$\frac{\partial u}{\partial x} + \frac{\partial v}{\partial y} = 0 \tag{2.6}$$

These equations may be combined by partially differentiating Equation (2.4) with $\frac{\partial}{\partial y}$ and Equation (2.5) with $\frac{\partial}{\partial x}$ and then subtracting to give:

$$\frac{d}{dt}\left(\frac{\partial v}{\partial x} - \frac{\partial u}{\partial y}\right) + f\left(\frac{\partial v}{\partial y} + \frac{\partial u}{\partial x}\right) + v\frac{\partial f}{\partial y} = 0 \tag{2.7}$$

The first term $\left(\frac{\partial v}{\partial x} - \frac{\partial u}{\partial y}\right)$ is known as the *relative vorticity*, ζ, which is a measure of the local 'spin' of the fluid flow. It may be considered as being a vector which is equal to the curl of the relative velocity observed in a co-ordinate system rotating with the Earth. The second term is equal to zero from equation (2.6). Therefore Equation (2.7) may be re-written as:

$$\frac{d(\zeta + f)}{dt} = \frac{d\eta}{dt} = 0 \tag{2.8}$$

where $(\zeta + f) = \eta$ is the *absolute vorticity*. This is the vorticity due to the rotation of the fluid itself with respect to the Earth added to a component arising from the rotation of the Earth itself. Equation (2.8) shows that under conditions of non-divergent, frictionless flow, absolute vorticity is conserved.

To solve Equation (2.8) for wave-like solutions a linear relationship is assumed between f and y, i.e., let $f = f_0 + \beta y$. This is the *beta-plane approximation* i.e, the assumption that the rate of change of the Coriolis force is linear with latitude and varies at a rate β. If we assume a uniform zonal flow $\bar{u}$ plus a perturbation flow, u', then $u = \bar{u} + u'$. The meridional velocity will consist of a perturbation flow only, expressed as $v = v'$ since we have already assumed no meridional flow, then substituting into (2.8) and linearising the equation becomes:

$$\left(\frac{\partial}{\partial t} + \bar{u}\frac{\partial}{\partial x}\right)\left(\frac{\partial v'}{\partial x} - \frac{\partial u'}{\partial y}\right) + \beta v' = 0 \tag{2.9}$$

Because the horizontal flow is non-divergent i.e., $\left(\frac{\partial u}{\partial x} + \frac{\partial v}{\partial y}\right) = 0$, the flow field can be represented completely by a stream function to automatically satisfy the continuity equation (2.6). A stream function is

$$u' = -\frac{\partial \psi}{\partial y}, \quad v' = \frac{\partial \psi}{\partial x} \tag{2.10}$$

substituting this into Equation (2.9) gives:

$$\left(\frac{\partial}{\partial t} + \bar{u}\frac{\partial}{\partial x}\right)\nabla^2\psi + \beta\frac{\partial \psi}{\partial x} = 0 \tag{2.11}$$

For wave solutions to be possible i.e., $\psi = Re\{\psi_0 exp(\omega t + kx + ly)\}$, the dispersion relation

$$c = -\frac{\omega}{k} = \bar{u} - \frac{\beta}{k^2 + l^2} \tag{2.12}$$

must be satisfied, (where ω is the wave frequency, t is time and k, l are the wavenumbers in the x and y directions respectively and c is the zonal phase speed of the wave). The velocity relative to the zonal flow is $c - \bar{u}$ where c is the phase speed in the x direction. This phase

speed must be negative since the term $\frac{\beta}{k^2+l^2}$ can only be positive. Rossby waves therefore drift to the west relative to the mean flow at typical speeds of a few meters per second. Note that the phase speed c, of the wave increases with wavelength. Therefore, Rossby waves with shorter wavelengths propagate more slowly westwards with respect to the mean flow. However, note that a complete three-dimensional treatment, such as that given in depth by Salby (1996), demonstrates that waves of short zonal wavelength will actually propagate eastward. Such short horizontal wavelengths have been observed for, e.g., wavenumber two waves at polar latitudes, which do indeed propagate eastwards (e.g., Nozawa et al., 2003b; Sandford et al., 2008).

The above derivation of the dispersion relation is a two-dimensional treatment. To extend this dispersion relation to include the *vertical* propagation of planetary waves, a three-dimensional description is needed. To simplify the physics an atmosphere with constant density is assumed by employing the *Boussinesq approximation* where changes in density are neglected except where they are coupled with gravity to produce buoyancy forces. This yields the dispersion relation for three-dimensional Rossby waves

$$c = -\frac{\omega}{k} = \bar{u} - \frac{\beta}{\left(k^2 + l^2 + \frac{m^2 f_0^2}{g\omega_{\mathbf{b}}}\right)} \tag{2.13}$$

where m is the vertical wavenumber and $\omega_{\mathbf{b}}$ is the Brunt-Väisälä frequency. This dispersion relation reveals that the vertical propagation of planetary waves is very sensitive to the state of the mean flow. Vertical wavelengths are in the order of 1% of the horizontal wavelengths. These large-scale waves may be forced by large land masses at the Earth's surface. This creates waves that are stationary with respect to the Earth's surface. These planetary waves are known as *stationary planetary waves* and their phase speeds, c, are thus zero. For c to be zero from Equation (2.13) it must be that

$$m^2 = \frac{g\omega_{\mathbf{b}}}{f_0^2}\left\{\frac{\beta}{\bar{u}} - (k^2 - l^2)\right\} \tag{2.14}$$

For vertical propagation to occur m^2 must be positive, which sets the condition

$$0 < \bar{u} < \frac{\beta}{k^2 + l^2} \tag{2.15}$$

if we let

$$U_c = \frac{\beta}{k^2 + l^2} \tag{2.16}$$

then

$$0 < \bar{u} < U_c \tag{2.17}$$

where U_c is the *Rossby critical velocity* which is the largest zonal wind speed in which vertical propagation is possible. However, this is for the specific case of stationary planetary waves. In the case of travelling planetary waves we must allow for the non-zero phase speed of the wave with respect to the Earth's surface. This gives

$$0 < \bar{u} - c < U_c \tag{2.18}$$

which is known as the Charney-Drazin criterion which describes the conditions under which vertical propagation is possible. Therefore, under conditions of westward flow ($\bar{u} < 0$) or strong eastward flow ($\bar{u} \gg 0$), no vertical propagation will occur. Waves with high zonal wavenumbers and low zonal phase speeds are thus effectively prevented from propagating into the mesosphere by the background winds of the stratosphere (Charney and Drazin, 1961).

Therefore, the escape of large amounts of planetary-wave energy from the troposphere into the upper atmosphere is prevented in summer by the easterly strong zonal winds of the stratosphere. Propagation does take place in winter but even then there is enough trapping to prevent a large energy flux into the upper atmosphere. It is interesting to note that if this wave energy were actually able to reach the upper atmosphere, it's dissipation would heat the atmosphere to temperatures similar to those of the solar corona (Salby, 1996).

This process explains the lack of stationary planetary-wave activity in the summer stratosphere and mesosphere and the presence of only the lowest wavenumber (gravest-scales) in the winter stratosphere and mesosphere. This means that the circulation in the upper stratosphere and mesosphere is, to a certain extent, mechanically independent of the motion in the lower atmosphere. Therefore, most waves observed in the summertime MLT region must have been generated either *in situ* or been ducted across the equator from the winter hemisphere since they cannot have propagated to the MLT from below.

2.4 Classification of Wave Modes

Tides and planetary waves in the atmosphere can be described by Laplace's tidal equations. These equations describe waves that are bound at the poles and may produce either eastwards or westwards propagating disturbances. Laplace's tidal equation may be expressed in terms of eigenfunction/eigenvalue pairs, each of which consists of a particular wave mode. The eigenfunctions Θ_n are known as *Hough functions*, after the scientist who pioneered their numerical computation (Hough, 1897, 1898). Either the ϵ_n or the h_n (where $\epsilon_n = 4\Omega^2 a^2/(gh_n) \approx 88km/h_n$) are the eigenvalues of the system, where Ω is the angular

velocity of the Earth, a is the radius of the Earth and g is the acceleration due to gravity. The eigenvalue h_n is known as the *equivalent depth*.

Each eigenfunction/eigenvalue pair constitutes a 'mode'. A common nomenclature in defining modes is to express the zonal wavenumber,s, and the meridional index, n, which provide information on the number of latitudinal nodes and the symmetry of Θ_n. Therefore, it is common to refer to a particular mode as the Θ_n^s mode or just the (s, n) mode and then to add some information on the wave period. For example, at the free mode value of $\epsilon_n = 8.4(h_n = 10.5km)$ for a 256 K isothermal atmosphere the (1,-2) mode would represent the '5-day wave'. However, it is more common to refer to planetary-wave modes in the form $(s, |n| - s)$, used by (Salby, 1981a,b, 1984) and Longuet-Higgins (1968) etc. Therefore the 5-day wave is more commonly referred to a (1,1) mode.

In the nomenclature of a (s, n) mode, a mode is symmetric about the equator if $(n+s)$ is odd and antisymmetric if $(n + s)$ is even for Rossby waves. This is the same for mixed Rossby-gravity modes. For symmetric modes, the variables vertical velocity and zonal velocity are mirror images about the equator, whereas the meridional velocity is antisymmetric. For antisymmetric modes, the meridional velocity is symmetric and the other variables change sign at the equatorial node. Table 2.1 lists the global-scale structure parameters for the most commonly observed travelling planetary wave periods of 2, 4, 5, 10 and 16 days.

Planetary Wave	(s, n)	$(s, \|n\|\text{-}s)$	h_n (km)	Additional Descriptors
5-day wave	(1,-2)	(1,1)	10.5	Rotational; Rossby; first symmetric
10-day wave	(1,-3)	(1,2)	10.5	Rotational; Rossby; first asymmetric
16-day wave	(1,-4)	(1,3)	10.5	Rotational; Rossby; second symmetric
4-day wave	(2,-3)	(2,1)	10.5	Rotational; Rossby; first symmetric
2-day wave	(3,-3)	(3,0)	10.5	Mixed Rossby-Gravity; asymmetric

Table 2.1: Nomenclatures and other data for the most important travelling Rossby-normal modes in the middle and upper atmosphere. Also provided are the equivalent depth for each mode h_n after Forbes, J. M. (1995).

The table shows that the various planetary wave modes will have particular zonal wavenumbers. So, the 5-, 10- and 16-day waves will have zonal wavenumber 1, whereas the 4- and 2-day waves will have zonal wavenumbers of 2 and 3 respectively. Further, note that other modes are possible such as the 2-day wave (4, 0) mixed Rossby-gravity mode that will be investigated in Chapter 6. Finally, note that some of these modes also include an element of buoyancy in the 'restoring force', these are the mixed Rossby-gravity modes.

2.5 The Two-Day Wave

The 2-day planetary wave is one of the most important features in the dynamics of the summertime middle atmosphere. At its maximum it is the largest amplitude planetary wave observed anywhere in the mesosphere, with amplitudes as large as 11 K in the Southern Hemisphere (e.g., Limpasuvan and Wu, 2003). The wave is usually observed for about one to two months after the summer solstice when it is present from the upper stratosphere to the lower thermosphere. Wave temperature amplitudes maximise at mid-latitudes and at heights near the mesopause, and the wave is present from equatorial to polar latitudes. Wave amplitudes are known to be larger in the Southern Hemisphere than in the Northern Hemisphere and the wave is primarily a westward-propagating feature of zonal wavenumber 3, although other wavenumbers have been observed (see later).

The 2-day wave is important in the dynamics of the middle atmosphere because it is known to strongly interact with atmospheric tides and to modulate their amplitude (e.g., Teitelbaum and Vial, 1991; Mitchell et al., 1996; Palo et al., 1999; Pancheva et al., 2004; Wu et al., 2008). Further, there is evidence that the 2-day wave can become phase locked to the migrating semidiurnal and diurnal tides (i.e., the 2-day wave would have a period of exactly 48 hours). Interaction with the tides can generate a diurnal zonal wavenumber 6 feature and lead to rapid amplification of the 2-day wave amplitude (e.g., Walterscheid and Vincent, 1996; Hecht et al., 2010; McCormack et al., 2010).

Interactions with tides can also act to constrain 2-day wave amplitudes and result in a cascade of variance to smaller scales within the atmosphere (e.g., Salby and Callaghan, 2008). Non-linear coupling between the 2-day wave and the migrating diurnal tide has been proposed as a mechanism capable of exciting other planetary-wave modes (e.g., an eastward propagating zonal wavenumber 2, Palo et al. (2007b)).

The temperature perturbations associated with the wave have been shown to control the variability of polar mesospheric clouds (e.g., Merkel et al., 2009). Evidence that the 2-day wave at low latitudes influences polar summer time mesopause-region temperatures decreasing them by up to as much as 9 K has been provided by Morris et al. (2009) based on the occurrence frequency of polar mesosphere summer echoes. The 2-day wave influences the photochemistry and transport of minor species in the mesosphere (e.g., Kulikov, 2007). The 2-day wave is also known to produce a strong modulation of the ionosphere through mechanisms which remain poorly understood (e.g., Forbes et al., 1997; Forbes and Zhang, 1997), these in turn produce a 2-day modulation of the geomagnetic field (Yamada, 2009). There are also suggestions that the equatorial quasi-biennial-oscillation (QBO) influences the amplitude of the 2-day wave (Li et al., 2008).

The two-day wave was first detected in meteor-radar observations of mesospheric winds

by Muller (1972). The wave has since been extensively studied by ground-based radar and satellites. Meteor and MF radars were first used to investigate the structure and climatology of the wave in wind perturbations. The majority of ground-based studies have been made at middle and low latitudes (e.g., Salby and Roper, 1980; Craig et al., 1983; Plumb et al., 1987; Tsuda et al., 1988; Harris and Vincent, 1993; Palo and Avery, 1996; Jacobi et al., 1997; Thayaparan et al., 1997; Jacobi et al., 1998; Gurubaran et al., 2001; Manson et al., 2004a; Pancheva et al., 2004; Riggin et al., 2004; Meek and Manson, 2009). However, there have been comparatively few ground-based studies of the wave at polar latitudes in the MLT, although 2-day waves have been reported in the winter polar stratosphere region (e.g., Prata, 1984; Coy et al., 2003; Lait and Stanford, 1988).

Recent studies made using ground-based radars have investigated the summertime mesospheric polar 2-day wave and have also revealed the existence of strong 2-day wave activity around the winter solstice at high latitudes (Nozawa et al., 2003a,b; Manson et al., 2004b; Merzlyakov et al., 2004; Riggin et al., 2004; Nozawa et al., 2005; Palo et al., 2007b; Baumgaertner et al., 2008; Sandford et al., 2008; Tunbridge and Mitchell, 2009). Nozawa et al. (2003a) presented a climatology of the 2-day wave in the Arctic based on three years of observations at heights of 70 - 91 km made by an MF radar at Tromsø (69.6°N, 19.2°E). They observed 2-day wave activity in both summer and winter. Manson et al. (2004b) presented observations of the 2-day wave for one year using MF radars at Tromsø (69.6°N, 19.2°E) and Andenes MF radar (69°N, 16°E), and meteor radar at Esrange (68°N, 21°E). Again, significant wave activity was observed in winter as well as in summer. This strong winter activity is not observed at low or middle latitudes. Nozawa et al. (2003b) further investigated the characteristics of the 2-day wave at Tromsø (69.6°N, 19.2°E) and Poker Flat (65.2°N, 147.6°W). They suggested that zonal wavenumbers 2 and 4 occur more frequently than zonal wavenumber 3 and that the wintertime 2-day wave might actually be an E2 oscillation. This suggestion was confirmed in the satellite study of Sandford et al. (2008).

There have been very few studies of the 2-day wave at Antarctic latitudes. Phillips (1989) observed the 2-day wave over Mawson, Antarctica (67°S, 63°E) and Adelaide, Australia (35°S, 138°E). Baumgaertner et al. (2008) reported 2-day waves in the Antarctic at heights up to 95 km measured by MF radars at Scott Base (78°S, 167°E), Davis (69°S, 78°E), and Rothera (68°S, 68°W). Again, wave activity was evident in summer and winter.

However, ground-based radar measurements are limited to a particular latitude and longitude, making it not possible for a single instrument to determine the zonal structure of the wave, i.e., to determine the zonal wavenumber. To overcome this limitation, some studies have been conducted using longitudinally-spaced networks of two or more ground-based radars (e.g., Glass et al., 1975; Muller and Nelson, 1978; Clark et al., 1994; Pancheva et al., 2004). However, while offering excellent height and time resolution these multi-instruments are limited by instrument biases and spatial ambiguities due to sparse sampling which is not

necessarily present in satellite observations. These ground-based radar observations have led to a reasonable general understanding of the characteristics of the 2-day wave, including its vertical structure, period, amplitudes and seasonal variability.

Satellite observations of the 2-day wave have been made using various instruments that measure atmospheric temperature including the Nimbus 5 SCR and Nimbus 6 PMR (e.g., Rodgers and Prata, 1981), MLS on UARS (e.g., Limpasuvan and Wu, 2003; Riggin et al., 2004) SABER on TIMED, (e.g., Garcia et al., 2005; Palo et al., 2007b) and EOS MLS on Aura (e.g., Limpasuvan et al., 2005; Sandford et al., 2008; Meek and Manson, 2009). Satellite instruments have also been used to measure atmospheric winds associated with the 2-day wave, for example HRDI on UARS (e.g., Wu et al., 1993; Riggin et al., 2004), WINDII on UARS, (e.g., Ward et al., 1996) and more recently the Line of Sight (LOS) winds from the EOS MLS on Aura (e.g., Limpasuvan et al., 2005; Wu et al., 2008; Limpasuvan and Wu, 2009)

These studies have complemented ground-based observations of the seasonal behaviour and latitude and height structure of the wave. They have also revealed that the zonal wavenumber structure of the 2-day wave is, in fact, a complex of several different wavenumbers. The largest amplitude wavenumbers are the westward propagating zonal wavenumbers 2, 3 and 4 (hereafter W2, W3 and W4 respectively). The W3 reaches larger amplitudes in the Southern Hemisphere than in the Northern Hemisphere. In contrast, the W4 component reaches larger amplitudes in the Northern Hemisphere (e.g., Limpasuvan et al., 2000; Riggin et al., 2004; Garcia et al., 2005).

The wave period also varies between the two hemispheres. In the southern hemisphere at low to middle latitudes the wave period is often observed to be very close to 2 days (e.g., Craig et al., 1980; Wu et al., 1996). However, at high southern latitudes the period has been observed to be slightly longer, e.g., in the range 50 - 53 hours (e.g., Baumgaertner et al., 2008). In the northern hemisphere the wave period is observed to range between about 1.8 and 2.2 days. In both hemispheres the vertical wavelength is usually observed to be very large (larger than $\sim$ 70 km).

Further, note that a study by Palo et al. (2007a) suggested that non-linear interaction between the summertime 2-day wave and the migrating diurnal tide might generate a wavenumber 2 eastward propagating 2-day wave (hereafter E2) which would occur simultaneously with the westward propagating modes.

These observations and others have revealed a general structure for the 2-day wave in temperature and wind amplitudes. The meridional wind amplitudes are found to dominate over the zonal wind amplitudes, particularly towards the equator. At mid-latitudes meridional and zonal amplitudes are more similar and in general, the Southern Hemisphere wind-amplitudes are double that of the Northern Hemisphere wind amplitudes in summertime.

Temperature and geopotential-height amplitudes were also found to maximise at middle latitudes in summertime. Sandford et al. (2008) used geopotential height data from the Aura satellite to investigate the zonal structure of the wintertime 2-day wave and confirmed that it is an E2 oscillation, probably originating on the poleward flank of the stratospheric polar vortex and propagating up into the MLT.

A number of different mechanisms have been proposed for the excitation for the summertime 2-day wave. Salby and Roper (1980) proposed it to be the manifestation of the gravest zonal wavenumber 3 Rossby-gravity (3, 0) normal mode. Alternatively, Plumb (1983) and Pfister (1985) proposed that the wave is generated by a baroclinic instability of the summertime middle atmosphere westward zonal jet. Later work has suggested that both mechanisms may play a part in particular Salby and Callaghan (2001) suggested the wave exhibits characteristics of both the normal and unstable modes and suggested that the global Rossby-gravity wave mode could grow by drawing energy from the zonal winds. In this explanation, wave energy is transferred from the mean flow to the wave in a relatively restricted region near the wave's critical line, and then disperses globally into the planetary-scale structure of the 2-day wave.

In the case of the W4, Plumb (1983) and Pfister (1985) suggested that the W4 is solely due to an instability mode. Rojas and Norton (2007) investigated how a global Rossby-gravity normal mode might amplify from a local instability. They examined the growth rates of the wave in both linear and non-linear models and proposed that the summertime amplification of the 2-day wave results from the interaction of the global-scale Rossby-gravity mode and a local mode excited by instabilities associated with the reversed potential vorticity gradients caused by the summer westward zonal jet. Note that the experimental study of Offermann et al. (2011) suggested that the wave amplitude is related to the meridional gradient of quasi-geostrophic potential vorticity and baroclinic instabilities.

2.6 Summary

This chapter provided an introduction to planetary scale waves in the atmosphere and in particular to the 2-day planetary wave. The chapter started with an introduction to the nature of planetary waves and the different types of planetary waves that are present in the atmosphere. The 'restoring forces' in terms of vorticity was discussed and the dispersion relation of the simplest form of a planetary wave, a 2-dimensional Rossby wave, was described. The limitations to the vertical propagation of a travelling planetary wave was introduced which, explains why the observations of planetary waves in the mesosphere reveal a strong seasonal variability.

Chapter 3

VHF Meteor Radar

3.1 Introduction

Remote sensing of the Earth's atmosphere has played an important role in studying many aspects of the dynamics of the atmosphere. This is particularly so for the case of the mesosphere and lower thermosphere (MLT) region, where it is notoriously difficult to investigate experimentally *in situ* due to it being too high for most instruments apart from those carried by rockets. Rocket-borne measurements can be very accurate but are impractical for continuos long-term study and do not have global coverage.

The principle ground-based methods for sensing the middle atmosphere are active radio sensing (radars), active optical sensing (lidars) and passive optical sensing (airglow spectrometers and imagers). Ground-based atmospheric radars are used to typically produce wind measurements with resolutions in the order of a few seconds to a few hours. They can measure the 3-dimensional wind field and are therefore good instruments to observe atmospheric dynamics. The main types of radar used to study the dynamics of the middle atmosphere are mesosphere-stratosphere-troposphere (MST) radars , medium frequency (MF) radars, incoherent scatter (ISR) radars and meteor radars.

Meteor radars measure radio waves reflected from the ionised trails of meteors. These trails drift with the neutral winds where they are formed at heights between $\sim$ 75 - 110 km. Therefore they can be used as tracers of the motion of the atmosphere. A practical meteor radar might detect a few thousand individual meteors per day. These meteor count rates make the technique particularly suitable for studies of mean winds, tides and planetary waves that dominate the flow in this region. Meteor radars are well suited for collecting extended data sets since they can operate continuously and automatically with little maintenance for

periods of many years (e.g., the meteor radar at Esrange has been in operation for 11 years). They are also free from the constraints of optical methods and so are unaffected by weather conditions and are not restricted to hours of darkness, as are some optical techniques.

3.2 Meteors: an atmospheric phenomenon

When a particle of interplanetary material, a meteoroid, collides with the Earth's atmosphere it can become a luminous phenomenon known as a meteor or a 'shooting star'. Only particles with certain mass and velocity will produce enough energy to emit light. The smallest particles able to produce meteors are $\sim$ 0.01 mm and there is no upper limit. The largest meteoroids recorded by instruments are about 10 m in size. However, typical meteoroids are between 0.05 mm and 20 cm (Ceplecha et al., 1998).

Figure 3.1: A 19th-Century engraving of the Perseid meteor shower.

When a meteoroid starts to enter the atmosphere at heights of 100 - 300 km they are heated up very quickly by frictional heating with gases in the Earth's atmosphere. The surface temperature of the meteoroid rises very rapidly. Thus, for bodies larger than $\sim$ 0.5 mm there is no time for them to be heated throughout and the surface layer ablates. At heights of 80 - 90 km the surface temperature of the meteoroid reaches $\sim$ 2200 K. At this point the meteoroid material starts to ablate and sublimate producing a trail of hot vapours. Inellastic collisions of the atoms and molecules in these vapours with the surrounding air molecules produce a cylindrical trail of ionised material and free electrons in the wake of the meteoroid. The visible streak of light emitted from the meteor, seen as a 'shooting-star', is due to the de-excitation of the incandescent material. The free electrons in the trail are the scatterers of the radio waves from the meteor radar.

The entry speeds of meteoroids as they enter the Earth's atmosphere are between 11.2 and 72.8 kms^{-1} it is the kinetic energy at this speed that provides the energy that produces the incandescent gas and ionisation of the meteor trail. The lower limit of 11.2 kms^{-1} is due solely to the Earth's gravitational pull on a meteoroid that would have been initially at rest. The upper limit of 72.8 kms^{-1} results from a head-on collision between the Earth and a meteoroid orbiting the Sun at a distance of the Earth (1 AU). At this distance the escape velocity from the Sun is 42.5 kms^{-1} , which is the maximum speed a meteoroid could travel if it were orbiting the Sun at 1 AU. The Earth orbits the Sun at a speed of 30.3 kms^{-1} at perihelion. The summation of these two speeds yields the theoretical maximum of 72.8 kms^{-1} . If the meteoroid is less than several hundredths of a millimeter in diameter it is slowed down enough to not allow its surface temperature to reach evaporation point and so no hot vapours occur instead it sediments slowly through the atmosphere. This is a meteoroid dust particle.

3.2.1 Meteor Trails

Meteoroids of size smaller than a radius of ~ 0.1 cm make up the majority of those detected by meteor radar. The structure of the ionised trail typically has the shape of an elongated cone a few tens of kilometers long and will extend over a height range of 10 - 15 km. The exact geometry will vary for each individual meteor since it depends on the entry speed, entry angle and initial mass of the meteoroid. The trail consists of a core of high ionisation density surrounded by a region of less dense ionisation. The initial radius of the trail is defined by the root mean square value of the radial position of the ions once thermal equilibrium has been reached (this takes 10 or so collisions). This initial trail radius is determined by the entry speed of the meteor and the height of the formative trail. This is because atmospheric mean free path increases with height and so the trail radius will be greater at greater heights. For example, for a typical 40 kms^{-1} meteoroid, the initial radius of the trail will be ~ 0.3, 0.6 and 1.2m at heights of 75, 90 and 105 km respectively.

The meteor trail has a short lifetime of a few seconds to a few minutes (although some trails can last for many minutes (Close et al., 2000)). Immediately after the trail is formed, it starts to diffuse outwards and it's electron number density decreases although the electron line density remains the same. This is due to ambipolar diffusion, atmospheric turbulence and recombination. Radio studies of meteors have shown that the most important processes is ambipolar diffusion which affects the volume density but not the line density (Ceplecha et al., 1998).

3.2.2 Radio Reflection from Meteor Trails

Meteor radars use meteor trails to determine-middle atmosphere winds. Meteor radars are designed to detect radio scatter from the free electrons in the ionised meteor trail. The reflection of radio waves off meteor trails is *specular reflection* (like the reflection from a mirror). Therefore, for a backscatter system where the transmitter (Tx) and receiver antenna (Rx) are in the same place, the reflection of the transmitted signal will only be returned if the radio wave is orthogonal to the ionised trail. This is shown in figure 3.2.

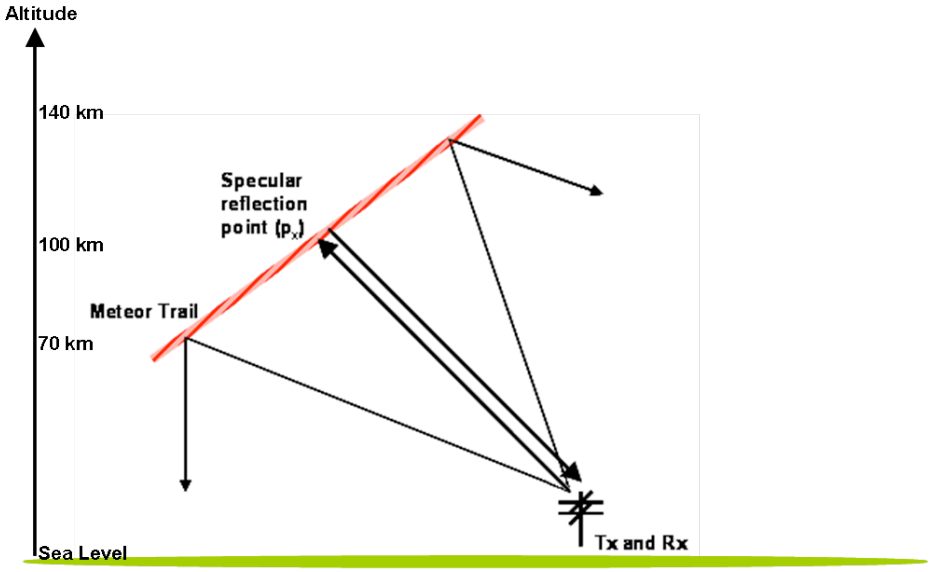

Figure 3.2: Geometry of the meteor radar backscatter showing specular reflection

Thus, in order to be detected, some part of the meteor trail must be perpendicular to the line-of-sight to the radar. If this is not the case then the meteor will not be detected, regardless of the radar power, distance to the meteor or the ionisation energy. Hence, the majority of meteors falling into the radar's 'collecting volume' will not be detected even for so called 'all-sky' systems that use low-gain antennas to illuminate a large volume of the meteor region.

3.2.3 Meteor-Echo Signals

The amplitude of a radio echo received from a meteor trail will rise rapidly to a maximum value as a meteor moves past the specular reflection point. Most of the returned signal here is from the first Fresnel zone. The echo behaviour after this maximum depends strongly on the density of free electrons in the meteor trail. If the electron line density is less than $\sim 10^{14}$ m^{-1} the echo that is returned from the trail is termed an *underdense* echo. The majority of meteor echoes are of this type. In an underdense echo the radio wave can penetrate into the trail and the echo power received is a sum of all the individual contributions of the

scattering from the electrons in the trail. Underdense meteor echoes come from meteoroids that are typically smaller than 10^{-5} kg (a radius of ~ 0.1 cm).

The amplitude-time profile of a typical underdense echo is shown in Figure 3.3. There is a sharp increase in the amplitude of the returned signal that lasts no more than a few tenths of a second, followed by exponential decay which takes about half a second to return to the noise level. The rapid decay is due to ambipolar diffusion which increases the trail radius with time until it becomes large enough for destructive interference of radio signals to occur between the signal scattered from electrons at different depths in the trail. This characteristic shape of an underdense meteor echo is very useful for distinguishing between a meteor echo and a spurious signal.

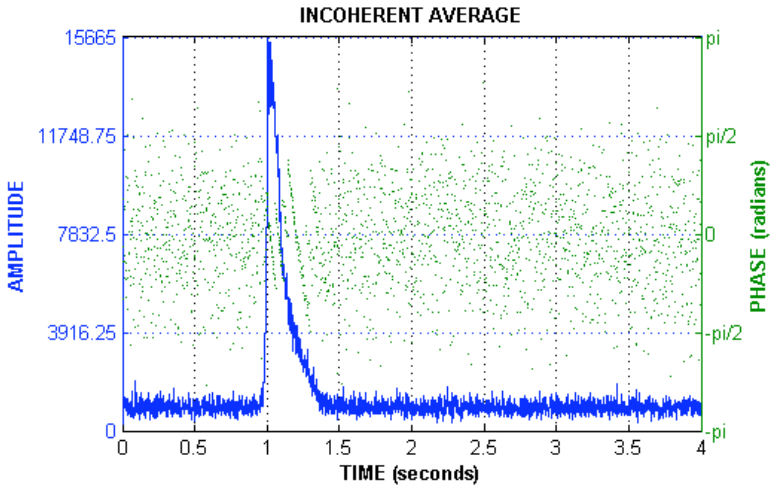

Figure 3.3: The amplitude in arbitrary units of a typical underdense meteor echo as a function of time. This echo was observed by the Esrange meteor radar.

The maximum height at which an underdense echo can be detected is termed the *underdense echo ceiling*. This is the height at which destructive interference is caused immediately after in the initial trail radius is formed (recall that the initial trail radius increases with height). This is dependent on the radio wavelength used such that the underdense echo ceiling will be higher for longer radio wavelengths. Meteors that occur above this height are not detected. The lower limit of meter detection is determined by the total destruction, by ablation, of the meteoroid. For a typical meteor this is ~ 75 km in height.

If the electron line density is larger than $\sim 10^{14}$ m^{-1} the echo that is returned from the trail is termed an *overdense* echo. A minority of meteors are overdense. In this case the electron density is sufficient enough to totally reflect the incident wave from the trail surface so that the radio wave cannot penetrate into the ionised trail. The reflection of the radio wave is as if the trail were a metal cylinder. The reflected signals may last for many seconds and can therefore be subject to severe distortions as strong winds distort the meteor trail, possibly leading to multiple refection points.

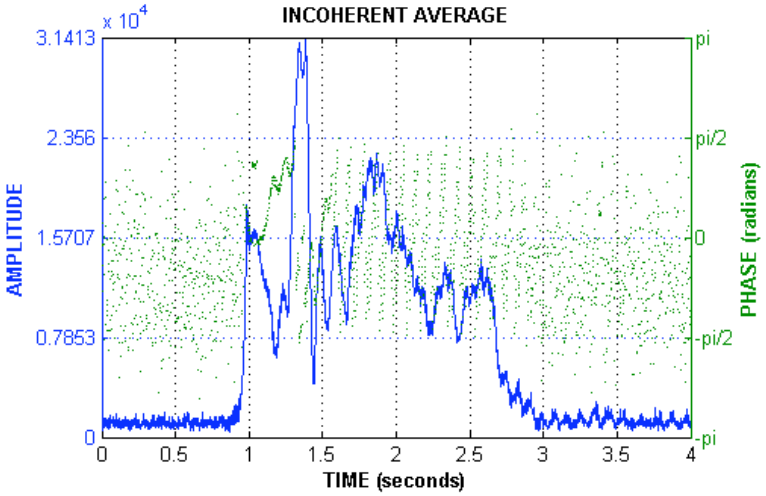

Figure 3.4: The amplitude-time profile of a typical overdense meteor echo observed by the Esrange meteor radar.

Figure 3.4 presents the amplitude-time profile of a typical overdense meteor echo. There is an initial rapid increase in amplitude, as for an underdense echo, but following this there is an irregular pattern in the amplitude and there is no characteristic shape. This is due to the extended lifetime of the trail. The distorted trail can lead to multiple specular reflection points, which can in turn lead to constructive and destructive interference and cause the amplitude of the total received signal to fluctuate. Furthermore, the distortions in the trail may cause the specular reflection point to move along the trail and give spurious drift velocities. Due to this irregular behaviour in the echo power it is difficult to unambiguously discriminate between noise and meteor trail echo. Therefore, the meteor radar used in this study only record data for underdense echoes and any overdense echoes detected are not used.

3.3 The University of Bath Meteor Radars

Data from two polar meteor radars were used in this study. The first is based in the Antarctic at Rothera Point (68°S, 68°W) and was deployed in 2005. The second is based in the Arctic at Esrange (68°N, 21°E) in the Swedish Space Corporation rocket range located near Kiruna, Sweden. Both these radars are commercially produced All-Sky Interferometric Meteor Radar (SKiYMET) systems operating on an all sky configuration. Figure 3.5 show a picture of a typical receiver antennae at Bear Lake in Utah.

The all-sky radar technique has a transmitting antennae with a broad radiation pattern that covers a large expanse of the sky. This is to allow meteors to be detected over the largest volume of atmosphere. This type of system uses interferometric techniques which use phase information from a series of receiver antennas to determine meteor locations.

Figure 3.5: A photograph of one of five receiver antennas at Bear Lake in Utah in February 2007.

The system consists of one transmitter antenna and five receiver antenna in an array which are arranged as an interferometer, see figure 3.6. A single three element Yagi transmitter is used along with five two-element Yagi receivers. The interferometer pattern determines phase differences at the receivers and along with the range information the position of the meteor trail can be accurately located.

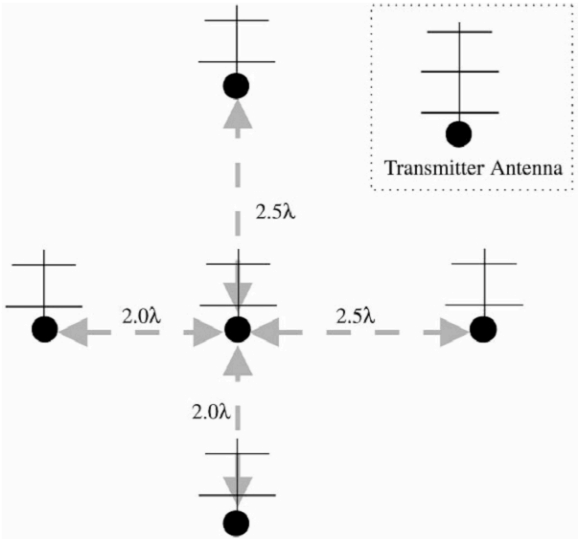

Figure 3.6: Antenna ground plan of a typical SKiYMET radar. Where, λ, is the transmitter wavelength, after Hocking et al. (2001).

The real-time detection, confirmation and analysis of meteor echoes and the determination of meteor parameters is performed in real time by an on-site PC (Hocking et al., 2001). The parameters which describe the meteor and its plasma trail are stored for each meteor detected. These parameters are summarised in Table 3.1. These parameters are then outputted in a mpd file, an example of which is shown in Figure 3.7. A more complete description of the SKiYMET meteor radars is given in Hocking et al. (2001).

The meteor trail formed is essentially frozen into the neutral winds and is then advected. Observations of how many meteor trails drift with time can provide a comprehensive picture of the wind field.

Table 3.1: Parameters stored in a mpd file from the SKiYMET meteor radars.

Parameter	Description
Date	The date of detection relative to Co-ordinated Universal Time (UTC)
Time	The time of detection in UTC (millisecond accuracy)
File	The file name extension used to store the raw data for this detection
Rge	The range of the detection in km (1 decimal place accuracy)
Ht	The height above ground of the detection, a correction is included for the curvature of the Earth.
Vrad	The radial drift velocity of the meteor trail (ms^{-1})
DelVr	The error of the radial velocity measurement obtained from the 5 antennae pairs in the interferometer of receivers. Data with delVr > 5.5 ms^{-1} are rejected.
Theta	The zenith angle of the detection (degrees)
Phi0	The azimuth angle of the detection (degrees) measured from the East
Ambig	Due to ambiguities that arise from the detection system there are several possible locations the detection could have originated from. Ambig records the number of possible locations of the detection.
Delphase	The worst possible phase error between antennas assuming the correctly measured azimuth and zenith (degrees)
ant-pair	The antennae pair that have the worst phase error
IREX	The receive channel used in the analysis for certain single-channel data quality tests. This is "1" during normal operation.
amax	Peak value of amplitude of the meteor echo in digitiser units
Tau	The half-life decay time of the meteor (seconds)
vmet	The entrance speed of the meteor (kms^{-1})
snrdb	The signal to noise ratio of the meteor

```
version 2.2
SITENAME rothera-sk
LOCATION -67.5,-68.0
TIME_ZONE -3.000000
FREQUENCY(MHz)  32.500
LO_FREQUENCY(MHz)  20.700
CHANNELS 10
RESOLUTION(KM)    2.0
GATES  30
START_RGE(KM)    4.0
PRF  2144
ANTENNA_COORDS   18.44  26.00  23.07 206.00  18.44 116.00  23.08 296.00    .00 360.00
PHASE_OFFSETS      .00   -1.20  -98.60  -20.20  -27.40
INTEGRATIONS   4
RECORD_LENGTH  4.00
NSMOOTH  5
MINHT   70
MAXHT  110
RXLIST 1 1 1 1 1
RX_GAIN  115
TIME_ACCURACY HIGH
GPS_STATUS LOCK 67.567627 S 68.119453 W
VEL_ERR_LIM  5.50
SN_ACCEPT_RATIO  1.80
T_DECAY_MAX  2.00
PLANE_NORMAL   5.40 327.40
PULSE_CODE 1
MODE I
```

Date	Time	File	Rge	Ht	Vrad	delVr	Theta	PhiO	Ambig	Delphase	ant pair	IREX	amax	Tau	vmet	snrdb
2005/02/22	0:00:01.608	00000	169.9	91.0	-17.94	4.60	58.3	117.4	1	25.2	13	1	1693.	.103	-9.99	6.5
2005/02/22	0:00:06.069	00001	104.0	96.9	25.90	5.03	21.4	119.1	1	25.2	25	1	3125.	.013	-9.99	10.8
2005/02/22	0:00:14.237	00002	215.9	88.2	-12.96	.22	66.8	49.8	1	5.1	14	1	4292.	.110	-9.99	13.6
2005/02/22	0:00:14.254	00003	217.9	89.1	-11.65	1.72	66.8	49.5	1	15.6	13	1	1584.	.106	-9.99	5.3
2005/02/22	0:00:48.573	00004	153.9	103.4	-20.07	4.71	48.3	341.1	4	38.4	23	1	1989.	.035	-9.99	6.7
2005/02/22	0:00:48.573	00004	223.9	73.3	-20.07	4.71	71.8	120.5	4	37.4	23	1	1989.	.035	-9.99	6.7
2005/02/22	0:00:48.573	00004	293.9	97.6	-20.07	4.71	71.8	120.5	4	37.4	23	1	1989.	.035	-9.99	6.7
2005/02/22	0:00:48.573	00004	223.9	88.0	-20.07	4.71	67.8	8.5	4	29.3	24	1	1989.	.035	-9.99	6.7
2005/02/22	0:01:13.028	00005	173.9	88.8	-24.67	.55	60.0	87.1	1	17.5	35	1	3429.	.101	-9.99	12.2
2005/02/22	0:01:13.062	00006	175.9	89.8	-24.33	1.16	60.0	87.4	1	20.7	45	1	2574.	.098	-9.99	9.1
2005/02/22	0:01:46.256	00008	104.0	97.2	-30.39	.32	20.9	314.9	2	16.3	35	1	2865.	.039	-9.99	10.6
2005/02/22	0:01:46.256	00008	173.9	86.2	-30.39	.32	61.0	354.4	2	24.9	25	1	2865.	.039	-9.99	10.6
2005/02/22	0:01:46.256	00009	104.0	97.2	-30.42	.32	21.0	314.9	2	16.4	35	1	2863.	.039	-9.99	10.6

Figure 3.7: A snapshot of an MPD file from the Rothera radar on the 22nd February 2005.

3.4 The Distribution of Meteor Echoes observed by the SKiYMET Meteor Radars

3.4.1 The Height Distribution

The SKiYMET system detects meteors over a height range of 70 - 110 km with a resolution of $\sim$ 1 km. The height measurements are made using the elevation angle and range measured by the radar for each meteor echo. A correction for the curvature of the Earth is applied. Figure 3.8 shows the height distributions of meteor echoes over Rothera calculated using all meteors detected in January - July 2010.

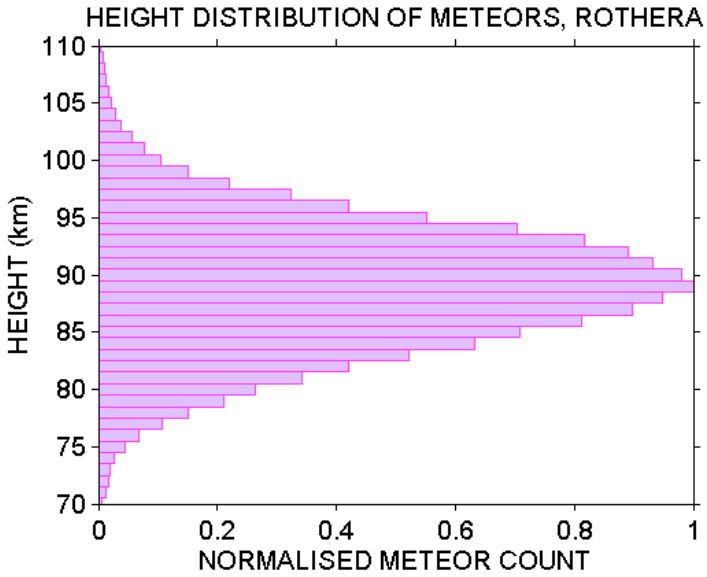

Figure 3.8: The height distribution of meteor echos over Rothera in 2010

The height distribution of meteor echoes approximately follows a Gaussian distribution. Peak values are at $\sim$ 90 km with a standard deviation of $\sim$ 5 km.

3.4.2 The Azimuth Distribution

The radars are 'all-sky' systems so the transmitted power from the transmitting antennae is largely independent of azimuth. This allows the detection of meteors from all azimuth and elevation angles, giving an approximately even azimuthal distribution of meteors detected. This distribution is shown in figures 3.9 and 3.10. The figures show the number of meteors detected in a typical day over Rothera and Esrange. Each individual meteor is represented by a purple dot and the radar is located at the centre.

The observed distribution has some interesting characteristics. The first is that there are

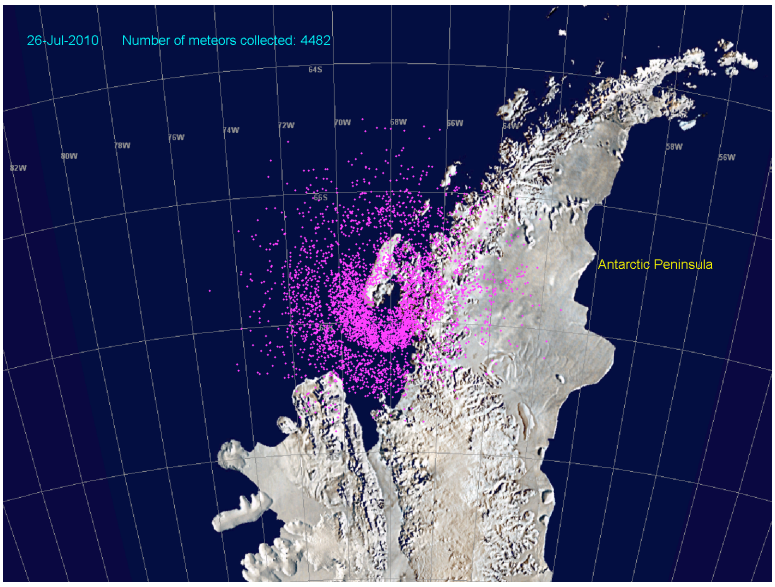

Figure 3.9: The distribution of 4482 individual meteors between a height range of 78 and 110 km for 26^{th} July 2010 detected by the Rothera meteor radar.

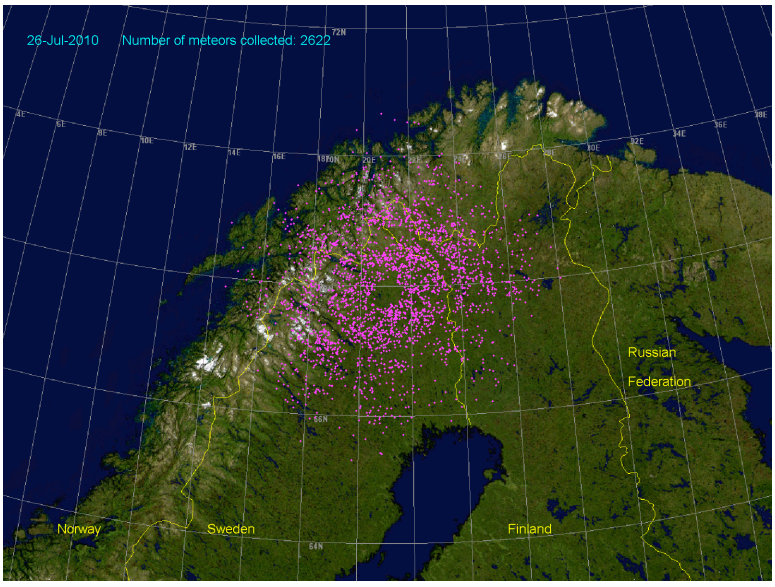

Figure 3.10: The distribution of 2622 individual meteors between a height range of 78 and 110 km for 26^{th} July 2010 detected by the Esrange meteor radar.

rings in which no meteors are detected. This is due to the switching off of the receiver when the pulse is transmitted. This is done because the transmitter and receiver array are in close proximity and so to avoid the receiver being saturated by the direct ground wave the receiver is switched off during pulse transmission. The second is that there are no meteors above the radar. This is due to the specular reflection of radio waves from meteor trails. The angle of detection required near the zenith would mean that the meteor would be travelling nearly horizontally. This would require a long slant path through the atmosphere and even the largest of meteors travelling through the atmosphere would be completely ablated before they reached the zenith.

3.4.3 The Range Distribution

The range distribution of meteor echoes measured by the Rothera system is shown in Figure 3.11. The range distribution for Esrange is nearly identical. The figure highlights the meteor distribution shown in figures 3.9 and 3.10. The gaps in the distribution are noticeable here at ranges of $\sim$ 140, 210 and 280 km. As mentioned previously these mark the times when the receivers were disabled during the transmission of each successive radar pulse. There are very few meteors within a range of 100 km due to the angle of detection requiring a long slant path as discussed above and the meteor count rate decreases with increasing range due to the attenuation of echo power with distance.

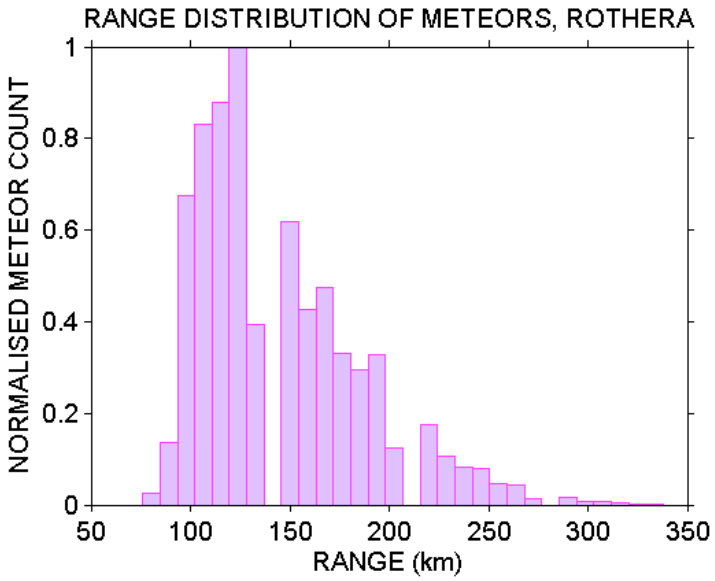

Figure 3.11: Normalised histogram showing the distribution of meteors in range over Rothera in 2010

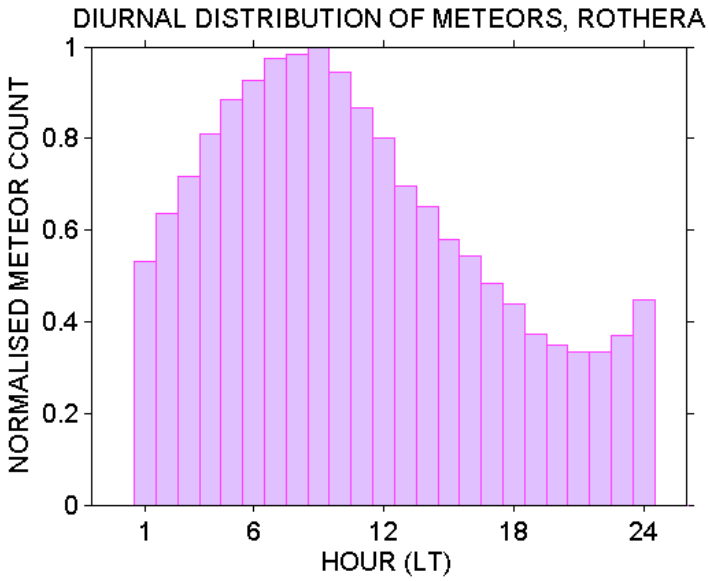

Figure 3.12: Normalised histogram showing the diurnal cycle in meteor count over Rothera for 2010.

3.4.4 The Diurnal Distribution

There is a large variation in the meteor count rate over the course of each day. Figure 3.12 shows a normalised histogram of the count of meteors detected in each hour over the course of a day over Rothera. From the figure it is clear that there is a higher count rates between midnight and midday (00:00 - 12:00 LT). This is due to the rotation of the Earth around the Sun. During the high count rate part of the day the (00:00 - 12:00 LT) the radar site is on the 'leading hemisphere' of the Earth, where sporadic meteors are being 'swept up' by the Earth's atmosphere. As the Earth rotates the radar site moves to 'trailing hemisphere' in the low count rate part of the day (12:00 - 24:00 LT). In this time interval the Earth is effectively blocking the sporadic meteors from the radar sites view and so to fall into the atmosphere meteoroids must 'overtake' the Earth.

The low count rates in the afternoon/evening can lead to gaps in the calculated winds if not enough meteor echoes are detected to allow a reliable value of the wind. Therefore, spectral analysis techniques that do not require evenly-spaced data, for example the Lomb-Scargle Periodogram, must sometimes be used in preference to methods such as Fast Fourier Transforms (FFTs) which require periodically-tabulated data.

3.4.5 The Annual Variability

As well as the diurnal cycle in meteor count rates there is also a seasonal cycle. This is shown in figure 3.13 where daily meteor counts over Esrange for 2007 are plotted. This annual cycle is believed to be astronomical in origin and to result from the distribution of

the sporadic meteor radiants (Hocking et al., 2001; Younger et al., 2009).

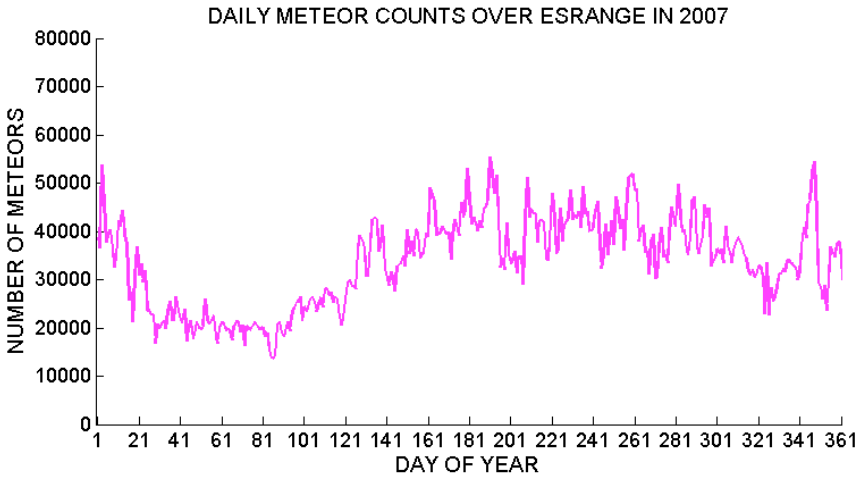

Figure 3.13: Daily meteor counts over Esrange for 2007

3.5 Measurements of middle-atmosphere winds

3.5.1 Determining Atmospheric Winds from a Meteor Radar

The ionised trails detected by meteor radar are 'frozen' into the neutral wind and thus can be used as a tracer for atmospheric motion as they drift with the winds. The drift of the trail along the line of sight of the radar is detected as a phase change in the returned signal. The sign of the phase change depends on whether the meteor is moving away or towards the radar. Therefore a *Doppler shift* method can be used to calculate the radial drift velocity of each meteor trail from which the winds can be deduced.

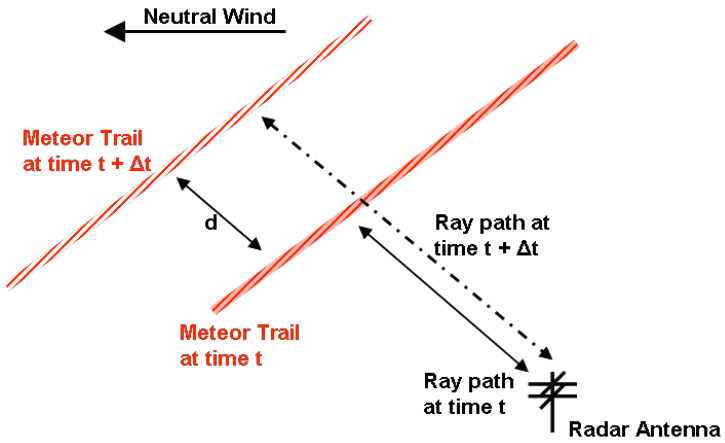

Figure 3.14: Schematic showing the geometry of the phase change method of line-of-sight velocity determination.

Consider the drifting meteor trail presented in Figure 3.14. As the trail drifts it changes its

position from the radar by a distance d. This results in the lengthening of the return path of the signal by a distance $2d$ and therefore will change the phase of the signal. If the trail were to drift a distance that was equivalent to half a wavelength, then the observed phase change would be 2π radians since the total return path to the meteor would have increased by one wavelength. Therefore, when a trail drifts an arbitrary distance, d, and reflects a radio wave of wavelength, λ, a phase change of $4\pi d/\lambda$ will be observed. The magnitude of the line-of-sight drift velocity can then be calculated using equation (3.1).

$$V_{rad} = \frac{d}{\Delta t} = \frac{(\lambda/4\pi)}{(\Delta t/\Delta\phi)} \tag{3.1}$$

where $\Delta\phi/\Delta t$ is the rate of change of the relative phase angle. Assuming that the vertical velocity is negligible the line-of-sight drift velocity can be converted to horizontal velocity.

To determine the atmospheric zonal and meridional winds from a series of meteor drifts two principle assumptions have to be made. These are:

1. The vertical velocities in the MLT are negligible when compared to the horizontal velocities on a time scale of hours. This assumption allows the calculation of horizontal winds from the radial drift velocity. This assumptions is justified since the vertical winds are at least an order of magnitude smaller than the horizontal winds (Mitchell and Howells, 1998).

2. The atmosphere within the meteor collecting volume moves as a uniform slab within a given height range. This assumption is justified for motions that have long horizontal scales that are much larger than the meteor collecting volume, which is a few hundred kilometres in diameter, for example, planetary waves, tides and mean winds.

These two assumptions can then be used to calculate hourly means of the winds provided that measurements from many individual meteor echoes from the collecting volume are combined. Then a reliable wind vector can be calculated.

Only valid echoes are processed for wind analysis. This means that the echoes must meet with the following criteria:

1. There is no ambiguity in the position i.e., only one combination of zenith angle, azimuth angle and range has been calculated for a particular meteor. AMBIG in Table 3.1 and Figure 3.7 must equal 1.

2. The echo decay time (TAU in Table 3.1) is greater than 0.015 s. This is reject any short-lived noise spikes.

Under assumption 1, the *radial velocity* V_{rad} can then be used to calculate the *horizontal velocity*, V_h using equation (3.2). This includes a correction for the curvature of the Earth.

$$V_h = \frac{V_{rad}}{sin(\alpha)} \tag{3.2}$$

Where

$$\alpha = cos^{-1}\left(\frac{(r_E + h)^2 + r^2 - r_E^2}{2r(r_E + h)}\right) \tag{3.3}$$

h is the true height of the meteor, r_E is the radius of the Earth and r is the slant range to the meteor. These equations can be derived from the geometry shown in Figure 3.15.

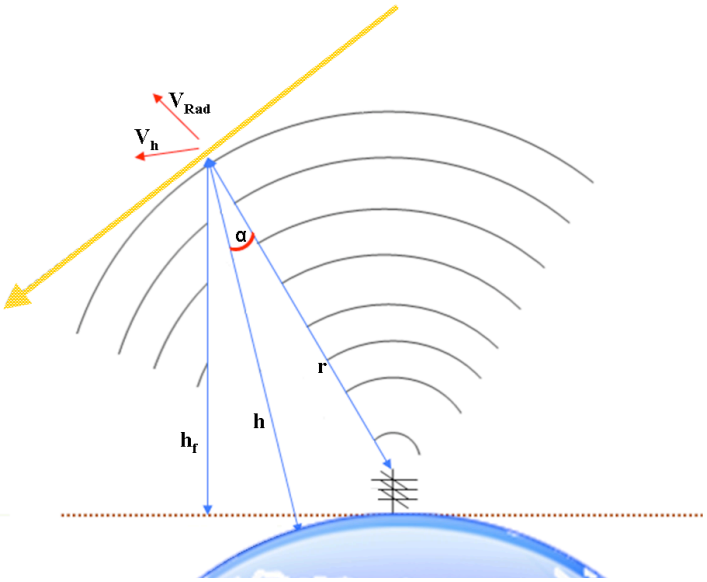

Figure 3.15: Geometry of the curved Earth correction and wind calculation. Where V_{rad} is the radial velocity, V_h is the calculated horizontal velocity, r is the range of the echo, r_E is the radius of the Earth, h is the calculated height and h_f is the false height (no curved Earth correction).

Meteors with zenith angles of less than 15° are discarded because close to the zenith the radial velocities become significantly contaminated by the vertical motions of a few ms^{-1} that are known to exist at these heights (Mitchell and Howells, 1998).

For calculating winds, the meteors are grouped into two-hour intervals and height gates. The SKiYMET radars have height-finding capability which allows the calculation of vertical profiles of the wind. The meteor echoes are binned into six height gates which are analysed separately. The height gates routinely used are (78 - 83), (83 - 86), (86 - 89), (89 - 92), (92 - 95) and (95 - 100) km giving each height gate a depth of 5, 3, 3, 3 and 5 km. The upper and lower gates are deeper to ensure there are enough meteors detected for reliable wind estimates to be made. This is because the meteor count rates are much smaller at the uppermost and lowermost heights - see Figure 3.8. The representative height for each gate is determined by the the mean height of echoes detected in that gate. These representative heights are found to be 80.8, 84.7, 87.5, 90.4, 93.3 and 97.1 km. This differs from the

geometric centre of the height gate since the distribution of detected meteors varies strongly with height. The data are then sorted by moving a two-hour window through the dataset in steps of one hour.

Within each height gate and two-hour interval the meteors are approximately evenly distributed in azimuth around the radar. The horizontal velocities of these meteors will generally follow the bulk flow and so some of the horizontal velocities will be directed toward the radar and some away. Therefore, the horizontal velocities will follow an approximate 'sine wave in azimuth'. Any departures from a sine wave will be due to small-scale motions that are not resolved by the radar. However, these small-scale motions - primarily associated with gravity waves - can be investigated using statistical methods (e.g., Beldon and Mitchell, 2009; Mitchell and Beldon, 2009; Fritts et al., 2010). By fitting a sine wave to the meteor distribution the magnitude and direction of the bulk flow can be calculated. This is shown in Figure 3.16. The amplitude of the sine wave corresponds to the speed of the bulk flow and the phase to the direction of flow. Therefore, the amplitude and phase of the sine wave give the speed and direction of the wind. This can then be resolved into zonal and meridional components.

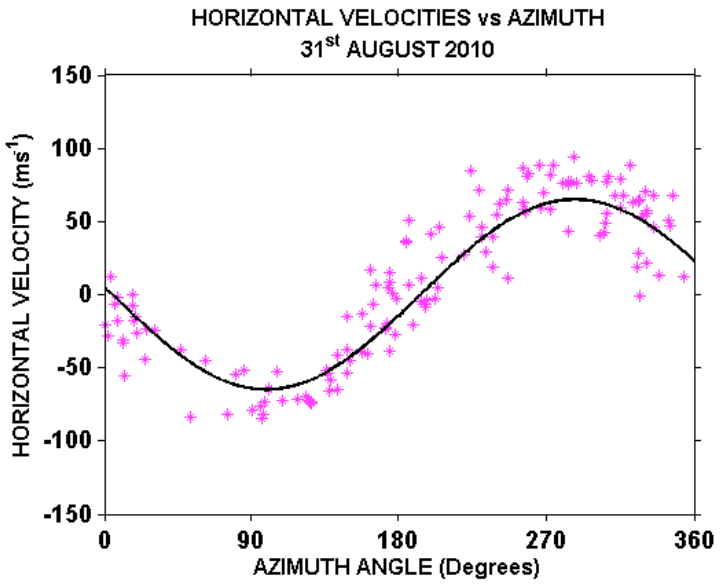

Figure 3.16: A plot of horizontal winds against azimuth for individual meteors recorded between 03.00 and 05:00 UT on 31st August, 2010 over Ascension Island. The data were recorded between a height of 89 to 95 km. The black line indicates the best fit from a least squares fit sine wave to the distribution of horizontal velocities in azimuth. In the case of the data shown, the wind speed (indicated by the amplitude of the fitted sine wave) is approximately 60 ms^{-1} and directed towards an azimuth of 270°.

A student's T-test is then performed on the data to test the 'goodness of fit' between the fitted data and velocity measurements. A bad fit is produced when there are either too few meteors collected or there is an uneven azimuthal distribution. The resultant wind vector is then split into zonal (East - West) and meridional (North - South) components. This yields a representative wind velocity for a two-hour interval for each height gate. The two-hour

window is incremented through the data in steps of one hour to provide an hourly-spaced time-series of winds.

3.6 Advantages and Disadvantages to VHF Meteor Radar

There are many advantages to using meteor radar for making observations of the mesosphere, these are:

1. They are very simple and therefore are reliable and use a low amount of power. This means that long data sets over many years may be obtained with little maintenance.

2. They are relatively cheap systems to set up ($\sim$ £100,000 for a basic system) and they require little maintenance and therefore are low in cost to run.

3. They have a continuos operation, both over a typical day and over many years. This is because they are unaffected by conditions such as hours of darkness, cloud cover etc.

4. They have a robust well-understood scattering mechanism. This gives reliable data.

5. They have a high resolution in time, height and winds.

There are also disadvantages to using meteor radar these are:

1. They have a narrow height coverage of only $\sim$ 80 - 100 km, compared to the depth of the middle atmosphere that has a height range of 10 - 100 km.

2. They are restricted to measurements in one location only. This is not ideal when studying tides and planetary waves, which are global in scale.

3. Due to the large diameter of the meteor collecting volume ($>$ 400 km) smaller-scale features such as gravity waves, cannot be distinguished.

Finally we should note that meteor radar can be used for other applications since it is not only used for wind measurements in the upper atmosphere. Meteor radar are particularly useful for meteor astronomy. This is because the meteor radar provide data such as meteor flux rates, particle size distributions, meteor entry speeds etc. Meteor radar also provide daily temperature measurements in the upper atmosphere.

3.7 Summary

This chapter provided an introduction to meteor radar and the techniques used for obtaining horizontal wind measurements. Meteor radars are an ideal technique for studying the long-term trends and large-scale dynamics of the MLT region. The two radars used in this study were introduced. The nature and distribution of meteor echoes were described. How the data were collected and binned is also described along with the calculation of zonal and meridional horizontal winds from meteor data.

Chapter 4

The NASA EOS Microwave Limb Sounder on the Aura Satellite

4.1 The NASA "A-Train" and the Aura Satellite

The work in this thesis includes the analysis of temperature measurements from the Earth Observing System (EOS) Microwave Limb Sounder (MLS) instrument on Aura. The EOS programme consists of three core satellites - Terra, Aqua and Aura as well as several other smaller satellites. Aura (Latin for "breeze") has a design life of 5 years with an operational goal of 6 years. It currently flies in the same orbit as Aqua, CloudSat and CALIPSO. This constellation of satellites is referred to as the Afternoon Train, or "A-Train " for short.

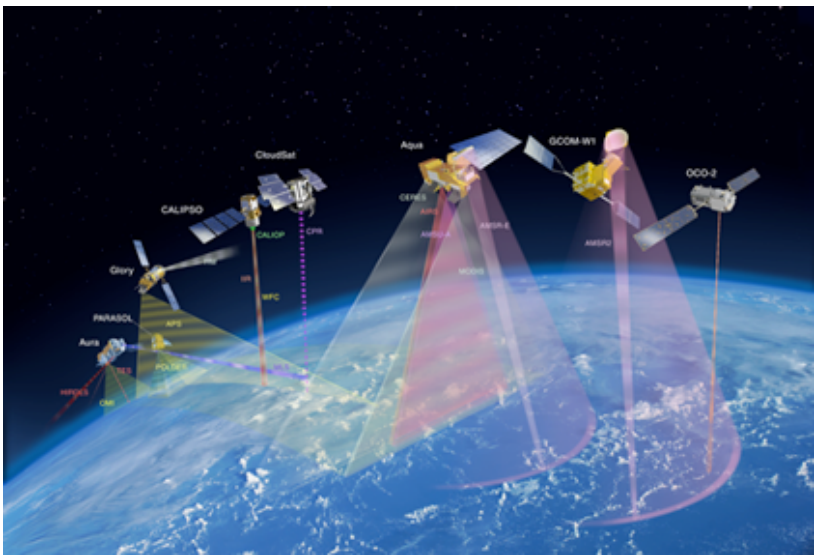

Figure 4.1: An artist's 3D concept of how NASA's A-Train constellation of satellites will fly in formation.

The A-Train satellites, shown in figure 4.1, travel one behind each other along the same orbital track. They cross the equator within a few minutes of each other at around 1:30 p.m. local time. The A-Train name was adopted by Aura project scientist Mark Schoeberl, after the famous 1930's jazz piece composed by Billy Strayhorn and popularized by the Duke Ellington Orchestra. Other satellites that are scheduled to join the A-Train are Glory in 2011, GCOM-W1 in 2011 and OCO-2 in 2013. PARASOL was launched into the A-Train orbit in 2004. In December 2009 it was lowered under the A-Train, enabling it to carry on sharing data with the A-Train satellites. It is gradually leaving the A-Train and at its current orbit is predicted to have completely left the A-Train at by the end of 2012 (see figure 4.2 for the full set of satellites).

Aura's scientific objectives are to answer three scientific questions (Waters et al., 2006):

1. To determine if stratospheric ozone chemistry is recovering

2. To quantify aspects of how composition affects climate change

3. To study aspects of pollution in the upper troposphere .

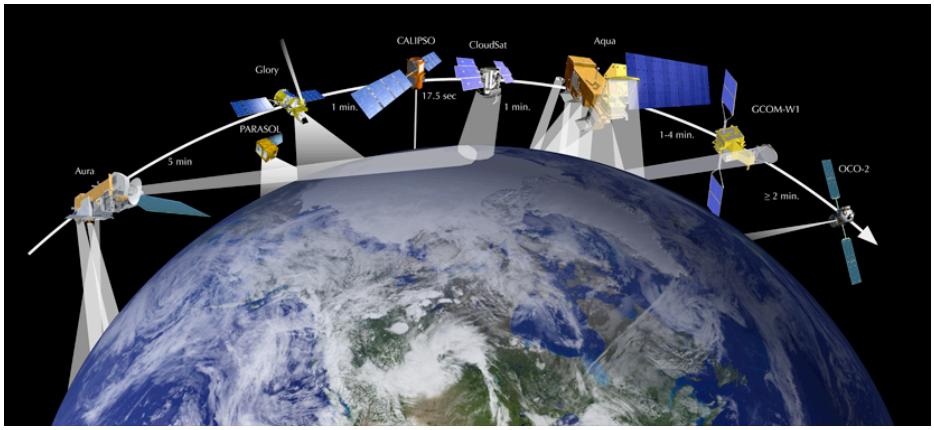

Figure 4.2: An artist's concept of how NASA's A-Train constellation of satellites will fly in formation.

4.2 EOS MLS

The Earth Observing System (EOS) Microwave Limb Sounder (MLS), onboard the National Aeronautics and Space Administration (NASA) Aura satellite launched on the 15^{th} July, 2004, uses the microwave technique to provide information on the Earth's upper troposphere, stratosphere and mesosphere.

There are four different instruments aboard the Aura satellite. These are, i) the Microwave Limb Sounder (MLS), ii) the High Resolution Dynamics Limb Sounder (HIRDLS) iii) the Ozone Monitoring Instrument (OMI), and iv) the Tropospheric Emission Spectrometer

(TES). Table 4.1 briefly outlines the measurements taken for each instrument. Figure 4.3 shows the location of these instruments on the Aura spacecraft. Figure 4.4 shows the vertical profiles of the measurements taken by the different instruments. The data used in Chapter 6 are temperature data from the MLS instrument.

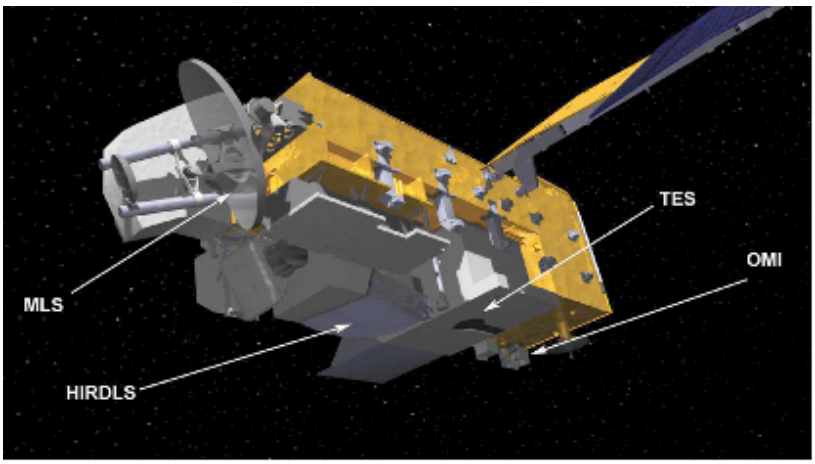

Figure 4.3: A schematic diagram of the Aura spacecraft showing the location of the four instruments HIRDLS, MLS, OMI and TES, after Schoeberl et al. (2006).

The EOS MLS instrument on Aura is an improved version of the earlier MLS instrument on board the NASA Upper Atmosphere Research Satellite (UARS) which was launched on the 12^{th} September, 1991. Daily measurements were made from the 29^{th} September, 1991 through to the 15^{th} March, 1994. From this point the measurements were made intermittently in order to conserve the lifetime of the MLS antenna and the last data obtained were recorded on the 25^{th} August 2001. The MLS instrument on UARS looked in a direction which was 90° from the UARS orbital velocity. The UARS orbit had a 57° inclination and this restricted the MLS instrument to measurements at latitudes from 34° on one side of the equator to 80° on the other. This significantly restricted the range of latitudes accessible to the UARS MLS instrument and reduced its ability to investigate global-scale features such as planetary waves.

The newer EOS MLS instrument on board the Aura satellite is improved over UARS MLS in having additional stratospheric measurements for chemical composition, better global and temporal coverage and resolution, better precision for measurements of temperature and the ability to measure to high latitudes in both hemispheres. This is due to advances being made in microwave technology since the time of UARS. Aura uses a polar orbit which allows nearly pole-to-pole coverage. Therefore, it is better for investigating planetary waves.

The EOS MLS instrument observes the thermal microwave emission of the atmosphere in five spectral regions from 115 GHz to 2.5 THz. The temperature measurements are taken from observations near the O_2 spectral lines at 118 GHz and 239 GHz. The 239-GHz line is the predominant source of temperature information in the troposphere while the 118-GHz line is the the predominant source of temperature information in the stratosphere and

Table 4.1: Aura Instruments and Measurements

Acronym	Name	Constituent	Instrument Description	Instrument Use
MLS	Microwave Limb Sounder	Profiles of Temperature, H_20, O_3, ClO, BrO, HCl, OH, HO_2, HNO_3, HCN, N2O, CO_3, cloud ice	Microwave limb sounder 118 GHz to 2.5 THz 3.5-14 km vertical resolution	MLS provides global measurements of temperature and GPH to provide information for the Earth's upper troposphere, stratosphere and mesosphere using the microwave technique.
HIRDLS	High Resolution Dynamics Limb Sounder	Profiles of Temperature, O_3, H_2O, CH_4, N_2O, CF_3Cl, CF_2Cl_2, $ClONO_2$, Aerosols	Limb IR filter radiometer from 6.2 μm to 17.76 μm 1.2 km vertical resolution up to 50 km	Provides high-resolution measurements that are important in improving the understanding the dynamics of the upper troposphere and stratosphere and provides additional stratospheric species not provided by the MLS.
OMI	Ozone Monitoring Instrument	Column O_3, SO_2, aerosols, NO_2, BrO, OClO, HCHO, cloud top pressure, O_3 profiles, UV-B	Hyperspectral nadir imager, 114° FOV, 270-500 nm, 13 × 24 km footprint for ozone and aerosols	OMI measures total column ozone along with information on the vertical distribution of ozone and other measurements.
TES	Tropospheric Emission Spectrometer	Profiles of Temperature, O_3, NO_2, CO, HNO_3, CH_4, H_2O	Limb (to 34 km) and nadir IR Fourier transform spectrometer 3.2-15.4 μm. Nadir footprint 5.3 × 8.5 km, limb 2.3 km	TES provides global measurements of the tropospheric chemical species and additional stratospheric products.

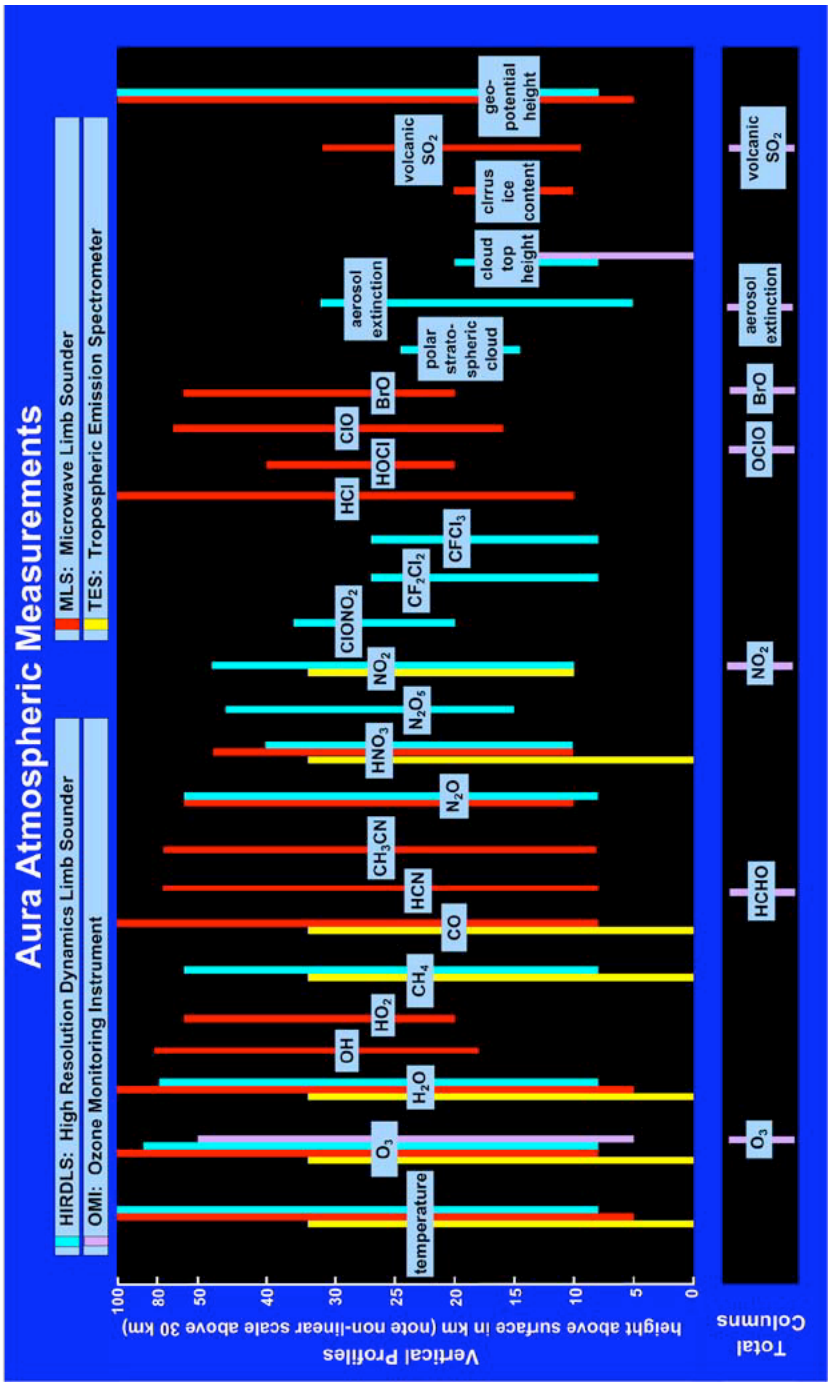

Figure 4.4: EOS Aura atmospheric measurements after Schoeberl et al. (2006). The temperature measurements are indicated by the first set of vertical lines.

above. The MLS instrument looks forward from the Aura spacecraft and scans the Earth's atmosphere vertically from the limb to $\sim$ 90 km every 24.7 s. The scans are synchronised to the Aura orbit so that the scans are made at the same latitudes each orbit. Temperatures are extracted from calibrated MLS limb radiances using the MLS version 2.2 (v2.2) level-2 software. Version 2.2 is the second public release of MLS data and has been in use since March 2007. The v2.2 files were chosen for use in the work presented in Chapter 6 over the earlier v1.5 files because the v2.2 files have twice the vertical resolution of the original v1.5 files. Data from August 2004 - March 2007 are also in the v2.2 data since they have been retrospectively processed using the v2.2 algorithms.

4.3 Data retrieval

Microwave limb sounding used by Aura observes millimetre and sub-millimetre wavelength thermal emissions (radiances) in the forward facing instrument field of view (FOV) as it scans through the atmospheric limb. This is a powerful remote sensing technique for gaining measurements of atmospheric parameters. Figure 4.5 presents a schematic diagram of this forward-looking limb-scan geometry.

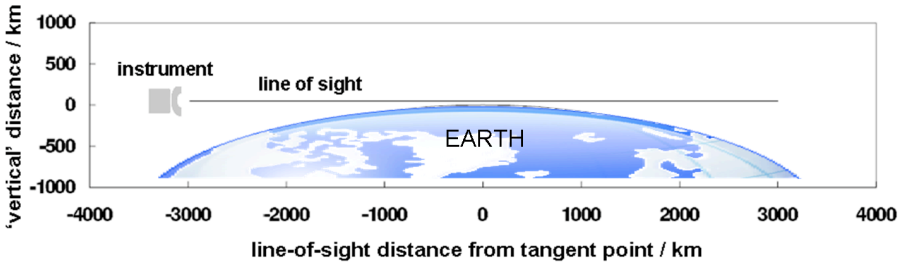

Figure 4.5: Orbit height and limb-scan geometry. The geometry shown is drawn to scale with the Aura satellite at a height of 705 km and the line of sight having a 50 km tangent height. The orbit plane is the plane of the page. Note that the instrument size is exaggerated.

The EOS MLS instrument consists of seven microwave radiometers, covering five different spectral regions. The signals from the radiometers are passed on to a number of different spectrometers. The spectral coverage of the instrument is shown in fig. 4.6. In the MLS data processing, radiance is measured in Kelvins and considered to be a *brightness temperature*. The brightness temperature is defined to be exactly equal to the temperature of a hypothetical black body completely filling the field of view of the EOS MLS instrument that would give the same radiance. As an example, figure 4.7 shows the individual channel positions and widths which define the filter resolution for the particular case of a simulated ozone line. A brightness temperature and radiance is calculated for each channel in the spectrometer and these are indicated on the figure.

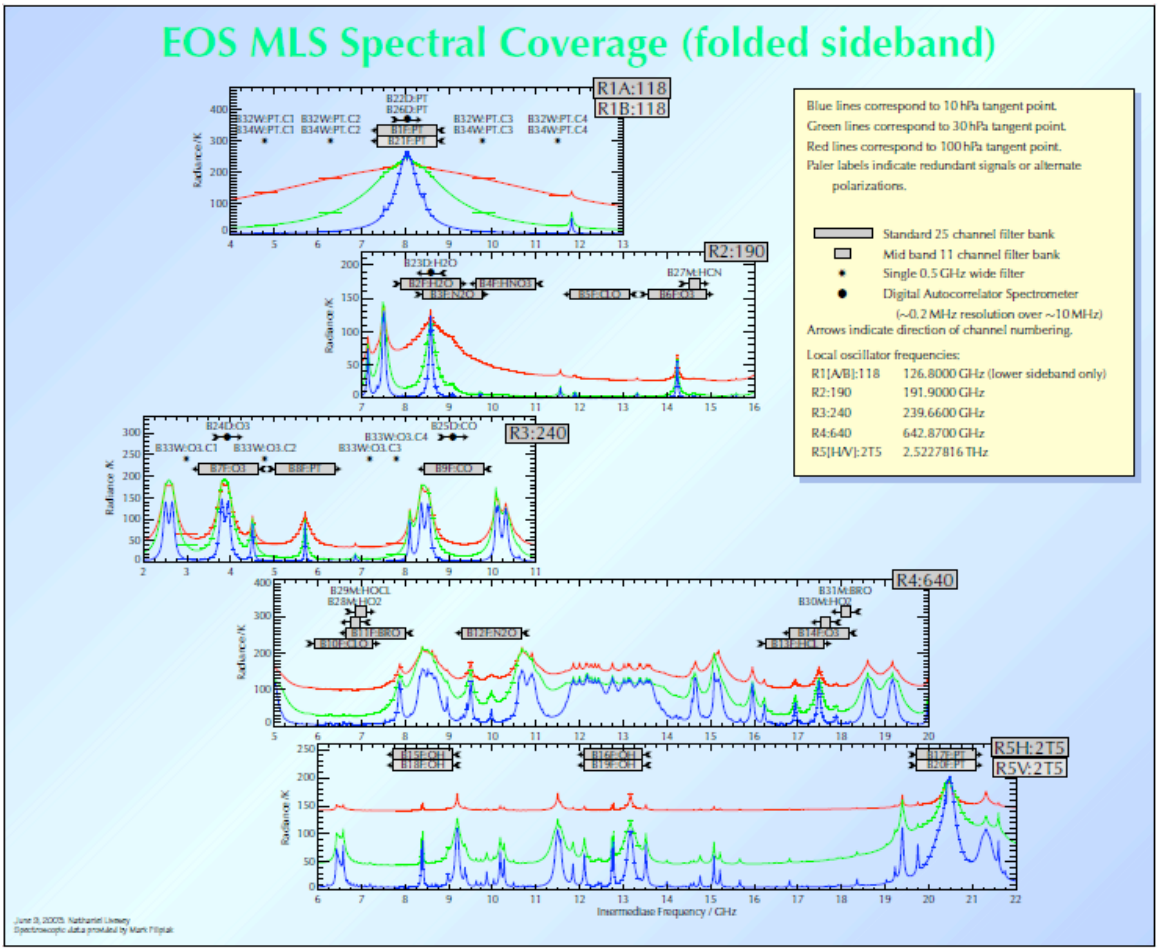

Figure 4.6: Atmospheric spectral regions measured by EOS MLS. There is a separate panel for each radiometer. The red, green and blue curves are the calculated atmospheric limb spectra at 100, 30 and 10 hPa tangent pressure corresponding to heights of ∼ 16, 24 and 32 km height. After Livesey and Snyder (2004).

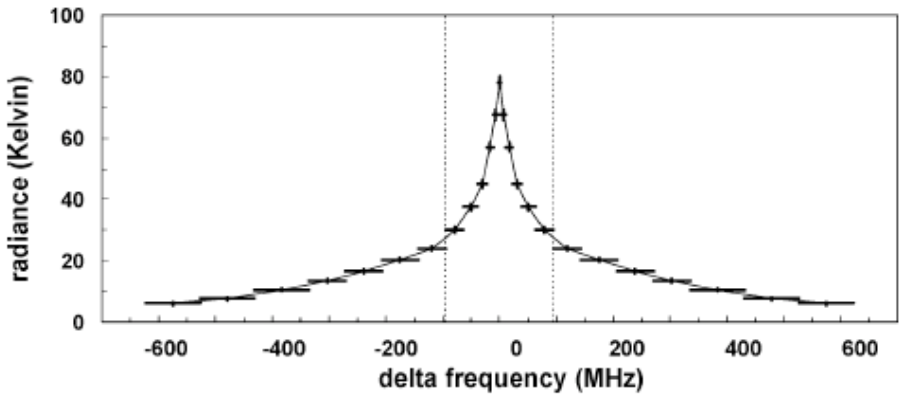

Figure 4.7: Illustrating coverage of the EOS MLS "standard" 25-channel spectrometer. Each filter in the spectrometer is shown as a horizontal bar whose width gives the filter resolution. The signal shown here is a simulated ozone line for a limb observation with tangent height in the lower stratosphere. The 11 filters that occur between the dotted lines are the "midband" spectrometers. After Waters et al. (2006)

4.3.1 The EOS MLS Instrument

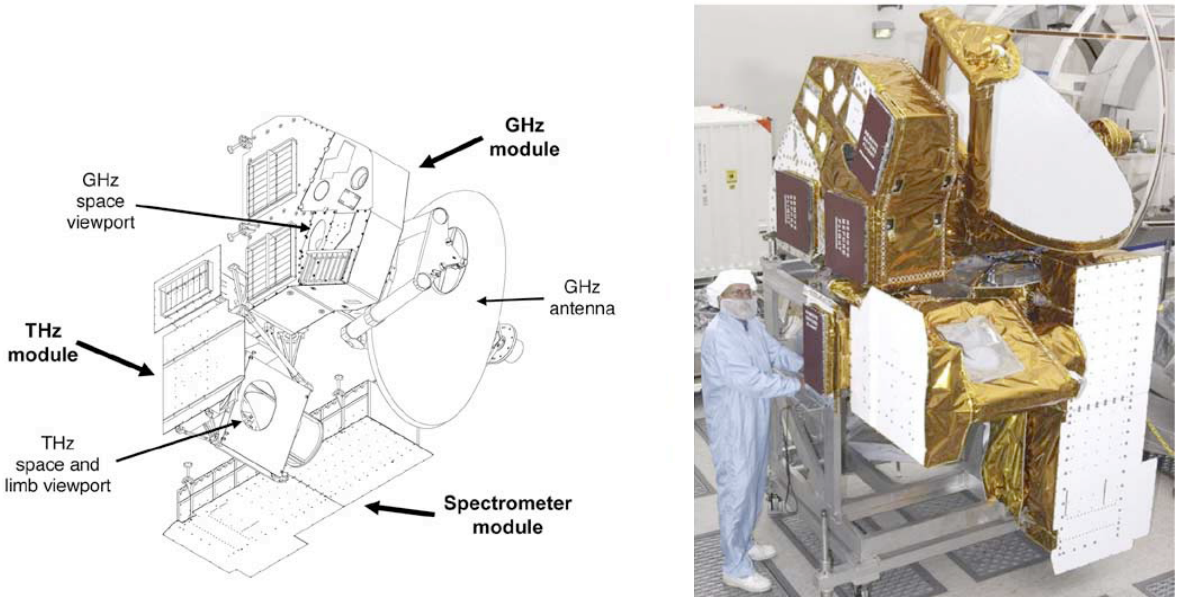

(a) (b)

Figure 4.8: a) A schematic diagram of the EOS MLS instrument and b) A photograph of the EOS MLS instrument. After Waters et al. (2006).

The EOS MLS instrument is assembled in three modules (see Fig 4.8 for a schematic and a photograph of the instrument):

1. the 'GHZ module' which consists of radiometers R1 - R4 and includes measurements of all constituents apart from the OH line. The R1 radiometer covering the strong 118-GHz O_2 line provides the temperature and tangent pressure measurements (see fig 4.2 for a full list of what the GHz module measurements are).

2. the 'THZ module' uses the 2.5-THz (R5) radiometer to measure the OH because of the reasonably clean spectral region around the pair of OH lines at 2.510 and 2.514 THz.

3. the 'Spectrometer module' consists of four types of spectrometers that have different spectral resolutions and bandwidths, see fig. 4.6 for the EOS MLS spectra coverage.

The GHz and THz antennas take one complete vertical scan between the surface and $\sim$ 95 km in about 20s. There is a difference in the GHz and THz scan rates. This is to allow the THz antenna more time to observe the upper stratosphere. After each scan 4.7 s are spent on calibration and antennae retrace activities. This gives a repeat period of about 24.7 s for each scan/calibrate/retrace sequence. This is called a *major frame*. The 20s limb scan is a continuous movement as opposed to the 'stop and stare' scan used on the UARS MLS. During the scan, 120 measurement integrations are performed, that pass the data from the

Table 4.2: EOS MLD radiometers and measurements

Radiometer	Primary measurements for which the radiometer was included in EOS MLS	Additional measurements that are provided, or contributed to
R1(118 GHz)	temperature, pressure	cloud ice, geopotential height
R2 (190 GHz)	H_20, HNO_3	cloud ice, ClO, N_2O, O_3, HCN, CH_3CN, volcanic SO_2
R3 (240 GHz)	O_3, CO	cloud ice, temperature, pressure, HNO_3, volcanic SO_2
R4 (640 GHz)	HCl, Clo, BrO, N_2O, HO_2	cloud ice, O_3, HOCl, CH_3CN, volcanic SO_2
R5 (2.5 THz)	OH	O_3, cloud ice, temperature, pressure

spectrometers to the data-handling system for transmission. Each integration time takes $\sim 1/6$s. These integration periods are known as *minor frames*.

4.3.2 How the radiances vary with height

The radiances retrieved vary with height. This is due to the varying density of the atmosphere with height. At high tangent point altitudes (the point along the ray path that is closest to the Earth's surface) little emission is observed due to low atmospheric density. As the ray path descends through the atmosphere the atmosphere becomes more dense and so emission is stronger. This continues as the scan moves to lower and lower heights until the atmosphere becomes opaque so that the emission from lower regions in the atmosphere is absorbed by the air above at higher altitudes and thus cannot be observed by the instrument. At this point the radiances are said to be *saturated* or *blacked out*. These saturated radiances are a measure of the temperature of the region of the atmosphere where the saturation takes place. Figure 4.9 shows a set of calculated radiances from the O_2 spectral band. The saturated radiances can be seen where the curves kink downwards and is described as the 'knee' of the radiance curves.

These MLS calibrated radiance observations are then converted into estimates of geophysical parameters such as temperature and composition by the use of 'retrieval' algorithms.

4.4 Data Processing and Products

There are three levels of MLS data processing that each produce corresponding levels of data products. The MLS calibrated radiance observations are known as Level 1 data. This Level 1 data is referred to as "Level 1B" since it distinguishes them from "Level 1A"

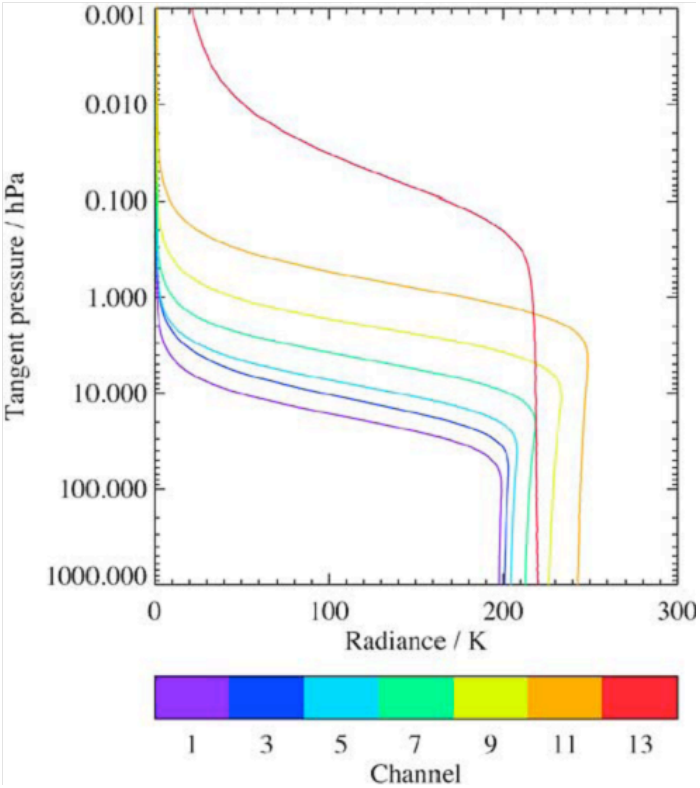

Figure 4.9: EOS MLS radiance profile of the R1A:118.B1F:PT band which is targeted on the O_2 line and used to measure temperature and tangent pressure. Only the radiances for the first 13 channels have been shown. The red lines correspond to the channels closest to the centers of the spectral lines. After Livesey et al. (2006)

datasets that do not include geolocation. Level 2 data describe vertical profiles of retrieved geophysical parameters along the instrument track, such as temperature. Level 3 data describe the profiles of geophysical parameters on latitude/longitude grids. Level 1B and Level 2 data files are produced on a daily basis whereas Level 3 data are produced on a monthly basis. The Level 2 geophysical data products are the output files of the version 2.2 data processing algorithms that are used to generate Level 2 data from the input Level 1 data (the calibrated microwave radiance observations). The Level 3 data is generated by the application of gridding and/or averaging algorithms to the Level 2 data.

The methods used to convert measurements of thermal limb emission (Level 1 data) into estimates of geophysical parameters (Level 2 data) are known as *retrieval algorithms*. In a retrieval algorithm a *state vector* is used to describe the aspects of the atmosphere and measurement system that affects the radiance measurements, this is done using *priori* information from climatological data sets in this case operational meteorological data from NASA's Global Modelling and Assimilation Office (GMAO), (Waters et al., 2006). Then a *forward model* is used. A forward model is a calculation which gives an estimate of radiances that would be observed by the instrument if the atmosphere were in a state given by the state vector. These predicted radiances are then compared with the actual radiances observed along with additional information from the forward model calculation to produce a better estimate of the state vector i.e. a state vector where the predicted radiances will be closer to the observed radiances. This is an iterative process which continuously refines the state vector until appropriate convergence has been achieved. The main components of this processing is shown in figure 4.10 after Livesey and Snyder (2004).

4.4.1 Data Usage

Once the data is processed to Level 2 data then the precision, resolution and accuracy are quantified and recommendations for data screening are then considered. The data quality document Livesey et al. (2006) gives information on file formats and contents as well as instructions on the proper use of MLS data products.

Precision, Resolution and Accuracy

Each MLS Level 2 data point is accompanied by a precision estimate. Precision quantifies random error of measurements which would average down if the measurement were repeated. This is from the propagation of radiometric noise and of uncertainties in measurements. If the retrieval does not improve the precision by a factor of two from its priori value, then it has failed to extract sufficient information from the radiances and the retrieved values will be influenced by the priori value. These precisions are set negative and the data shouldn't

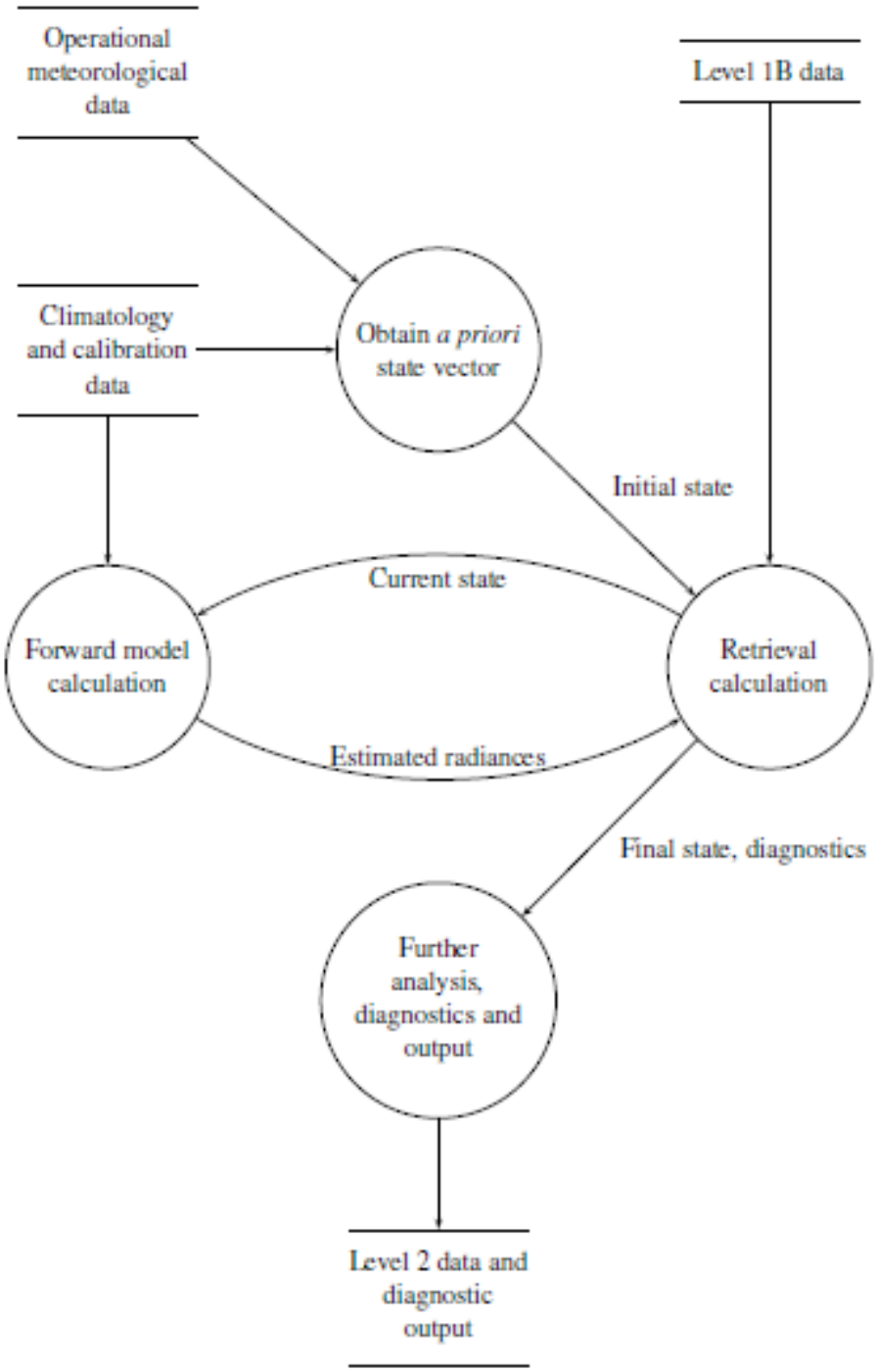

Figure 4.10: The essential components and data flow used in the data processing software for the EOS MLS Level 2 data. After Livesey and Snyder (2004)

be used for scientific studies.

The vertical resolution of the MLS temperature measurement is 5.3 km at 316 hPa (8 km), 5.2 km at 100 hPa (16 km), 3.5 km at 31.6 hPa (24 km), 4.3 km at 10 hPa (32 km), 6.2 km at 3.16 hPa (40 km) and 14 km at 0.01 hPa (81 km). Along track resolution is $\sim$ 170 km from 316 hPa (8 km) to 0.1 hPa (64 km) and degrades to 220 km at 0.001 hPa (97 km). The longitudinal separation is determined by the Aura orbit and is 10° to 20° over middle and low latitudes and much finer over the polar regions. Averaging kernels can be used to estimate vertical and horizontal resolution see Livesey et al. (2006) for more information on averaging kernels. The averaging kernel is identified by an identity matrix **A** and the block diagonal of **A** quantifies the resolution since the columns of **A** are the true values of the geophysical parameters and the rows of **A** are the measured values. Figure 4.11 shows the vertical resolution of the MLS temperature measurement by averaging kernels. The resolution is taken to be the full width at half maximum of these averaging kernels.

Systematic uncertainties occur due to instrumental issues such as spectroscopic uncertainty. Accuracy of the v2.2 temperature measurements is estimated by modelling the impact of uncertainties in measurement and retrieval parameters that could lead to systematic errors, and through comparisons with correlative data sets. For a further discussion on accuracy please see section 2.6 in Schwartz et al. (2008).

Data Screening

The pressure range recommended for scientific use is between 316 - 0.001 hPa (8 - 97 km). Values outside this range should not be used.

For every profile of temperature three quality metrics are output; Status flag, Quality field and Convergence field. Status is a 32 bit integer that acts as a bit field containing several "flags". Figure 4.12 shows these flags in more details. Consequently any profile for which status is an odd number should not be used. Even values of status indicate that the profile has been marked as questionable by the data processing software, usually because of the presence of thick clouds report, Schwartz et al. (2008).

Quality indicates how well the measured MLS radiances have been fit by the Level 2 algorithms. Larger values of quality generally indicate good radiance fits, whereas values closer to zero indicate poorer radiance fits and thus less reliable data. For temperature and GPH data only profiles with a quality value larger than 0.6 should be used in scientific study. This threshold value excludes 4% of profiles.

Convergence describes how well the retrieval algorithms fit to the measured radiances com-

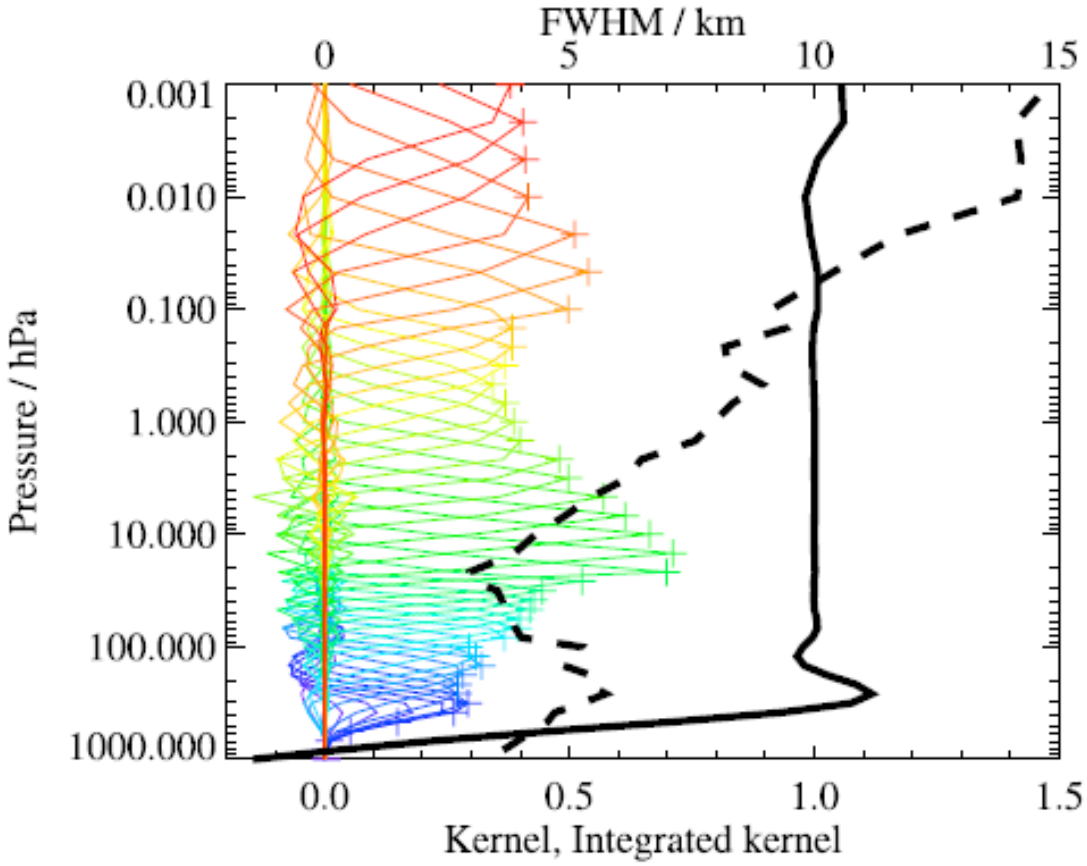

Figure 4.11: From Schwartz et al. (2008) MLS v2.2 temperature vertical two-dimensional averaging kernels. The variation of averaging kernels are small enough that this is representative of typical profiles, in this case for 35 ° N September climatology. The coloured lines show the contribution of atmospheric temperatures at each level, indicating the region of that atmosphere from which information is contributing to the measurements to a given retrieved temperature indicated by a plus sign of the same colour. The dashed black line indicates the vertical resolution in km and is determined by the full width at half maximum of the averaging kernels. The vertical solid black line shows the integrated area under the kernels. Values close to unity imply that the majority of the information comes from the atmosphere, whereas lower values imply contribution from a priori information.

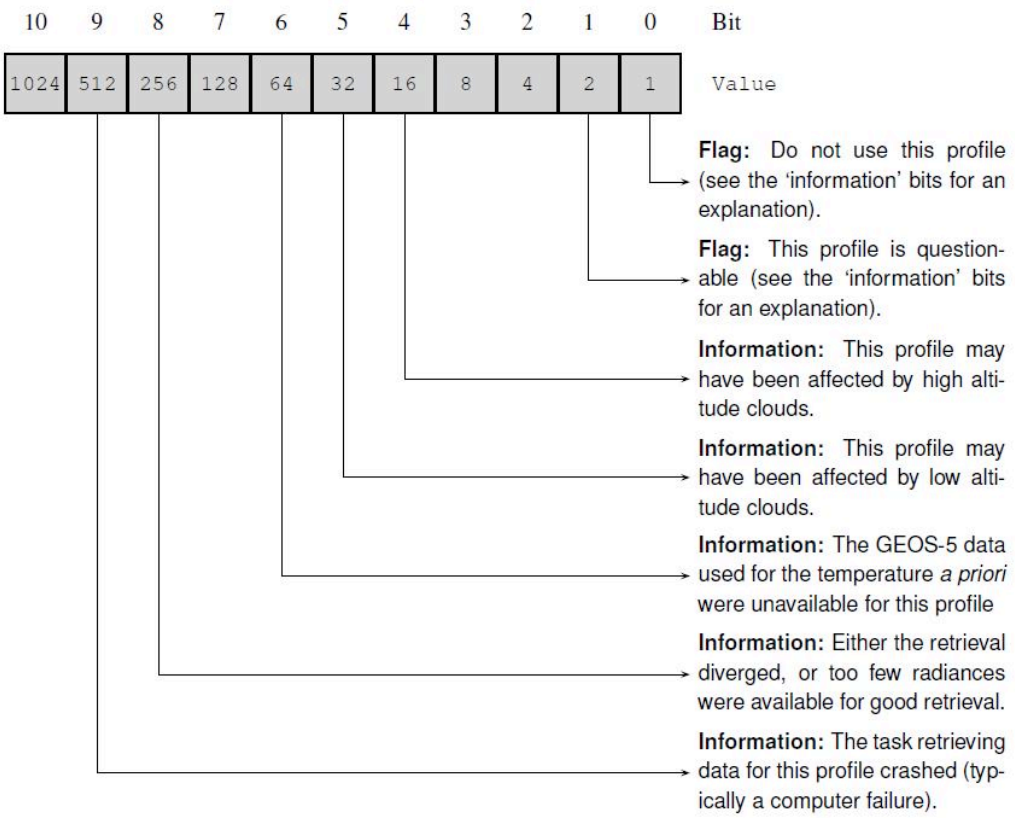

Figure 4.12: Description of the meanings of the different bits in the Status field. The bits not labelled are not used in the v2.2 data.

pared to the degree of fit to be expected between the two. Values of unity indicate good convergence. For temperature and GPH values a convergence threshold of 1.2 is used where use of values above this number is not recommended for scientific study. This discards 2% of profiles but only an additional 0.5% beyond those profiles already flagged by quality.

4.5 Aura's orbit and the EOS MLS Measurement Coverage

The Aura satellite is in a sun-synchronous orbit at 705 km above the Earth's surface. It has a 98° inclination and a 1:45 p.m. ascending equator-crossing time (the ascending node). The MLS instrument scans the limb in the orbit plane to provide latitude coverage from 82°N to 82°S on each orbit. The MLS scan plane is perpendicular to the tangent plane at the limb. The MLS limb scan is made in the forward direction (i.e., the MLS dish points in the direction of orbital motion) and the scans are made in an upward direction from the limb away from the planet. The tangent points of the limb scans are not perfectly perpendicular. At greater heights they are closer to the satellite than at the limb. However, in the Earth's

frame of reference this is compensated by the satellites forward motion.

A complete scan cycle takes $\sim$ 24.7 s. Because of the orbital velocity of the satellite this means that successive scans are spaced by 1.5° of the satellites orbit equivalent to $\sim$ 165 km along the orbital track, this equates to 240 limb scans per orbit. This is shown in figure 4.13 where the EOS MLS scan is shown with height as a function of time.

The individual scans made by MLS are kept symmetrical about the equator by use of accurate knowledge of the satellite's orbit. This ensures the same latitude sampling in the Northern and Southern Hemispheres, and on the ascending/descending orbits. This results in $\sim$ 3500 scans per day. The resulting global data sampling of the MLS instrument is shown in figure 4.14. The figure shows the sub-orbital track as a continuous line and the individual tangents points for limb scans a series of crosses. The tangent points are displaced from the sub-orbital track due to the motion of the Earth. This causes the satellite to move forward to the tangent point latitude.

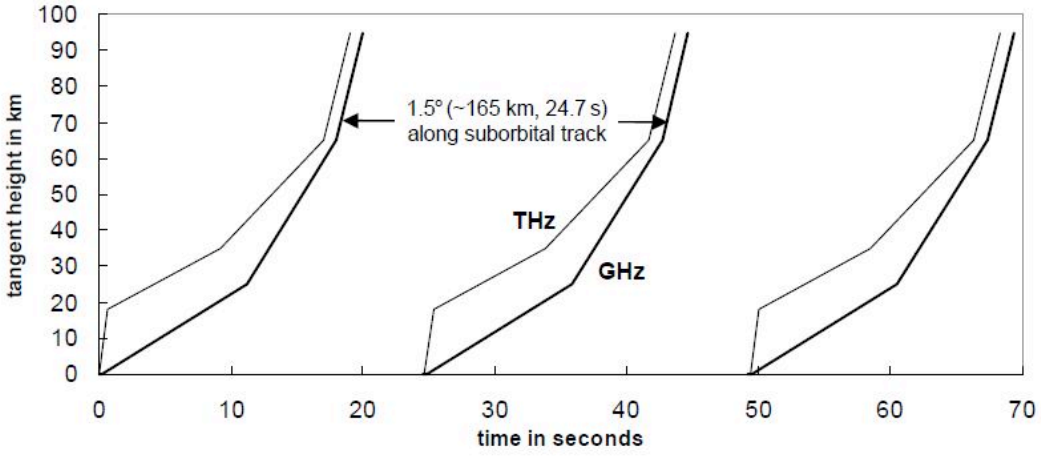

Figure 4.13: EOS MLS scan with height at tangent point as a function of time. Radiometric calibration (observation of cold space and a blackbody target) and retrace are performed during the 24.7 s gap between limb scans. Figure after Waters et al. (2004).

4.6 Advantages and Disadvantages of Satellite Remote Sensing

There are many advantages to using Satellite remote sensing for the study of planetary waves, these are:

1. Satellite measurements cover the whole globe giving a good temporal coverage of wave

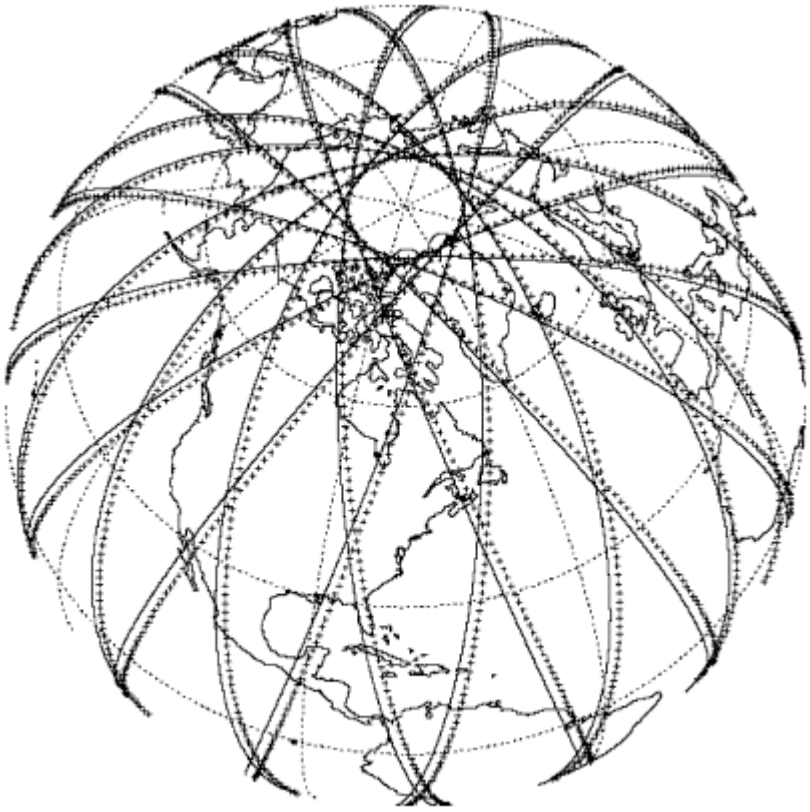

Figure 4.14: EOS MLS measurements for a 24 hour period. The crosses denote the location of the tangent points for individual limb scans. The continuous line is the suborbital track. This is displaced from the tangent points due to the Earth rotating as the satellite moves forward to the tangent point. The ascending orbits are those with the Southeast - Northwest tilt. There is the same daily coverage in the Southern Hemisphere as there is to the Northern Hemisphere shown here. Figure after Waters et al. (2004).

dynamics in both longitude and latitude.

2. Many instruments can be fitted to one satellite allowing measurements to be made of a vast amount of chemical species as well as temperature and GPH. This gains a good knowledge of the chemical state of the atmosphere as well as the dynamical state.

3. The height coverage spans from about 12 km up to 97 km. This allows simultaneous study of the troposphere, stratosphere and mesosphere.

There are also disadvantages to satellite remote sensing, these are:

1. There is poor spatial resolution, for example for the vertical resolution of the MLS temperature measurement at 81 km the vertical resolution is 14 km. This is too poor to allow the detection of finer structures in the mesosphere for example gravity waves.

2. Due to the Sun-synchronous orbit of the Aura satellite, migrating tides can not be detected in the data measurements and therefore at MLT heights the satellite is only suited to studying waves that are not Sun-synchronous and of a planetary-wave scale and period.

3. Due to high running costs and limited power reserves the satellite life-time is limited to only a few years, in the case of Aura it was predicted it would run for a maximum of 6 years.

4. When observing planetary waves with satellite data, due to the nature of the sampling and the mathematical techniques used to extract the wave, the data is subject to aliasing in space and time. When analysing satellite data this has to be taken into great consideration. See Chapter 6 for a more detailed explanation of this effect.

4.7 Summary

This chapter provided an introduction to satellite remote sensing and the EOS MLS technique used on the Aura satellite. This technique was chosen for this thesis since it is well suited to the study of planetary waves.

This chapter covered the Aura satellite itself and more specifically the MLS instrument. It focussed on how the MLS instrument detects and retrieves data values through radiances and processes them using processing algorithms to output temperature and GPH values for scientific use.

The data used in this study is the v2.2 "Level-2" data. The data screening that should be taken into consideration before the data is used for scientific use is discussed and the limitations on the data due to the satellite resolution, precision and accuracy are considered.

Finally the advantages and disadvantages of satellite remote sensing were recognised and in conclusion satellite techniques can provide a good global picture of the behaviour of planetary waves and so was used to study the 2-day wave as a climatology in this thesis.

Chapter 5

The 2-day wave in the Arctic and Antarctic mesosphere and lower thermosphere

5.1 Introduction

There have been comparatively few studies reported of the 2-day planetary wave in the middle atmosphere at polar latitudes. Here we report on a study made using high-latitude meteor radars at Rothera in the Antarctic (68°S, 68°W) and Esrange in Arctic Sweden (68°N, 21°E). Observations from 2005 - 2008 are used for Rothera and from 1999 - 2008 for Esrange. Measurements were made of horizontal winds at heights of 80 - 100 km. The radar winds distinct summertime and wintertime 2-day waves. The Antarctic summertime wave occurs with significant amplitudes in January - February at heights between about 88 100 km. Horizontal wind monthly variances associated with the wave exceed 160 m^2s^{-2} and the zonal component has larger amplitudes than the meridional. In contrast, the Arctic summertime wave occurs for a longer duration, June - August and has meridional amplitudes larger than the zonal amplitudes. The Arctic summertime wave is weaker than that in the Antarctic and maximum monthly variances are typically 60 m^2s^{-2}. In both hemispheres the summertime wave reaches largest amplitudes in the strongly sheared eastward zonal flow above the zero-wind line and is largely absent in the westward flow below. The observed differences in the summertime wave are probably due to the differences in the background zonal winds in the two hemispheres. The Antarctic and Arctic wintertime 2-day waves have very similar behaviour. The Antarctic wave has significant amplitudes in May - August and the Arctic wave in November - February. Both are evident across the full height range observed. This work has been published as; V. M. Tunbridge and N. J. Mitchell. The two-day wave in the Antarctic and Arctic mesosphere and lower thermosphere. *Atmospheric Chemistry and Physics*, 9(17): 6377-6388, 2009.

5.2 Data Analysis

The data analysed in this paper were obtained from two meteor radars located at Rothera (68°S, 68°W) in the Antarctic and Esrange (68°N, 21°E) in Arctic Sweden. The Rothera radar has been in operation since February 2005 and the Esrange radar since October 1999. Both radars have been in continuous operation for most of the time since these dates.

Both radars are commercially produced All-Sky Interferometric Meteor Radar (SKiYMET) Very High Frequency (VHF) systems that operate in an 'all-sky' configuration with radiated power being largely independent of azimuth. The radars have height and time resolutions of about 1 km and about 1 hour, respectively. See Hocking et al. (2001) and Mitchell et al. (2002) for details. The radars operate continuously, generating hourly values of zonal and meridional winds at heights of $\sim$ 80 - 100 km. This height range is split into six independent height-gates with depths of 5, 3, 3, 3, 3, 5 km. However, the vertical distribution of meteor echoes is strongly peaked at a height of $\sim$ 90 km and the meteor counts decrease above and below this height. To allow for this, in each height-gate the average meteor echo height is calculated from all the meteors within that gate. This yields heights of 80.8, 84.7, 87.5, 90.4, 93.3 and 97.1 km, as the mean heights of all the meteor echoes falling within each of the above six height gates. There is very little variation in the distribution of echo heights with time and so these values are used throughout the data set

For each month of data a variance value was calculated from the bandpassed horizontal winds in each height gate. The winds were bandpassed between 1.6 and 2.8 days. This variance is taken as a proxy for the activity of the 2-day waves in each height gate for the month in question. This was done for both zonal and meridional winds. Variance is a useful quantity because it is proportional to wave kinetic energy density per unit mass. However, it is also useful to relate this to wave amplitudes. For a sine wave, wave amplitude is equal to the square root of two times the variance. This means that variances of 20, 60, 100 and 140 m^2s^{-2} correspond to wave amplitudes of 6.3, 11.0, 14.1 and 16.7 ms^{-1} . Note that there may be significant short-term variability of the 2-day wave within each month. The monthly variance (and its equivalent amplitude) represents the average level of wave activity for that month.

5.3 Results

5.3.1 General characteristics of the polar 2-day waves

The occurrence of 2-day waves in the mesosphere lower thermosphere (MLT) region observed by the radars can be investigated by the use of spectral analysis. Figure 5.1 presents a

wavelet analysis of meridional winds over Rothera and Esrange for the years 2005 to 2008. These years are chosen because they are the ones for which simultaneous observations were made over both Rothera and Esrange. A Morlet wavelet was used with 6 cycles of the wave contained within a Gaussian envelope. This wavelet was chosen because it has a similar morphology to the episodes of planetary-wave activity often reported in the MLT. The results are for a height of 93.3 km. The figure reveals that there is a rich field of planetary-wave activity over both Rothera and Esrange. Planetary-wave activity can be seen to occur in strong intermittent bursts and to have wave periods from less than 2 days to more than 10 days. If we consider waves with periods near 2 days, it can be seen that the bursts are of relatively short duration, often lasting no more than 10 days or so. Significant wave amplitude is present at wave periods from about 1.5 to near 3 days. Wave activity appears to be strongest around the summer and winter solstices and significantly weaker around the equinoxes. We will describe these waves with period near 2 days as "2-day waves".

To determine the period of the wave in different seasons, periods between 1.7 - 2.5 days were least squares fitted to zonal and meridional winds in a 12-day window. The period of the fitted wave was moved in 1 hour steps from 40 hours (1.7 days) to 60 hours (2.5 days). The wave period at which maximum amplitude occurred was recorded and taken to be the period of the 2-day wave in that window. This window was then incremented through the time series in steps of 3 days. This analysis was applied to the summer (June - August) and winter (December - January) months for each year in both hemispheres and for all height gates. The wave period determined from each fit was then averaged over the season to yield a seasonally-averaged wave period for the 2-day wave. A threshold wave amplitude of 10 ms^{-1} was used as a cut off in this seasonal averaging so that the wave period was only determined from intervals of strong wave activity.

The results of this analysis suggest that in Antarctic summer, the average wave period is 51.1 hours (2.13 days). In Arctic summer the average wave period is 54.7 hours (2.28 days). In winter, the wave period maximises with a period of 52.7 hours (2.20 days) in the Antarctic and 54.5 hours (2.27 days) in the Arctic. The uncertainty in these wave periods is ~ 1 hour. These results are in general agreement with the observations described in Chapter 2 Section 2.5.

To examine the 2-day waves in more detail, the wind time series were bandpassed as described in Sect. 5.2. The filter was an elliptical type with the 99% high/low cut-off frequencies corresponding to periods of 1.6 and 2.8 days. We assume that wave activity within this period band is dominated by the 2-day waves of interest (note that at the latitude of Rothera and Esrange the inertial period is approximately 0.54 days and so there will be no significant gravity-wave activity within the frequency band selected for the filter).

Figure 5.2 presents the results of this analysis in the case of meridional winds recorded over Rothera and Esrange, respectively, in 2007. The figure shows that wave activity is present

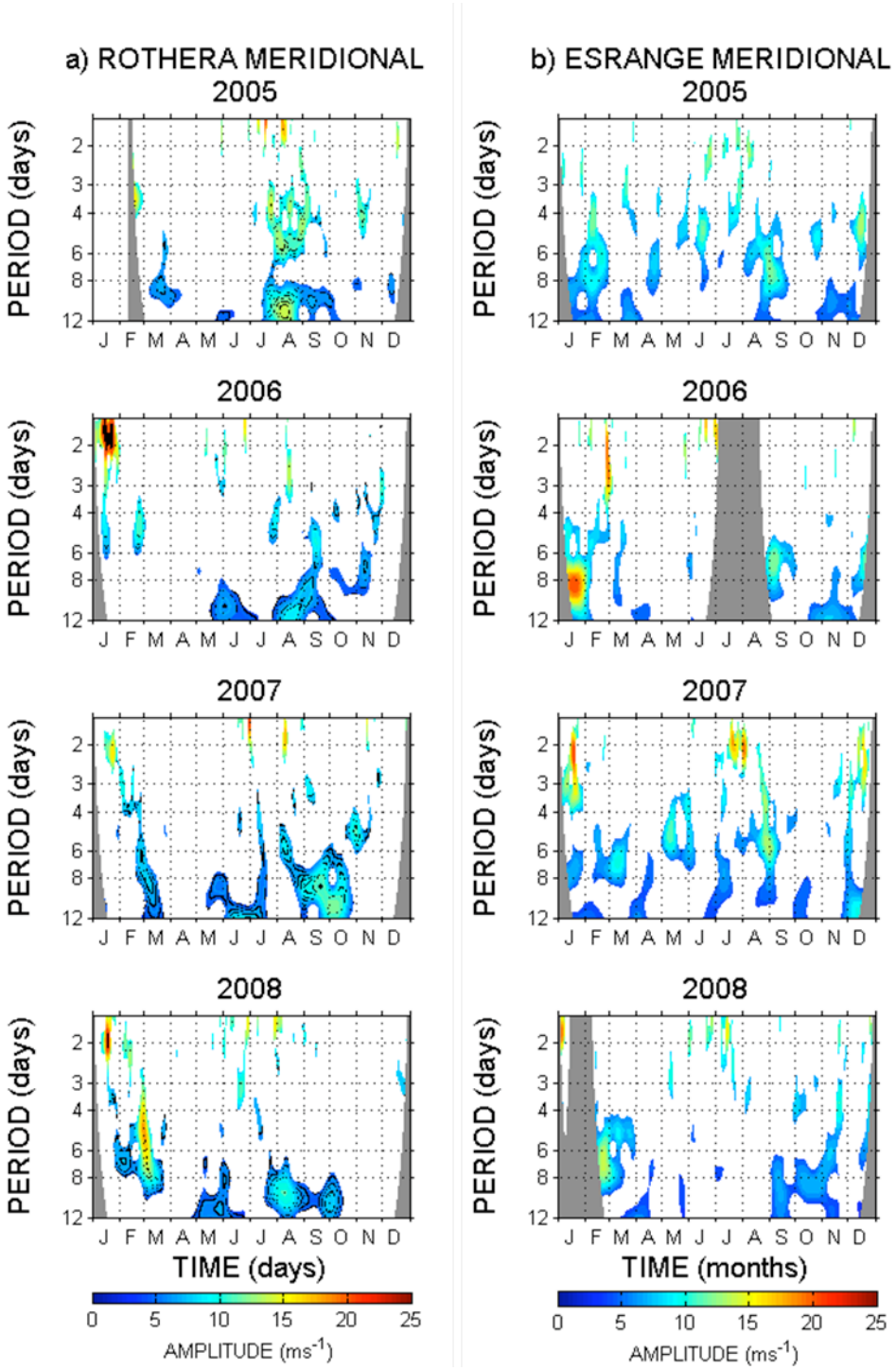

Figure 5.1: Wavelet analysis of meridional winds as a function of time at a height of $\sim$ 93 km a) over Rothera in 2006, b) over Esrange in 2007. The signal is only plotted above the 95% confidence level.

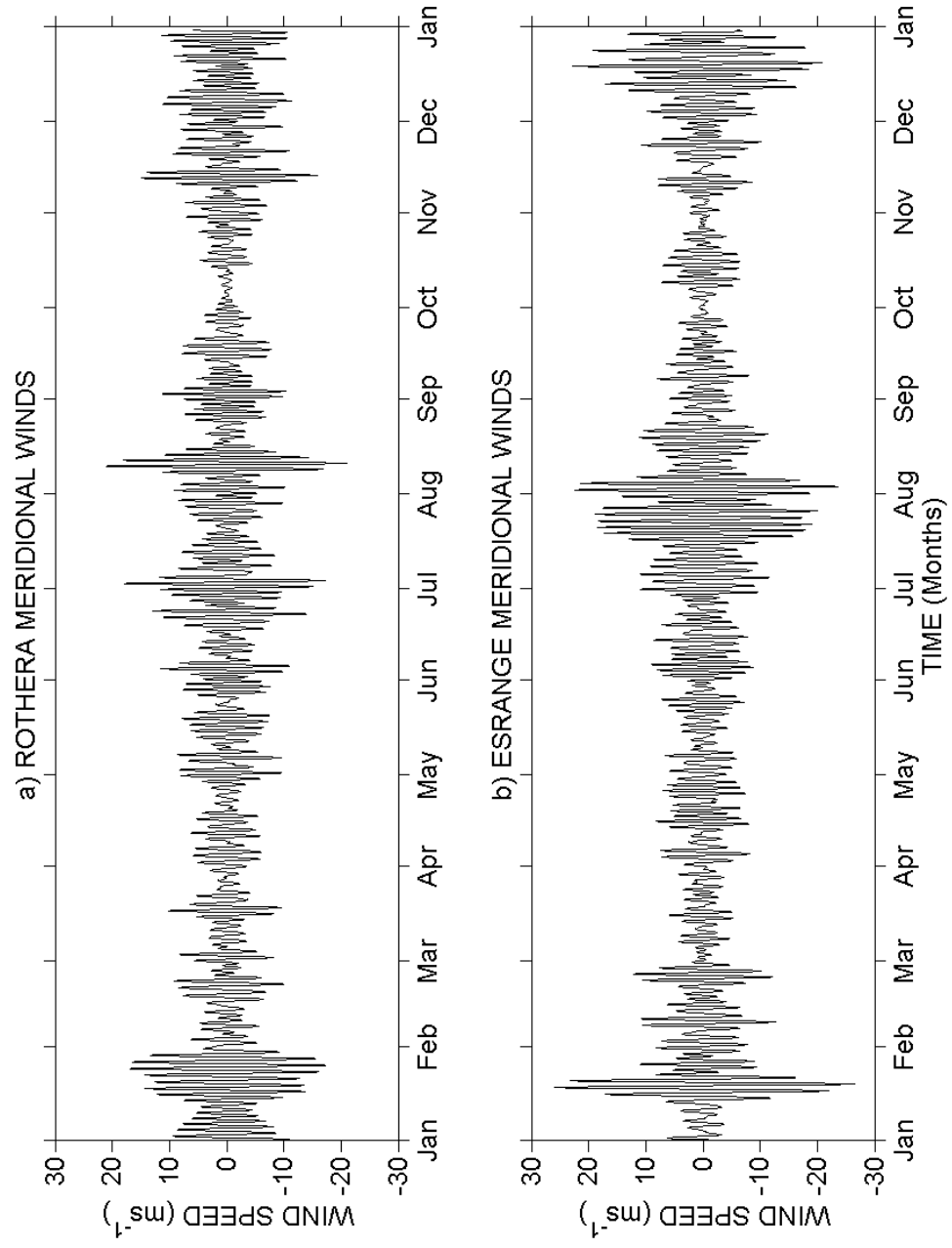

Figure 5.2: Bandpassed meridional winds as a function of time at a height of $\sim$ 93 km, for 2007, a) over Rothera, b) over Esrange. The data have been bandpassed between periods of 1.6 and 2.8 days.

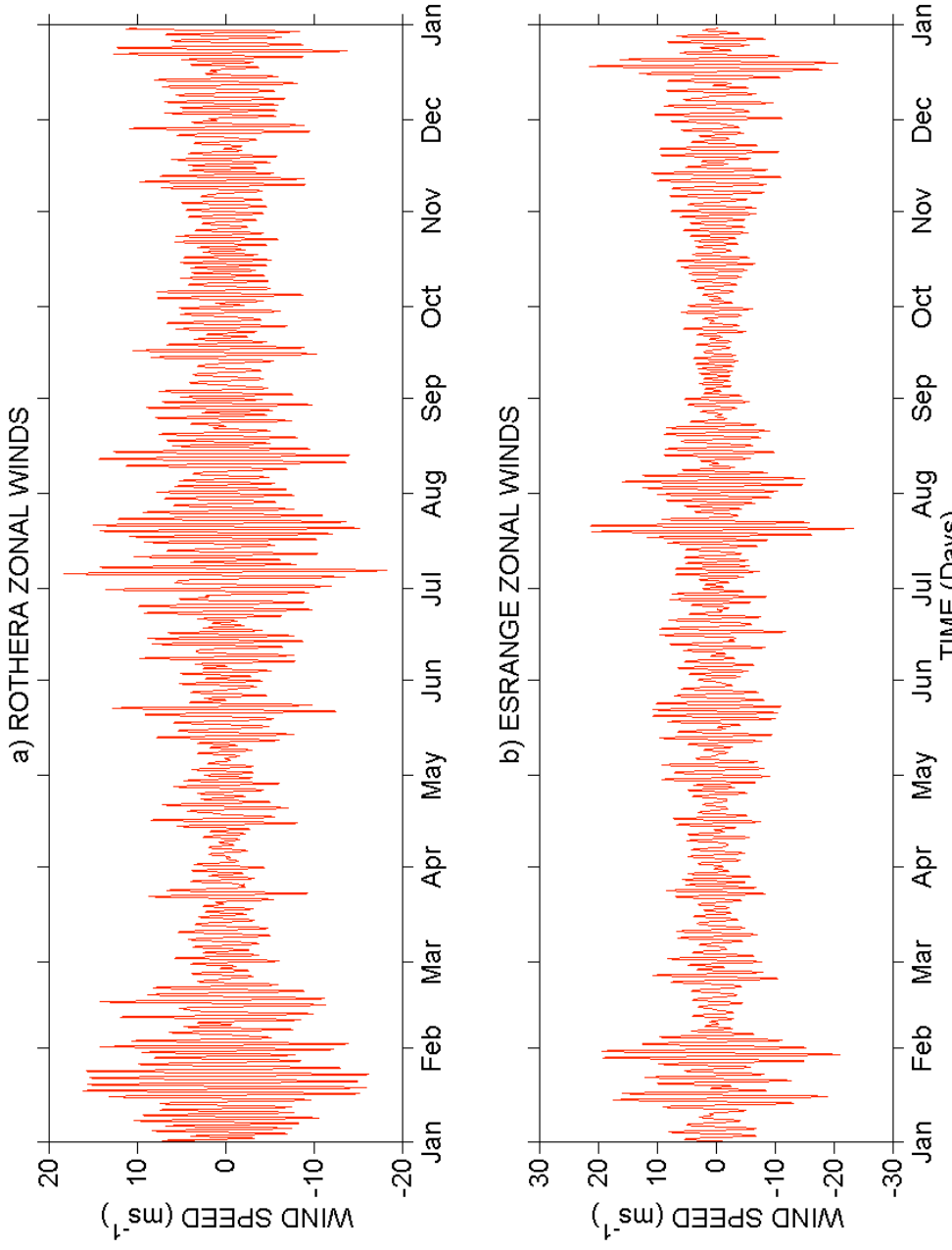

Figure 5.3: Bandpassed zonal winds as a function of time at a height of $\sim$ 93 km, for 2007, a) over Rothera, b) over Esrange. The data have been bandpassed between periods of 1.6 and 2.8 days.

throughout the year in this period range, but that strong bursts of wave activity occur only in winter and in late summer. For example, over Rothera amplitudes exceed 10 ms^{-1} in winter (June - August) and in summer (December - January). Similarly, over Esrange wave amplitudes exceed 10 ms^{-1} in winter (December - January) and in summer (July - August). The zonal amplitudes reveal a similar pattern of behaviour, shown in Figure 5.3, although the zonal amplitudes are smaller in the Arctic summer and larger in the Antarctic summer.

We can quantify the duration of bursts of activity of the 2-day wave by noting the length of time a particular burst of activity has an amplitude above a particular threshold. If we consider a threshold amplitude of 10 ms^{-1}, we find that in summer there were 26 separate bursts of wave activity with amplitude greater than this threshold in the 13 summer seasons observed (4 summers over Rothera and 9 over Esrange). Here we define summer as December, January and February (Rothera) and June, July and August (Esrange). In these 26 bursts, 8 had durations < 5 days, 13 had durations of 5-10 days, 3 had durations of 10-15 days and only 2 had durations > 15 days.

There were also 13 winter seasons observed with 20 separate bursts of wave activity in which amplitudes exceeded 10 ms^{-1} . Here we define winter as June, July and August (Rothera) and December, January and February (Esrange). In these 20 winter bursts, 10 had durations < 5 days, 6 had durations of 5-10 days, 2 had durations of 10-15 days and 2 had durations > 15 days. This suggests that the bursts of wave activity are on average of longer duration in summer than in winter.

To investigate the vertical structure of the summer and winter waves, data from the six height gates were bandpassed as above and then used to produce time - height contours of zonal and meridional winds over each site. Figure 5.4 presents two examples of this analysis for periods of strong wave activity evident in Fig.5.2. Figure 5.4a presents contours of the summertime meridional wind over Rothera in the Antarctic for 1^{st} December 2006 to 28^{th} February 2007. Figure 5.4b presents contours of the summertime meridional wind over Esrange for 1^{st} June 2007 to 31^{st} August 2007. These intervals are presented as being typical of summertime 2-day wave activity observed in bursts over these two sites. Several distinguishing characteristics are apparent from the examples, i) the wave activity occurs in strong bursts with duration of 10 to 20 days, although wave activity is present throughout the whole height-time interval, ii) the phase fronts of the wave are effectively vertical, implying a long vertical wavelength, iii) in the Antarctic the wave only reaches large amplitudes ($>$ 10 ms^{-1}) at heights above about 90 km. In the Arctic the wave maximises at heights of 90 - 95 km and decays above this height.

Figure 5.5 presents similar examples of this analysis for data representative of the winter season. Figure 5.5a presents contours of the wintertime meridional wind over Rothera for 1^{st} June 2007 to 31^{st} August 2007. Figure 5.5b presents contours of the wintertime meridional wind over Esrange for 1^{st} December 2006 to 28^{th} February 2007. These intervals

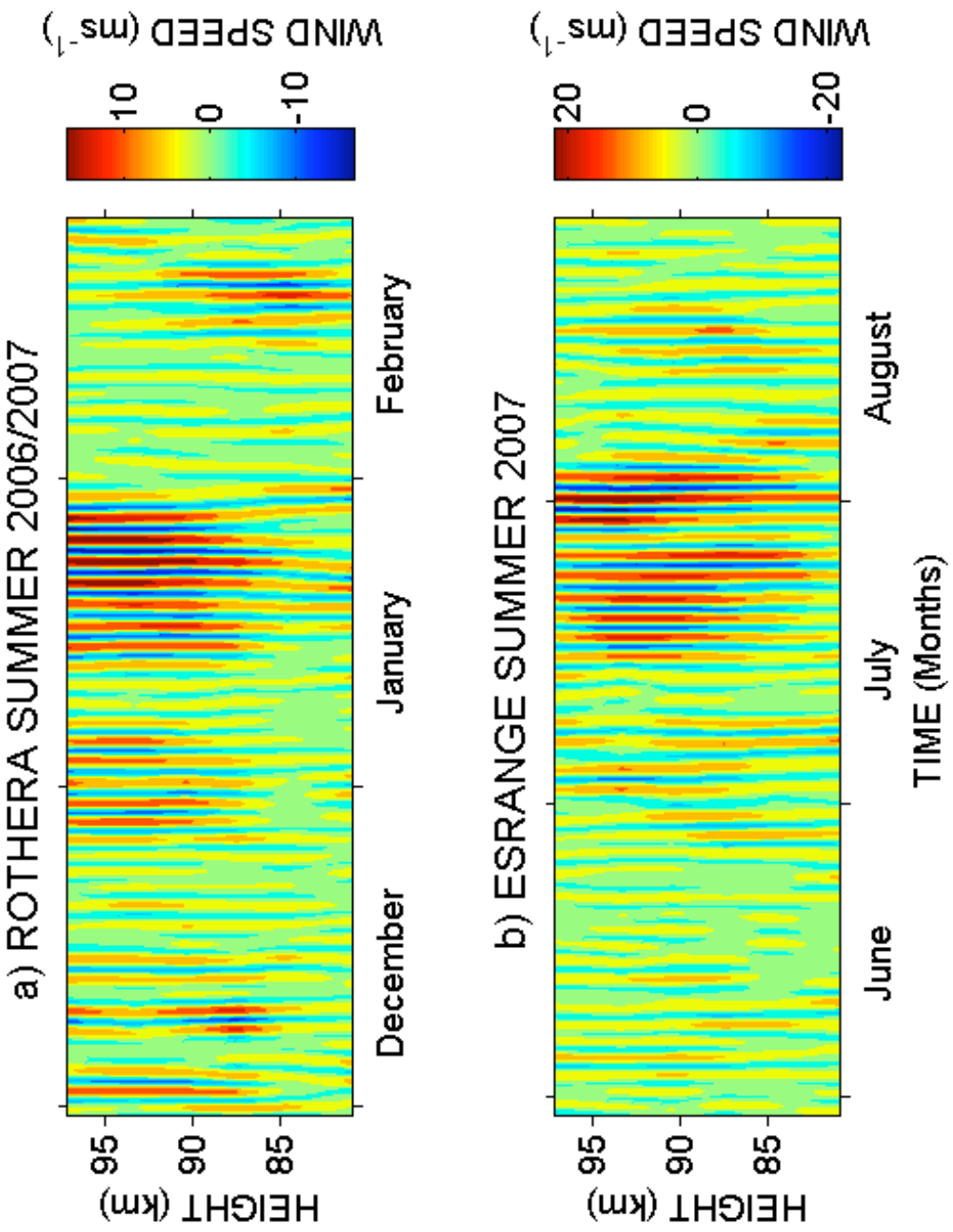

Figure 5.4: Bandpassed meridional winds as a function of time and height during summertime 2007, for heights of $\sim$ 80 - 97 km, a) over Rothera, b) over Esrange. The data were bandpassed between periods of 1.6 and 2.8 days.

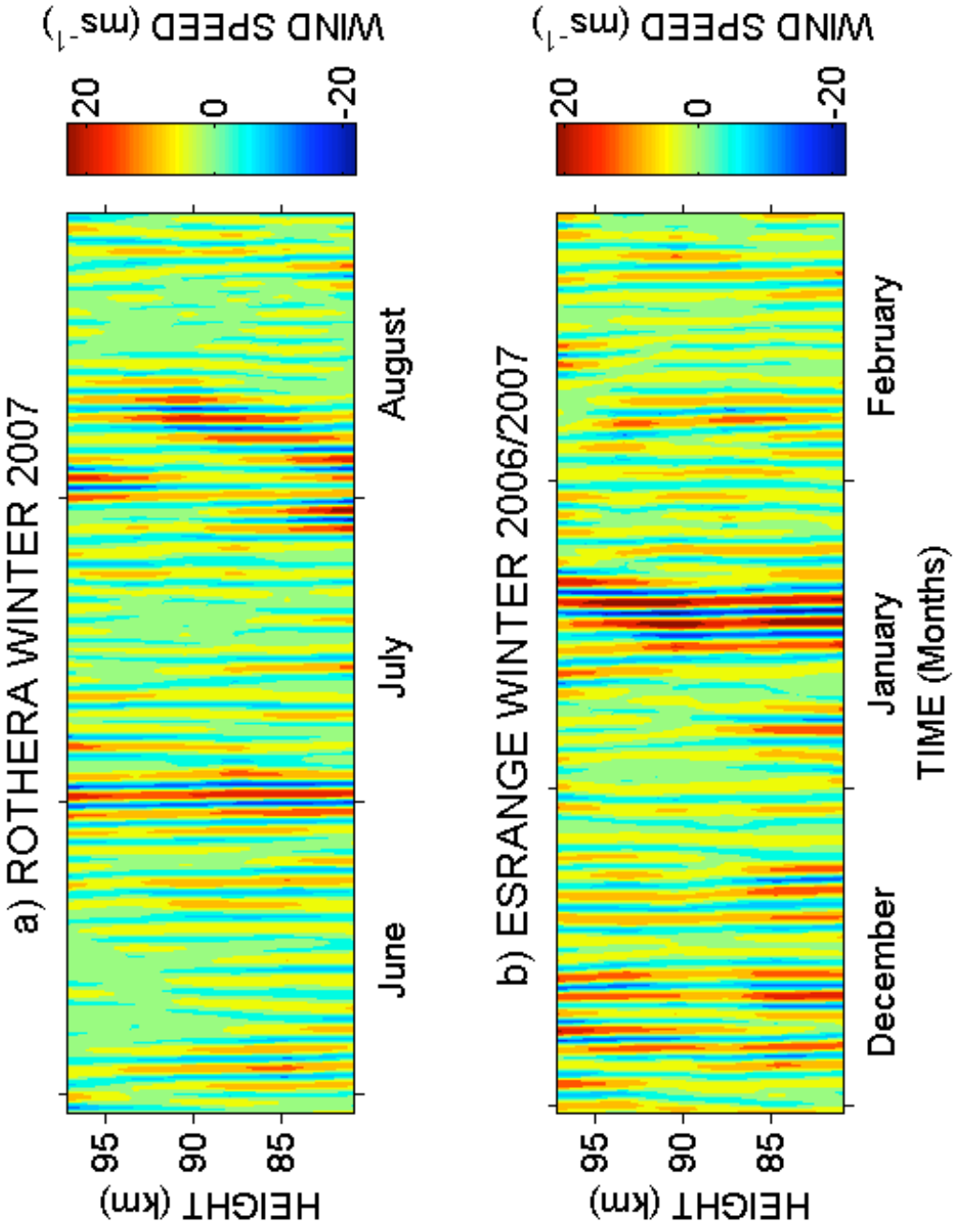

Figure 5.5: Bandpassed meridional winds as a function of time and height during wintertime 2007, for heights of ∼ 80 - 97 km, a) over Rothera, b) over Esrange. The data were bandpassed between periods of 1.6 and 2.8 days.

are again presented as being typical of wintertime 2-day wave activity. Several distinguishing characteristics are again apparent from the figures, i) the wave activity again occurs in bursts, although there is a suggestion that the bursts are of shorter duration than is the case in the summertime, ii) the phase fronts are again effectively vertical, implying a long vertical wavelength, iii) in contrast to the summertime wave, the wave activity occurs across the whole height range observed and does not seem to maximise in a particular height range.

5.3.2 Climatology of the polar 2-day waves

From the results presented in the previous Section it is apparent that there is a seasonal cycle in the 2-day wave activity. To investigate this further, Fig. 5.6 presents time-height contours of monthly variance at heights of $\sim$ 80 - 100 km for zonal and meridional components measured over Rothera from April 2005 to December 2008 (calculated as in Sect. 5.2). Indicated on each figure as open contours are the monthly-mean zonal winds for each year. From the figure it can be seen that there is a seasonal cycle in 2-day wave activity with a maximum in mid to late summer (December - February), a secondary maximum in winter (reaching largest variances in June - August) and equinoctial minima. These maxima correspond to the events described in Sect. 5.3.1. As suggested by the bandpassed results of Fig. 5.4, the summertime wave reaches largest variances at heights above $\sim$ 90 - 95 km. For instance, zonal monthly variances exceed 100 m^2s^{-2} in January 2006, 2007 and 2008, corresponding to monthly-mean amplitudes of > 14 ms^{-1} . In contrast, the wintertime wave can reach large variances across the entire height range observed. A considerable degree of inter-annual variability is also apparent. For example, the summertime 2-day wave is significantly stronger in 2006 compared to 2007 or 2008. This is particularly noticeable in the meridional component. However, in summer there is a clear tendency for the wave activity to be strong only in the regions of eastward winds above the zero-wind line. The wintertime 2-day wave also exhibits significant inter-annual variability.

Figure 5.7 presents a similar analysis applied to data from Esrange. The seasonal behaviour is generally similar to that observed over Rothera. Again, the summertime 2-day wave tends to maximise at heights above $\sim$ 90 km, above the zero-wind line, and the wintertime 2-day wave is present across the height range observed. Inter-annual variability is also very strong.

One difference evident between the results from Rothera and Esrange is that over Rothera the summertime 2-day wave has larger variances in the zonal component than in the meridional, whereas over Esrange the meridional variances are larger than the zonal variances.

To provide a clearer understanding of the seasonal behaviour of the 2-day wave, a composite-year analysis (i.e. a superposed-epoch or average-year analysis) was carried out using all available data. The monthly variance data have a log-normal distribution and so the com-

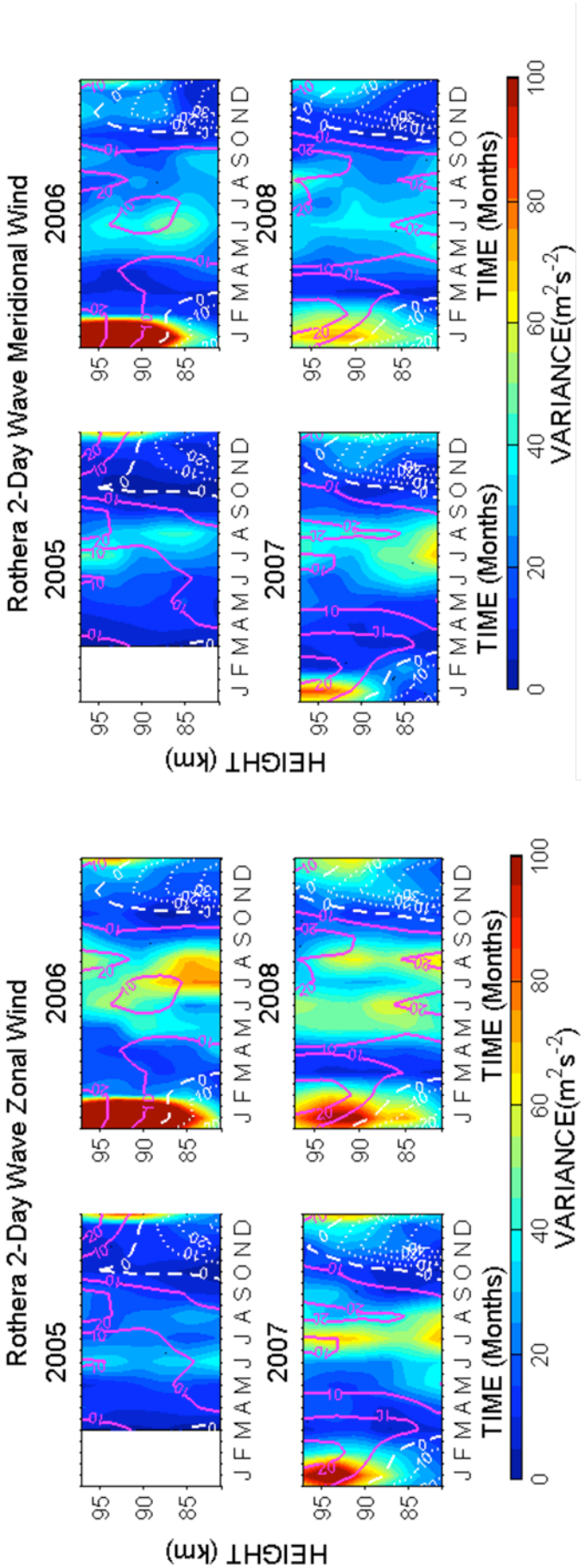

Figure 5.6: Time-height contours of the monthly variance of bandpassed horizontal winds over Rothera in the Antarctic between April 2005 and December 2008. The bandpass is between periods of 1.6 and 2.8 days. Also plotted are monthly mean zonal winds (open contours). The zero-wind contour is indicated by the heavy dashed white line.

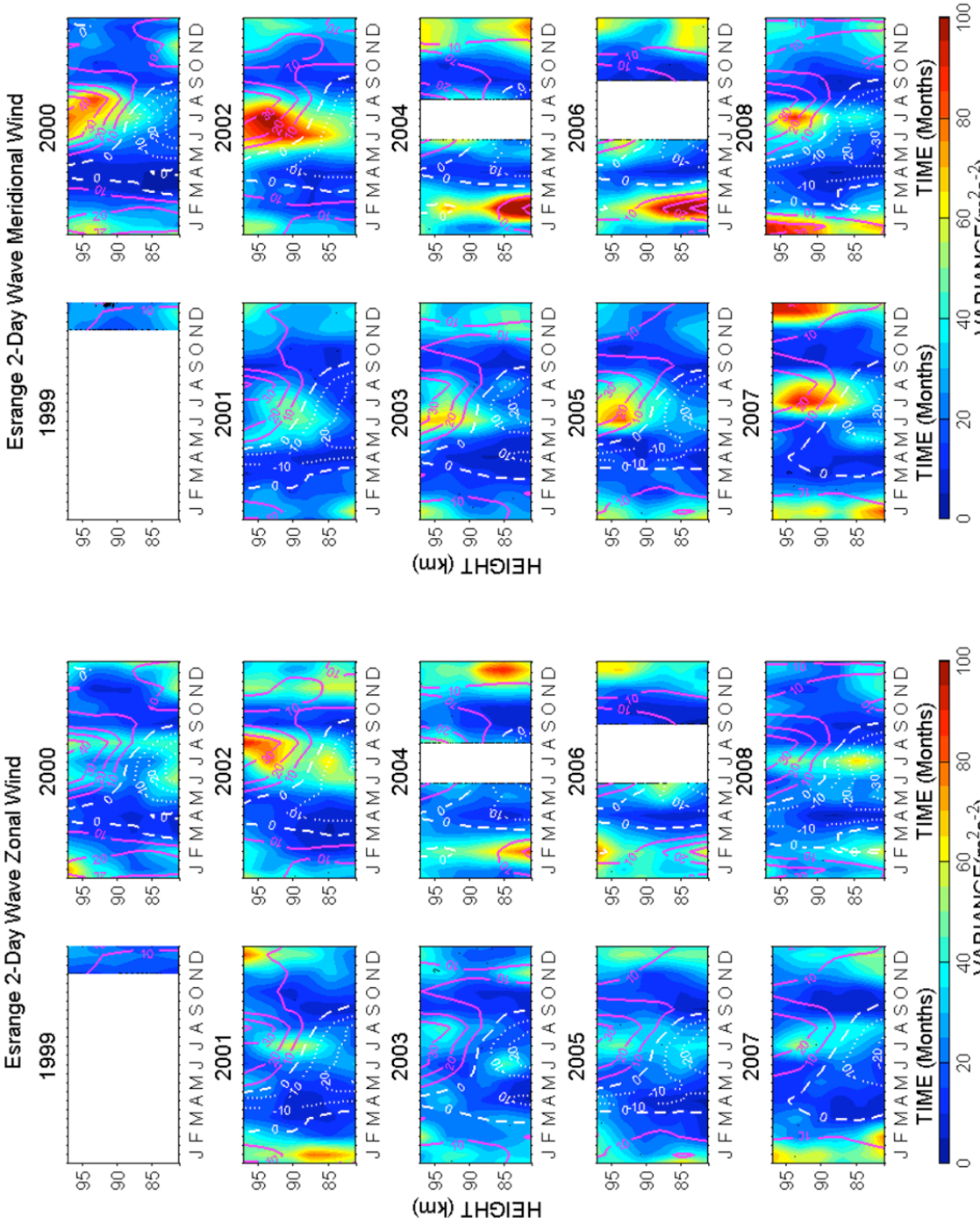

Figure 5.7: Time-height contours of the monthly variance of bandpassed horizontal winds over Esrange in the Arctic between October 1999 and December 2008. The bandpass is between periods of 1.6 and 2.8 days. Also plotted are monthly mean zonal winds (open contours). The zero-wind contour is indicated by the heavy dashed white line.

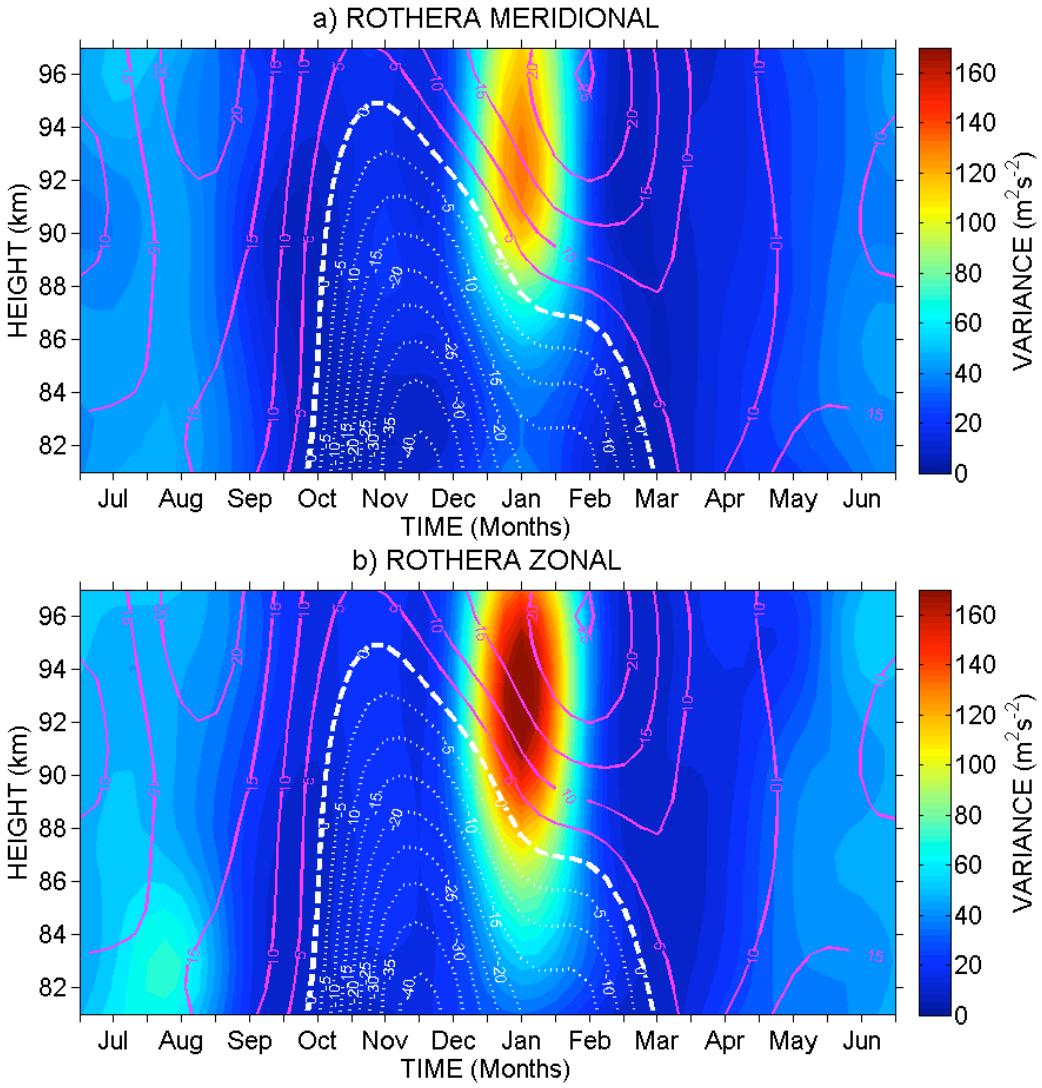

Figure 5.8: A composite-year analysis of the Rothera (Antarctic) variance data from Fig. 5.7 for a) the meridional component and b) the zonal component (filled colour contours). Also plotted are monthly mean zonal winds (open contours). The zero-wind contour is indicated by the heavy dashed white line. Note that the time axis is arranged so as to allow easy comparison with Fig. 10 (i.e. summer in the centre).

posite year cannot be produced by simply averaging the monthly variances in a particular height gate over all the years available. Instead, the variance was calculated for a given month and height gate by constructing a continuous time series of bandpassed winds for that height gate and month using data from all years. A variance was then calculated for this single time series and the procedure repeated for all other height gates and months. Figure 5.8a presents time-height contours of a composite-year analysis at heights of $\sim$ 80 - 100 km for the meridional component of winds over Rothera. The monthly-mean zonal winds were similarly averaged. Contours of these mean zonal winds are also plotted on the figure as lines. Figure 5.8b presents a similar analysis of the zonal component of the 2-day wave. Again, the monthly mean zonal winds are also plotted for comparison.

It can be seen from the figures that over Rothera the summertime wave has a much larger

variance than the wintertime wave. The summertime wave reaches variances above 160 m^2s^{-2} , at heights above $\sim$ 90 km in the zonal component. In fact, the summertime wave variance maximises just above the zero-wind line in both components. In contrast the wintertime wave is generally smaller than 60 m^2s^{-2} at most heights.

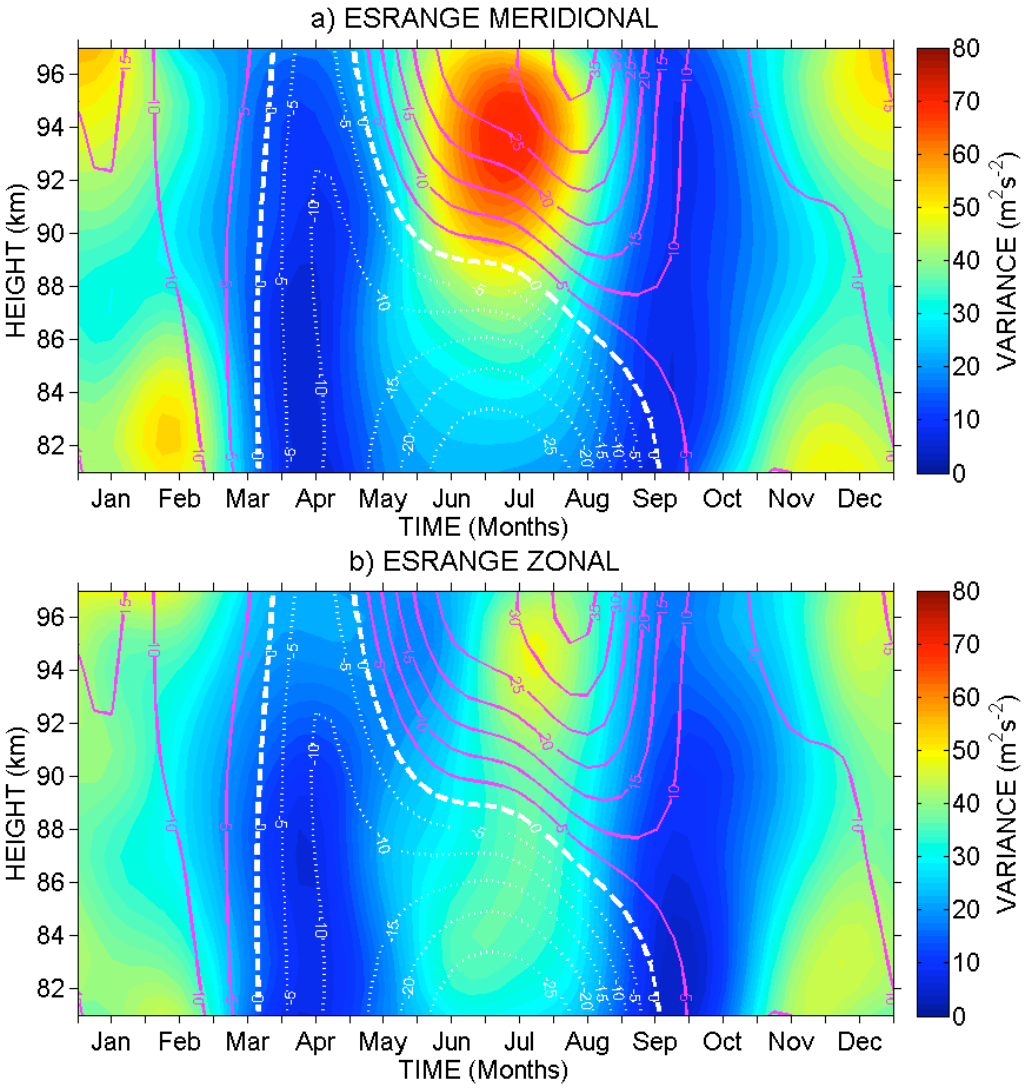

Figure 5.9: A composite-year analysis of the Esrange (Arctic) variance data from Fig. 5.8 for a) the meridional component and b) the zonal component (filled colour contours). Also plotted are monthly mean zonal winds (open contours). The zero-wind contour is indicated by the heavy dashed white line.

Figure 5.9 presents a similar composite-year analysis for the data from Esrange. As in Fig. 5.8, contours of mean zonal winds are plotted on the figure as lines. The results from Esrange are generally similar to those from Rothera. Again the summertime wave has a larger maximum variance than the wintertime wave and maximises just above the zero-wind line. The summertime wave reaches a maximum of $\sim$ 60 m^2s^{-2} at a height of $\sim$ 93 km in the meridional component. The zonal component is rather weaker, with a maximum of $\sim$ 50 m^2s^{-2}. The wintertime wave has a variance at most heights of about 40 m^2s^{-2}, with a minimum at about 88 - 90 km in both zonal and meridional components.

5.3.3 Antarctic / Arctic Comparisons

We will now compare and contrast the climatology of summertime and wintertime 2-day waves in the Antarctic and Arctic.

Firstly, we will consider the summertime 2-day wave. From Figs. 5.8 and 5.9, it can be seen that there are a number of key similarities and differences between the 2-day wave of the two polar regions. These are:

1. The maximum variance of the wave is larger in the Antarctic than the Arctic. This is true in both the zonal and meridional components. For example, in the Antarctic the summertime wave monthly variance reaches values larger than 160 m^2s^{-2}, whereas in the Arctic the equivalent value is only about 60 m^2s^{-2}.

2. The relative magnitude of the zonal and meridional components is different between the two hemispheres. In the Antarctic, the zonal component is larger than the meridional and the ratio of peak variance, zonal/meridional, is about 1.3 at a height of about 93 km in January. In contrast, in the Arctic the meridional component is larger than the zonal and the ratio of peak variance, zonal/meridional, is about 0.7 at a height of about 93 km in July.

3. In both hemispheres the summertime wave maximises at a height of about 93 km. This is in the region of strongly sheared zonal flow associated with the summertime middle atmosphere zonal jet. The waves reach largest amplitudes above the zero-wind line, but are still detectable to the lowest heights observed.

4. The duration of occurrence of the 2-day wave appears to be shorter in the Antarctic than in the Arctic. In the Antarctic, strong wave activity lasts only a little longer than one month (January), but in the Arctic strong wave activity is evident for at least three months (June - August). This appears to be connected to the duration of the strongly-sheared zonal flow occurring above the zero-wind line. In the Antarctic, such strong shear above the zero-wind line, with the zero-wind line at a height of about 90 km or below, only occurs in January. So although there is strong zonal wind shear in December, the zero-wind line occurs at heights above 95 km and there is no evidence of the wave having significant activity. In contrast, in the Arctic, strong zonal wind shears exist above the zero-wind line with the zero-wind line being below about 90 km throughout June - August. The wave is observed throughout this longer interval. However, because only three summer seasons of Antarctic observations are available these conclusions must be treated with some caution.

To investigate the duration of occurrence of the 2-day wave in more detail, Fig. 5.10a, b

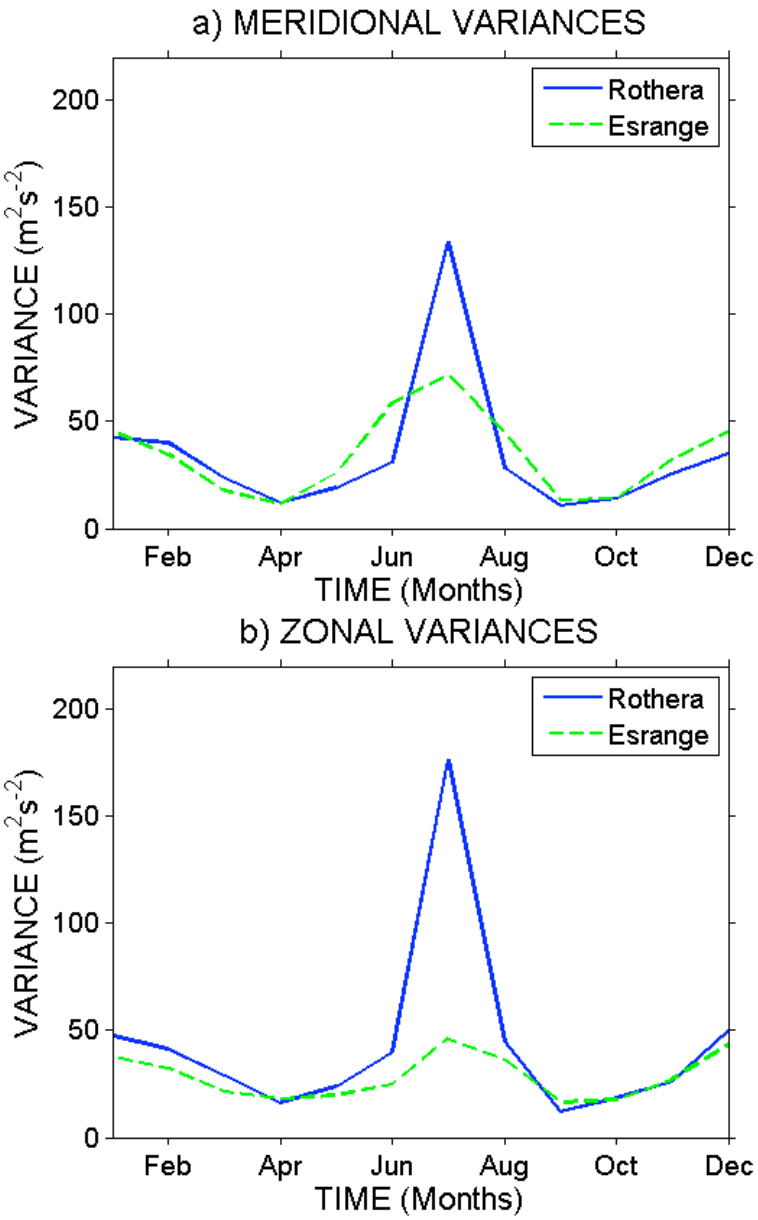

Figure 5.10: A composite year analysis of variances at a height of 93 km, corresponding to the data shown in Figs.5.8 and 5.9 for a) the meridional component and b) the zonal component. Months are for Esrange, Rothera data shifted by 6 months to make seasons comparable.

presents composite variances at a height of $\sim$ 93 km. The variances calculated over Rothera were shifted by 6 months in order to make the seasons comparable, so the months used on the time axis are those at Esrange. Figure 5.10a presents the meridional mean monthly variances measured over Rothera and Esrange. Figure 5.10b presents a similar analysis for the zonal component. It can be seen from the figures that the summertime wave activity over the Antarctic is significantly more intense in both components. However, in the meridional component the Antarctic wave activity appears to be shorter lived than that in the Arctic, although this may be influenced by the strong 2005/2006 summertime event since this is a mean taken from 3 years.

Secondly, we will consider the wintertime 2-day wave. From Figs. 5.8 and 5.9, it can be seen that there are again a number of key similarities and differences between the wintertime 2-day wave of the two polar regions. These are:

1. The variances appear to be very similar in both the Antarctic and Arctic. The mean variances in both hemispheres reach maximum values between $\sim$ 50- 60 m^2s^{-2} .

2. In both hemispheres the ratio of zonal to meridional variances is approximately one.

3. The wave is evident across the height range observed, but in both hemispheres has a minimum at heights between $\sim$ 88 - 90 km with maxima above and below this height.

4. In both hemispheres the duration of the wave appears to be very similar. The wave reaches largest variances (say, above 20 m^2s^{-2}) in May - August over Rothera and November - February over Esrange.

To investigate further the differences in the 2-day wave between the Antarctic and Arctic, a ratio of the composite years of Figs. 5.8 and 5.9 was calculated. The composite monthly mean variances calculated over Rothera were shifted by 6 months in order to make the seasons comparable. Figure 5.11 presents time-height contours of these ratios. In the figure, the months used on the time axis correspond to the month at Esrange. Figure 5.11a presents the composite monthly mean variances for the meridional component of the 2-day wave over Rothera divided by the equivalent variance from Esrange. Figure 5.11b presents a similar analysis for the zonal component. Differences of the composite years of Figs. 5.8 and 5.9 were also calculated for both zonal and meridional components and are shown in Figure 5.12. The figure shows that the differences calculated confirm the results in Fig. 5.11.

The data presented in the figure show considerable inter-hemispheric differences between Rothera and Esrange. The summertime 2-day wave (June - August) is stronger over Rothera, in both the zonal and meridional components. The ratio reaches a maximum of just over 4 in the zonal component at heights of $\sim$ 90 - 94 km, corresponding to larger wave amplitudes in the Antarctic. In contrast, in the meridional component, although the variances are larger

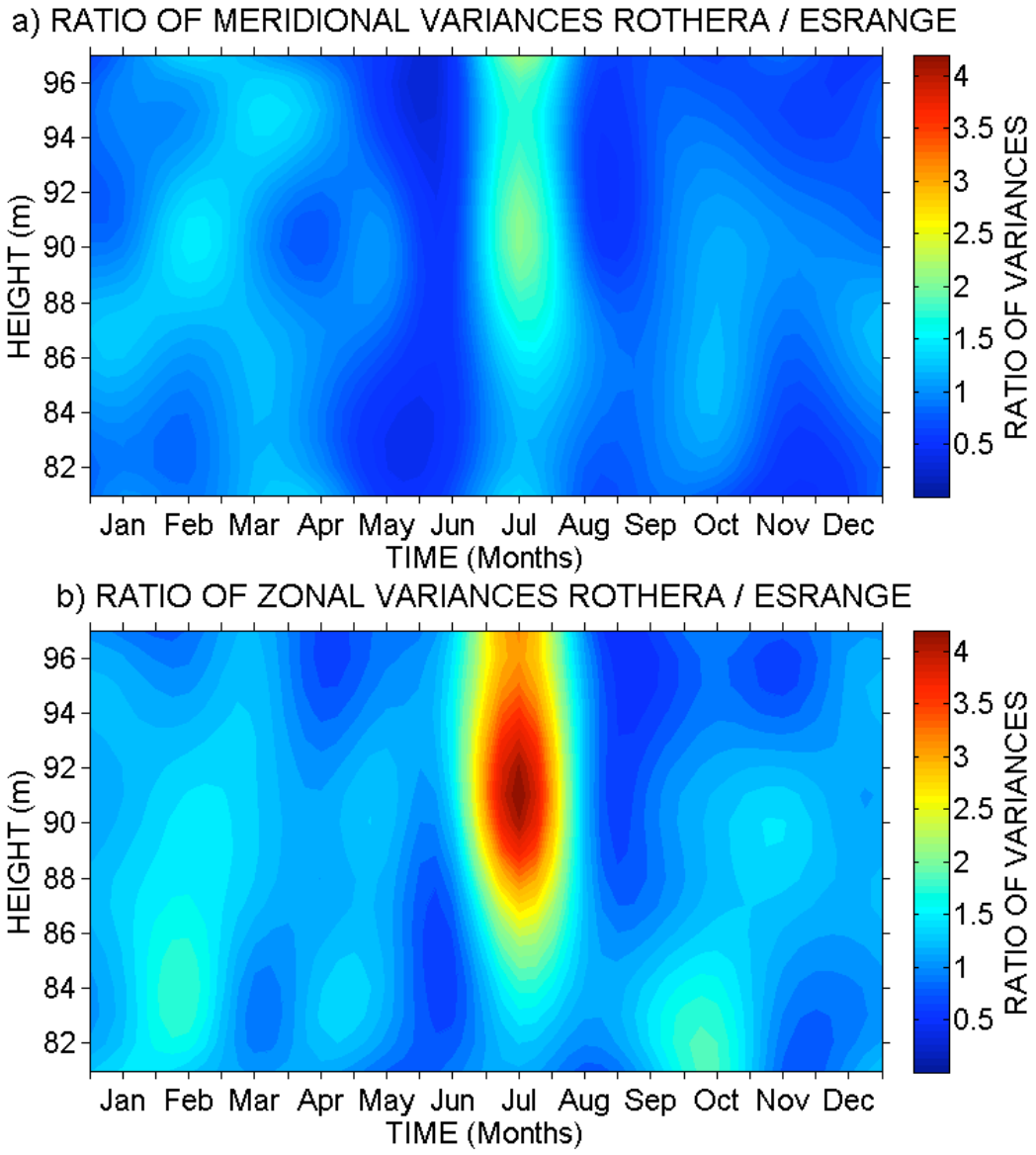

Figure 5.11: A ratio of the composite year analyses from Figs. 8 and 9 for a) the meridional component and b) the zonal component. In each case the ratio is the variance at Rothera divided by the variance at Esrange. The months are for Esrange, Rothera data shifted by 6 months to make seasons comparable.

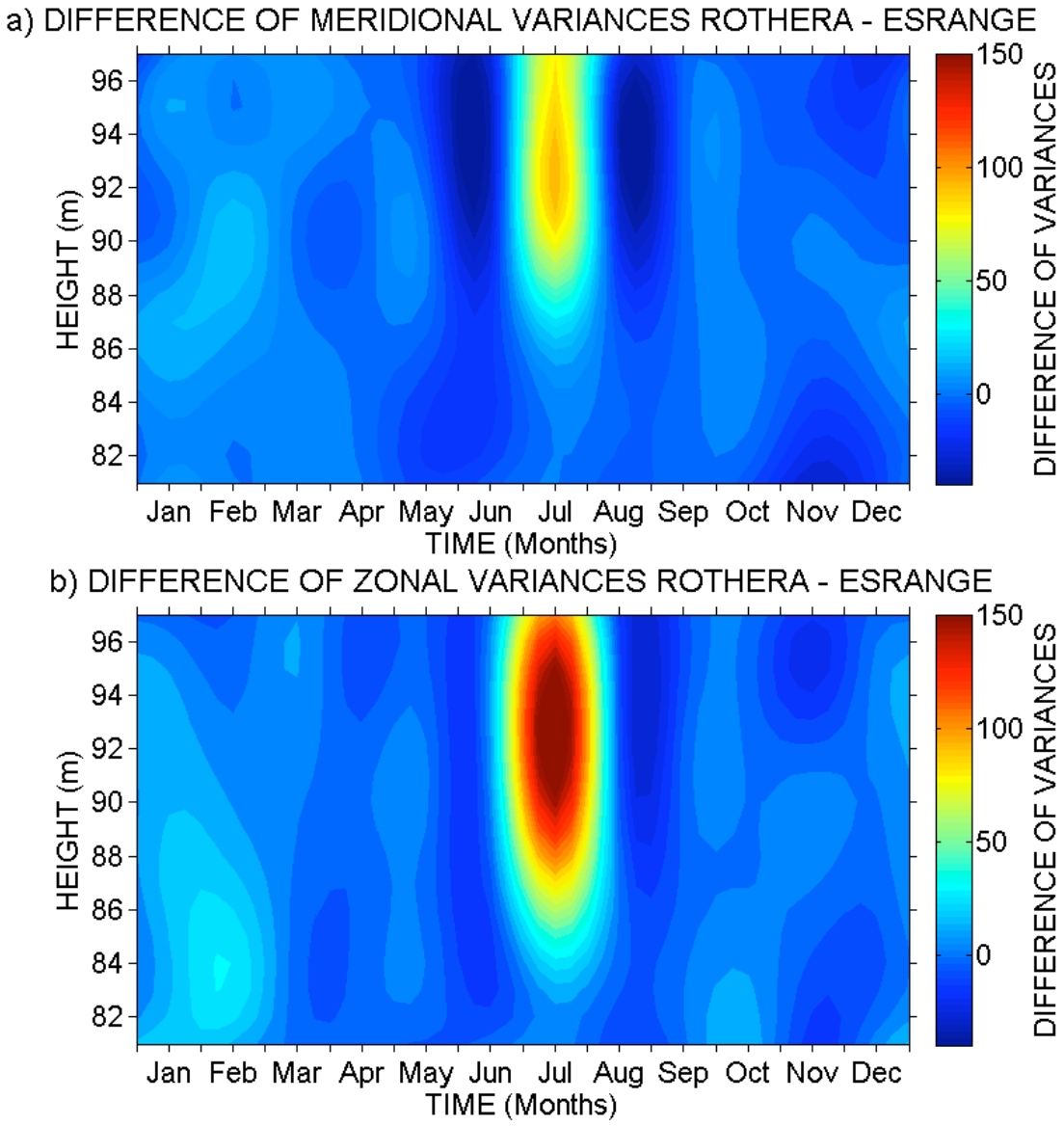

Figure 5.12: A difference of the composite year analyses from Figs. 8 and 9 for a) the meridional component and b) the zonal component. In each case the difference is the variance at Esrange subtracted from the variance at Rothera. The months are for Esrange, Rothera data shifted by 6 months to make seasons comparable.

over Rothera the ratio is only about 2.5. If we consider the wintertime 2-day wave, there is no clear tendency for larger variances over either polar region.

5.4 Discussion

Nozawa et al. (2003b) suggested that in the mesosphere and lower thermosphere the summertime 2-day wave and the wintertime 2-day wave are actually separate phenomena, the first being the familiar W2, W3, W4 propagating planetary waves and the latter being an E2 wave. Palo et al. (2007b), Baumgaertner et al. (2008) and Sandford et al. (2008) used satellite observations to confirm this suggestion. Palo et al. (2007b) suggested that E2 waves of this type are generated by non-linear interactions between the summertime 2-day wave and the migrating diurnal tide. Sandford et al. (2008) suggested that the wintertime E2 wave observed in the MLT is the mesospheric manifestation of a stratospheric wave proposed by Prata (1984) to originate on the poleward flank of the winter polar stratospheric vortex. Here we will discuss the summertime and wintertime waves in turn.

Firstly, we will consider the summertime 2-day wave. A number of observers have investigated the 2-day wave at mid-latitudes in the northern and southern hemispheres. The wave periods we observe are generally in agreement with those reported in other high latitude studies (e.g., Nozawa et al., 2003a; Baumgaertner et al., 2008). These studies have revealed a general pattern in which the largest amplitudes occur in the southern hemisphere (e.g., Craig et al., 1980; Rodgers and Prata, 1981; Craig et al., 1983; Limpasuvan and Wu, 2003). Our observations suggest that the larger southern hemisphere amplitudes persist to high latitudes and are clearly observed in the polar regions. This inter-hemispheric difference in amplitude is probably due to the different wavenumber components comprising the 2-day wave in the two hemispheres. In particular, the southern hemisphere is known to be dominated by a W3 component, whereas the northern hemisphere is known to have significant additional contributions from the W2 and W4 components (e.g., Meek et al., 1996; Norton and Thuburn, 1996; Lieberman, 1999; Limpasuvan and Wu, 2003; Pancheva et al., 2004).

Our observations also suggest that the average duration of 2-day wave activity is shorter in the Antarctic than the Arctic, although the Antarctic wave can reach larger amplitudes. An explanation for this behaviour might be as follows. The major W3 component of the 2-day wave is believed to have the character of the Rossby (3, 0) normal mode, but can be excited by instabilities associated with the summertime mesospheric westward jet (e.g., Fritts et al., 1999; Lieberman, 1999; Salby and Callaghan, 2001; Rojas and Norton, 2007). We thus might expect to find strongest wave activity at times when there is strong shear in the summertime mesospheric jet.

However, the wave propagation is constrained by wave/mean-flow interactions as outlined by

the Charney-Drazin theorem. Thus it can only propagate within a particular range of zonal wind speeds. The Charney-Drazin theorem can be approximated as allowing propagation only for zonal mean wind speeds, $0 < \overline{u} - c_x < U_c$, where $\overline{u}$ is the zonal mean wind, c_x is the zonal phase speed of the planetary wave which is $\sim$ - 28 ms^{-1} for a 2-day W3 wave at a latitude of 68°, where the minus sign indicates westward propagation and U_c is the Rossby critical velocity (Charney and Drazin, 1961). This means that the wave should only be able to propagate in westward zonal wind speeds above - 28 ms^{-1} (i.e. the wave cannot propagate through the strongly westward flow of the summertime middle-atmosphere jet). Similarly, a 2-day W4 wave at these latitudes should only be able to propagate in zonal winds above - 21 ms^{-1} .

This application of the Charney-Drazin theorem is subject to two qualifications. The first is that the simple theory quoted above is an approximation. Thus as noted by Luo et al. (2002), in the real atmosphere, weak wave activity may be observed outside of the regions defined by the theorem. The second qualification is that our results are presented as monthly mean winds and monthly variances. This means that in months where the average wind speed is outside the range specified by the theorem, there may still be episodes within that month where the wind speed does for a time fall within the range specified and so allowed the wave to propagate.

Because the zero-wind line is higher in the early months of the summer in the Antarctic, compared to the Arctic (at least in the years observed), the zonal winds are not strongly eastwards enough in the height range observed to allow the wave to propagate in the Antarctic during these early summer months. For example, over Rothera in November and December the zonal winds are almost entirely westward, whereas in the corresponding months in the Arctic (May and June) the winds become increasingly eastward above about 90 km (see Figs. 5.8 and 5.9). The summertime 2-day wave is thus largely absent in early Antarctic summer, but is present in early Arctic summer, leading to a reduced overall duration of occurrence in the Antarctic.

Secondly, we will consider the wintertime 2-day wave. In contrast to the summertime situation, the wintertime wave appears to have relatively small inter-hemispheric differences. In both the Antarctic and Arctic the seasonal climatology appears to be similar and the ratio of zonal to meridional variances is on average close to 1. The wave is present throughout the height range observed in both hemispheres and has a smaller maximum variance (i.e., smaller amplitude) than the summertime wave in the climatological average.

In both hemispheres, the wintertime wave variance has a minimum at a height of $\sim$ 88 - 90 km. This behaviour was also reported by Nozawa et al. (2005), where it was suggested that the secondary maxima in the wintertime 2-day wave amplitudes may be due to non-linear coupling process between the 2-day wave and other waves/tides for example, the 24 and 12 hour tides.

The wave was present in all the winters observed in both hemispheres and so seems to be a persistent feature of the wintertime polar mesosphere and lower thermosphere. Satellite observations have revealed this to be an E2 wave possibly originating in the lower polar stratosphere (Baumgaertner et al., 2008; Sandford et al., 2008) or generating by non-linear interactions (Palo et al., 2007b). Our observations show that despite the well known differences between the Antarctic and Arctic lower stratosphere, at MLT heights there is surprisingly little inter-hemispheric difference in the character of the wintertime 2-day wave.

The seasonal behaviour of this wintertime wave suggests it interacts with the mean winds. For an E2 2-day wave at 68 ° latitude, the zonal phase speed will be about + 43.6 ms^{-1} . The wave will thus only be able to propagate in regions where the zonal wind speed is greater than this value. However, in our observations, significant wave activity is evident at times when the monthly-mean wind is smaller than this value. For instance, significant wave activity is observed during winter with monthly-mean zonal winds as small as + 20 ms^{-1} . However, unlike the case with the summertime wave, this wintertime wave will have been able to propagate through the strongly eastward winds of the middle-atmosphere jet to the heights where it is observed.

5.5 Conclusions

In this chapter we have presented climatologies of the 2-day wave at Antarctic and Arctic latitudes. These were constructed from data recorded using identical meteor radars situated at the conjugate geographical latitudes of Rothera, (68°S, 68°W) and Esrange (68°N, 21°E). Inter-hemispheric comparisons can therefore be made free from the biases that might affect measurements if made by different techniques, such as comparisons between meteor and MF radars. This allows a robust assessment of inter-hemispheric differences between the two polar regions. The observations reveal two distinctly different waves in summer and winter in both hemispheres. We suggest that the summertime wave is the polar manifestation of the classic mid-latitude W3 and W4 2-day wave. We suggest that the wintertime wave is the polar E2 wave reported in the satellite observations described in Sect. 5.1.

In summer, the 2-day wave was observed in each year. A considerable degree of inter-annual variability was observed in both hemispheres. The climatological mean reveals that the wave amplitude is, on average, larger in the Antarctic than the Arctic. In the Antarctic the zonal component of the wave is larger than the meridional (at least in the three years observed). This is in contrast to the Arctic where the meridional component dominates. However, the duration of strong wave activity in the Antarctic is usually shorter than in the Arctic. This shorter Antarctic duration may be due to the shorter interval of time during which a strong shear exists in the eastward zonal flow above the zero-wind line. The different durations of occurrence of the 2-day wave would thus be a consequence of the differences in

the background flow of the two polar regions.

The wintertime 2-day wave is also a persistent feature of the polar MLT. It occurs each year. The variance (and thus amplitude) of the wintertime wave is generally smaller than the summertime wave in both the Antarctic and Arctic. The meridional and zonal components have approximately equal variances. There is clear inter-annual variation in the monthly wave variance but little variation in the months during which the wave occurs. Our observations show that the observed characteristics of the 2-day MLT wintertime wave are very similar in both hemispheres. From this we conclude that it is the same type of wave being observed in the Antarctic and Arctic (the E2 described above). This similarity in behaviour of the Antarctic and Arctic wintertime wave occurs despite the significant inter-hemispheric differences known to exist in the lower stratosphere.

Chapter 6

Zonal wavenumbers of the summertime 2-day planetary wave complex observed in the mesosphere by Aura MLS

6.1 Introduction

Recent observations and theoretical work suggest that the 2-day planetary wave in the summertime mesosphere is composed of multiple superposed zonal wavenumbers. Here we use EOS Aura MLS temperature data to determine the component zonal wavenumbers of the 2-day wave in the mesosphere at latitudes of 70°S to 70°N from 2004 - 2009. We consider the effect of aliasing between different wavenumbers and note that significant aliasing can occur and result in spurious signals, particularly at high latitudes in winter. The seasonal evolution of the different wavenumbers is investigated and found to be very different between the Northern and Southern Hemispheres. In both hemispheres the wave is dominated by westward-travelling waves of zonal wavenumber 3 and 4 (W3 and W4). However, in the Southern Hemisphere the wave is dominated by the W3 component but in the Northern Hemisphere the W3 component is smaller and the W4 component is often of similar or larger amplitude. A small-amplitude westward-travelling zonal wavenumber 2 (W2) wave is also evident in both hemispheres. In the Northern Hemisphere, the W2 amplitudes never exceed 3 K, the W3 amplitudes can reach 3.5 K and the W4 can be the largest component reaching amplitudes of 4 K. In the Southern Hemisphere, the W2 amplitudes can reach up to 3.5 K, the W3 amplitudes can be much larger, reaching 12 K, and the W4 amplitudes are smaller than in the Northern Hemisphere, in 4 out of 5 years not exceeding 3 K. The Northern Hemisphere W4 can reach large amplitudes in August when the W3 is small which means that the late-summer Northern Hemisphere quasi-2-day wave is usually a W4 oscillation rather than the familiar W3. In contrast, in the Southern Hemisphere, the W3 is often larger than the W4 around the summer solstice and there are no episodes observed where the wave becomes dominated by the W4 for an extended period of time. A high

degree of inter-annual variability is evident, particularly in the Southern Hemisphere, where the W3 peak amplitudes vary from 12 K in January 2006 to 3 K in January 2009. The height-latitude structure of the W4 suggests that this wave is a (4, 0) Rossby-gravity wave. This work has been published as; Tunbridge, V.M., D.J. Sandford, and N.J. Mitchell (2011), Zonal wavenumbers of the summertime 2-day planetary wave observed in the mesosphere by EOS Aura MLS. *Journal of Geophysical Research-Atmospheres*, doi:10.1029/2010JD4567.

6.2 Data Analysis

The source of data used in this study is the Microwave Limb Sounder (MLS) instrument aboard the NASA Earth Observing System (EOS) Aura satellite, which is part of the A-train constellation of satellites. MLS uses microwave emissions in the range 118 GHz to 2.5 THz to measure temperature and composition in the lower and middle atmosphere. The Aura satellite is in a Sun-synchronous orbit and so it passes through two local times at any given latitude. The range of latitude accessible to the satellite is approximately 82°N to 82°S. Measurements are performed along the sub-orbital track. The spatial resolution is approximately 500 km horizontally and 3 km vertically, decreasing to about 10 km near the mesopause (Livesey et al., 2007). A more detailed description of EOS Aura MLS can be found in (e.g., Waters et al., 2006). Here we use the temperature from the level-2 version 2.2 data product over the height range $\sim$ 10 - 97 km. The data were screened as recommended by the data quality document of Livesey et al. (2006). This means that the data products were only used if the precision was positive, the quality was greater than 0.6 and convergence is less than 1.2 and the status was even. The temperature precision is 1 K or better from 316 hPa to 3.16 hPa, degrading to $\sim$ 3 K at 0.001 hPa. The vertical resolution is 3 km at 31.6 hPa and 6 km at 316 hPa and only $\sim$ 13 km at 0.001 hPa Schwartz et al. (2008). The data are considered from the interval September 2004 - December 2009.

In order to extract the 2-day wave signal from the temperature data, the least-squares fitting method of Wu et al. (1995) was used. This method has earlier been used to identify the 2-day wave in UARS measurements. The method has subsequently been successfully applied to EOS Aura MLS temperature and geopotential height measurements (e.g., Limpasuvan et al., 2005; Baumgaertner et al., 2008; Sandford et al., 2008; Limpasuvan and Wu, 2009; Offermann et al., 2011). The method has the advantage that it can be used with non-uniform or irregular sampling pattern, but is more computationally intensive than alternative approaches such as FFT or asynoptic transforms. The advantages and disadvantages of the method have been discussed in depth by Wu et al. (1995).

In our application of the method here, sinusoidal functions with periods incremented in 1-hour steps between 40 - 60 hours period were least-squares fitted to the satellite data in a 12-day window on each pressure level in the data set. On each pressure level the data

were sorted into bands of 10 degrees latitude from 80°N to 80°S. The data points used in the fitting thus consisted of those parts of the track profiles that fall within a particular 10 degree latitude band and within a particular 12-day time window on a particular pressure level. This window was then incremented through the time series in steps of 3 days. The sinusoidal wave functions fitted had zonal wavenumbers 4 to -4, where positive wavenumbers correspond to westward propagating waves and negative to eastward propagating waves. For each wavenumber the wave period at which maximum amplitude occurred was recorded and taken to be the period of the 2-day wave in that particular 12-day window. The analysis was carried out for latitudes between 82°N to 82°S and for heights between $\sim$ 10 - 97 km. The pressure levels are converted to height in the figure labels for easy comparison with radar observations.

This analysis yields a final data product which is time series of temperature amplitudes, phases and periods for wavenumbers 4 to -4, within a particular latitude band. Before these results can be interpreted, however, we need to consider the affects of standard errors in the best fitting process and the possibility of aliasing between different wavenumbers.

Firstly, we will consider the standard error in the amplitude of the wave measured by the least-squares fit. In addition to the amplitude of a particular wave fitted to the data, the least-squares analysis also yields the standard error of that fitted amplitude. Considering the whole dataset, these standard errors in amplitude are found to be generally between about $\pm$ 0.3 and $\pm$ 1.2 K and mostly towards the lower end of this range. As an example, Figure 6.1 presents contours of the standard error for the case of the W3 wave as a function of time and latitude at a height of 91 km. These results are presented as being typical of the standard errors yielded by this analysis. The standard errors in the case of Figure 6.1 are not constant, but vary from less than $\pm$ 0.2 K up to about $\pm$ 0.6 K. We examined the standard errors for other heights and latitudes and for other wavenumbers and found the maximum standard errors in amplitude never exceeded $\pm$ 1.4 K and were almost always $\pm$ 0.5 K or less. We therefore will use $\pm$ 1 K as a representative minimum amplitude a wave must have to be regarded as significant, taking 2 times the standard error as a threshold for significance. This is a slightly pessimistic threshold, but does allow us to use a simple standard cut off in the presentation of our results.

Secondly, we will consider the effects of aliasing. The nature of the sampling offered by satellite measurements can lead to significant aliasing between different zonal wavenumber and period combinations. This could give rise to spurious results in which significant amplitudes are calculated for a particular wavenumber and frequency where no wave is actually present in the atmosphere with that wavenumber and frequency, and the amplitude has actually been aliased from another wave altogether.

This problem has been considered in depth by Salby (1982a), Salby (1982b), Wu et al. (1995) and Meek and Manson (2009) who also considered aliasing in the specific case of 2-day waves.

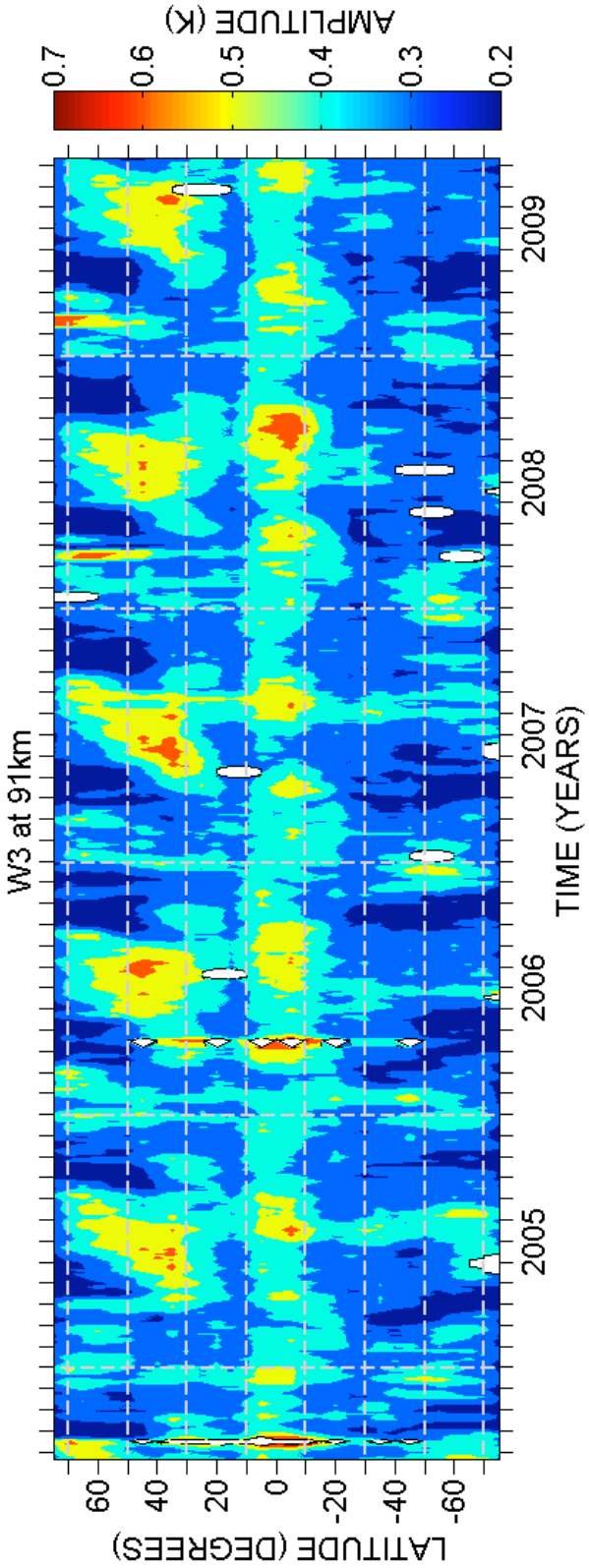

Figure 6.1: The temperature amplitude uncertainties of the W3 2-day planetary wave. The results are shown for a height of 91 km in the mesosphere as a function of latitude and time.

In the analysis presented here, we are aware that aliasing between different wavenumbers could be a significant issue. In particular, we need to be able to distinguish between real waves in the atmosphere and spurious results caused by the aliasing of amplitude from other wavenumbers.

We have examined the possible impact of aliasing on our results by modelling as follows. For each wavenumber -16 to 16, a synthetic data set was created in which a wave of arbitrary amplitude was present at that particular wavenumber with a wave period of 48 hours and of constant amplitude from pole to pole. This data set was then sampled using the same spatial and temporal sampling as that of the EOS Aura MLS data and the results examined to see how much amplitude was present in other wavenumbers and frequencies as a result of aliasing from this particular wave.

Figure 6.2 presents the results of this analysis for wavenumbers -7 to 7 (the higher wavenumbers not plotted because they are unlikely to correspond to real features in the atmosphere). Figure 6.2a presents the example case of a W3 wave of frequency 0.5 cycles per day (cpd) at a latitude of 70°S and a height of 59 km. In addition to a spectral peak corresponding to the synthetic wave, a number of other peaks are evident. In particular at wavenumber W3 there are a series of small "side-lobe" peaks at frequencies slightly higher and lower than 0.5 cpd. There are also three smaller peaks at frequency, wavenumber coordinates of 0.5, -2; 1.5, -1 and 1.5, 4 (where wavenumber -1 is an E1 wave etc). Note that such aliasing can also occur from a genuine wave at these latter periods and wavenumbers resulting in a spurious aliased signal at the 0.5, 3 frequency/wavenumber coordinate. However, some of the signals aliased from W3 are unlikely to be mistaken for a genuine planetary wave because they occur at frequencies higher than expected for a planetary wave (e.g., the two signals at 1.5 cpd). This result shows that a significant fraction of the amplitude of a W3 2-day wave can be aliased into an E2 2-day wave (and visa-versa). Finally, note that there are also signals aliased to wavenumber frequency coordinates outside of the regions plotted in Figure 6.2a. For example the 0.5 cpd W3 wave also produces an aliased signal at a wavenumber and frequency of 1, -11 . However, these peaks are at such extreme wavenumbers that we will not consider them further.

A similar analysis is presented for aliasing from a 0.5 cpd W2 and W4 waves in Figures 6.2b and 6.2c respectively. Both Figures also reveal a pattern of aliased peaks. Again there are three peaks in each case one at 0.5 cpd and two at 1.5 cpd. Figure 6.2c shows an aliased signature at frequency, wavenumber coordinates of 0.5, -1 wave and Figure 2d shows an aliased signature at frequency, wavenumber coordinates of 0.5, -3. There are again two signals for each wavenumber at a frequency of 1.5 cpd.

We noticed that there is considerable variation in the population of aliased waves as a function of latitude. To investigate this further we calculated the fraction of a synthetic waves amplitude that would be aliased into other wavenumbers as a function of latitude.

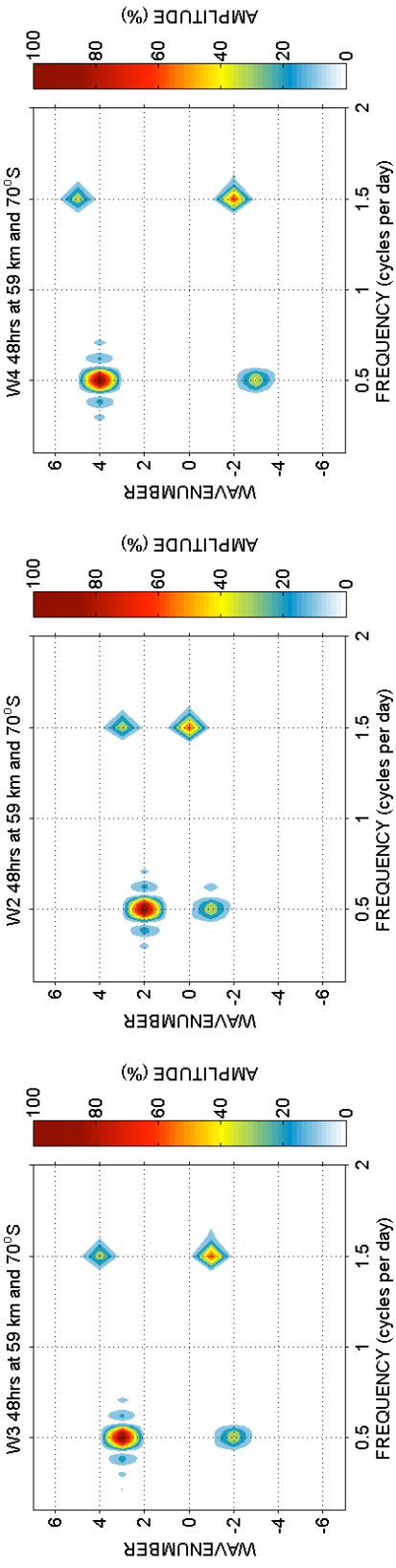

Figure 6.2: Aliased signals from a primary 2-day planetary wave at 0.5 cpd. This is for a) a W3 primary wave, b) a W2 primary wave and c) a W4 primary wave. Negative wavenumbers refer to the eastward travelling waves and positive to westward travelling waves.

The results of this investigation are summarised in Figure 6.3.

Firstly, we will consider the impact on our results of an E2 wave present in the atmosphere. Such waves with periods near 2-days are known to exist in the atmosphere (e.g., Nozawa et al., 2003a; Palo et al., 2007b; Sandford et al., 2008). Figure 6.3a presents the case where a synthetic E2 wave of constant arbitrary amplitude is modelled as present in the atmosphere. The Figure indicates the fraction (as a percentage) of the amplitude of this wave which will be aliased into W2, W3, and W4. From the Figure it can be seen that there is no significant aliased signal for the W2 and W4 components. However, a W3 aliased signal does result. This aliased signal varies strongly with latitude due to the nature of the sampling. The aliased W3 amplitude exceeds 40% of the E2 amplitude poleward of about 65° and decreases to very small values near the equator. This means that at high latitudes an E2 wave may produce significant amplitude aliased into the W3 wave. It is known that 2-day E2 waves exist in the high-latitude wintertime stratosphere and mesosphere (e.g., Nozawa et al., 2003b; Sandford et al., 2008).

Consequently, any 2-day W3 signal observed at high latitude in wintertime must be treated with caution because it may be aliased from the E2 rather than being a genuine wave in the atmosphere. However, in summer it is not believed that there exists a large amplitude E2 2-day wave at high latitude so any W3 signal observed in summer will thus be genuine. We note that our conclusion that amplitudes of up to about 40% may be aliased from a 2-day E2 to a W3 is in good agreement with the value derived by Wu et al. (1995) in their consideration of aliasing.

Secondly a similar technique was applied to the E1 and E3 waves and the results are shown in Figures 6.3b and 6.3c respectively. In Fig. 6.3b a synthetic E1 wave of constant arbitrary amplitude is modelled as present at all latitudes. The figure shows that the E1 wave produces an aliased signal in the W2 wave but no significant aliased signals for the W3 and W4 waves. The aliased W2 wave has a similar profile of amplitude with latitude to the results presented in Fig. 6.3a in that it exceeds 40% of the amplitude of the E1 wave poleward of about 65° and decreases to very small relative amplitudes near the equator. Therefore, at high latitudes an E1 wave may produce a W2 wave with a significant aliased amplitude. Similarly in Fig. 6.3c, a synthetic E3 wave is modelled as present at a constant arbitrary amplitude at all latitudes. In this case it can be seen that a significant W4 aliased amplitude can occur at high latitudes.

From the above analysis we conclude that for 2-day waves, high-latitude spurious signals may arise as a result of aliasing. In particular there may be aliasing between zonal wavenumbers E2/W3, E1/W2 and E3/W4. Note that aliasing between other pairs is possible if wave periods other than 2-days are considered. It is known that E1 and E2 waves exist in the atmosphere at high-latitudes in winter and so the possibility of aliasing must be considered in results showing W2 and W3 waves at these latitudes and in this season. However, at

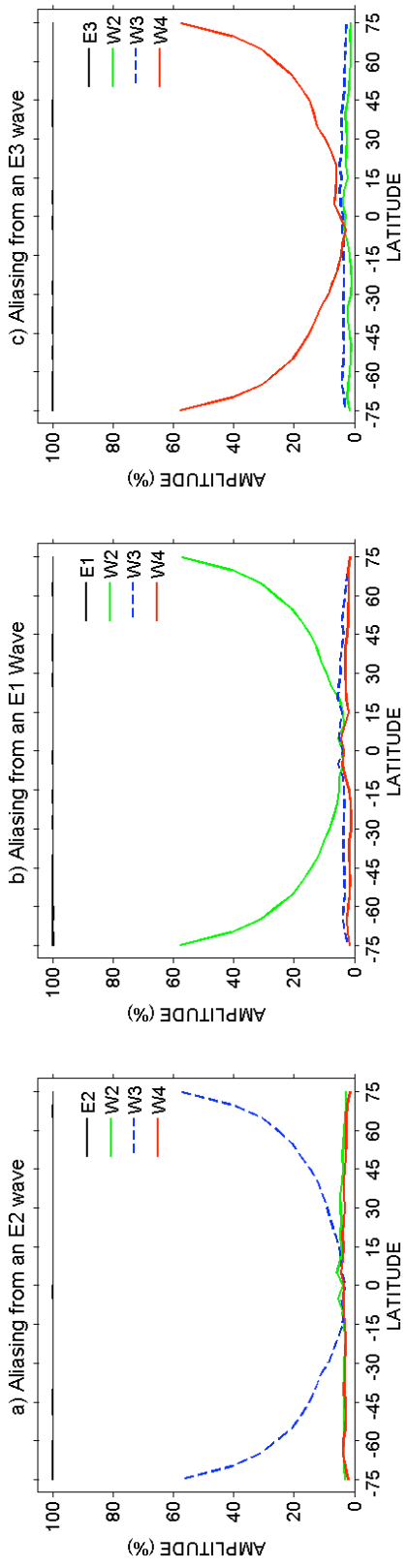

Figure 6.3: The fraction of wave amplitude aliased from a primary 2-day planetary wave into zonal wavenumbers W2, W3 and W4 as a function of latitude for a) an E2 primary wave, b) an E1 primary wave and c) an E3 primary wave. Spacecraft sampling from July 2008 is used in the analysis.

middle and low latitudes the magnitude of the aliased signals is very much smaller and so aliasing is probably not a significant problem. Finally, note that this analysis cannot detect waves of tidal period. So, for example, the W6 diurnal tide proposed by Walterscheid and Vincent (1996) to be generated by interaction of the 2-day wave and diurnal tide cannot be detected.

6.3 Results

Previous results presented in Sect. 2.5 suggest significant wave amplitudes occur for components W2, W3, W4 and E2. The temperature amplitudes of the W2, W3, W4 and E2 components as a function of time, height and latitude were determined as described above and used to investigate the variability of the 2-day wave.

We will now present the results for two particular heights. These are 91 km, taken as a representative height for the mesosphere and lower thermosphere (MLT) region (and because the radar results presented in Sect. 5.3 indicate that the summertime 2-day wave reaches maximum amplitudes at about this height) and 56 km, taken as a representative height for the stratopause.

Firstly, we present in Figure 6.4 the temperature amplitude time series of the 2-day wave for W2, W3, W4 and E2 components at a height of 91 km and for latitudes between 75°N and 75°S (latitudes poleward of this are not plotted because of the aliasing issues discussed in Sect. 6.2). The data span the interval September 2004 - December 2009. Contours are not plotted for amplitudes smaller than the 1 K threshold identified in Sect. 6.2.

We will now consider the variability of these waves in terms of their seasonal and latitudinal behaviour. We will also consider differences between the Northern and Southern Hemispheres. The figure shows there are significant 2-day wave amplitudes in all four wavenumbers and these wave amplitudes vary strongly with season and latitude.

The W2 amplitudes of Figure 6.4a are largest at middle to low latitudes and occur throughout the year as a series of isolated bursts of activity lasting a few tens of days and generally having amplitudes of less than 2.5 K. Significantly larger wave amplitudes occur in January of each year, where wave amplitudes exceed 3 K. This occurs simultaneously in both hemispheres and so the W2 activity is strongest in Southern Hemisphere summer and Northern Hemisphere winter. For example, in January 2006 wave amplitudes exceed 3 K in both hemispheres at latitudes near 20°. A similar burst of increased wave activity is evident in January 2008. In both cases the wave amplitude is largest in the Southern Hemisphere in summer. Strong inter-annual variability is evident. For example, in January 2006 and 2008 wave amplitudes exceed $\sim$ 3 K in both hemispheres in 2006 and in the Southern Hemisphere

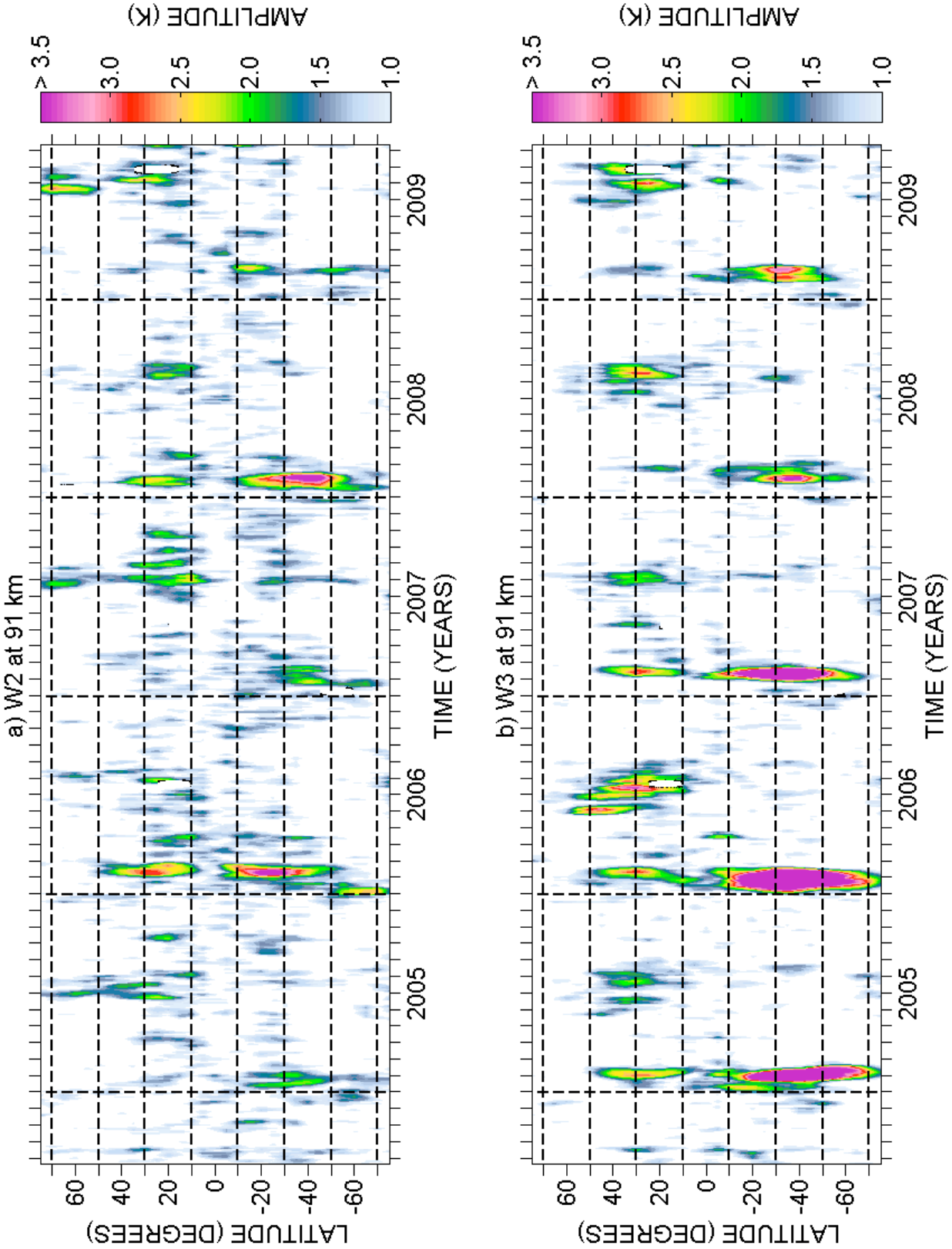

Figure 6.4: The temperature amplitude of 2-day planetary waves at a height of 91 km in the mesosphere as a function of latitude and time. Amplitudes below 1 K are not plotted. The results are shown for a) wavenumber W2 and b) W3.

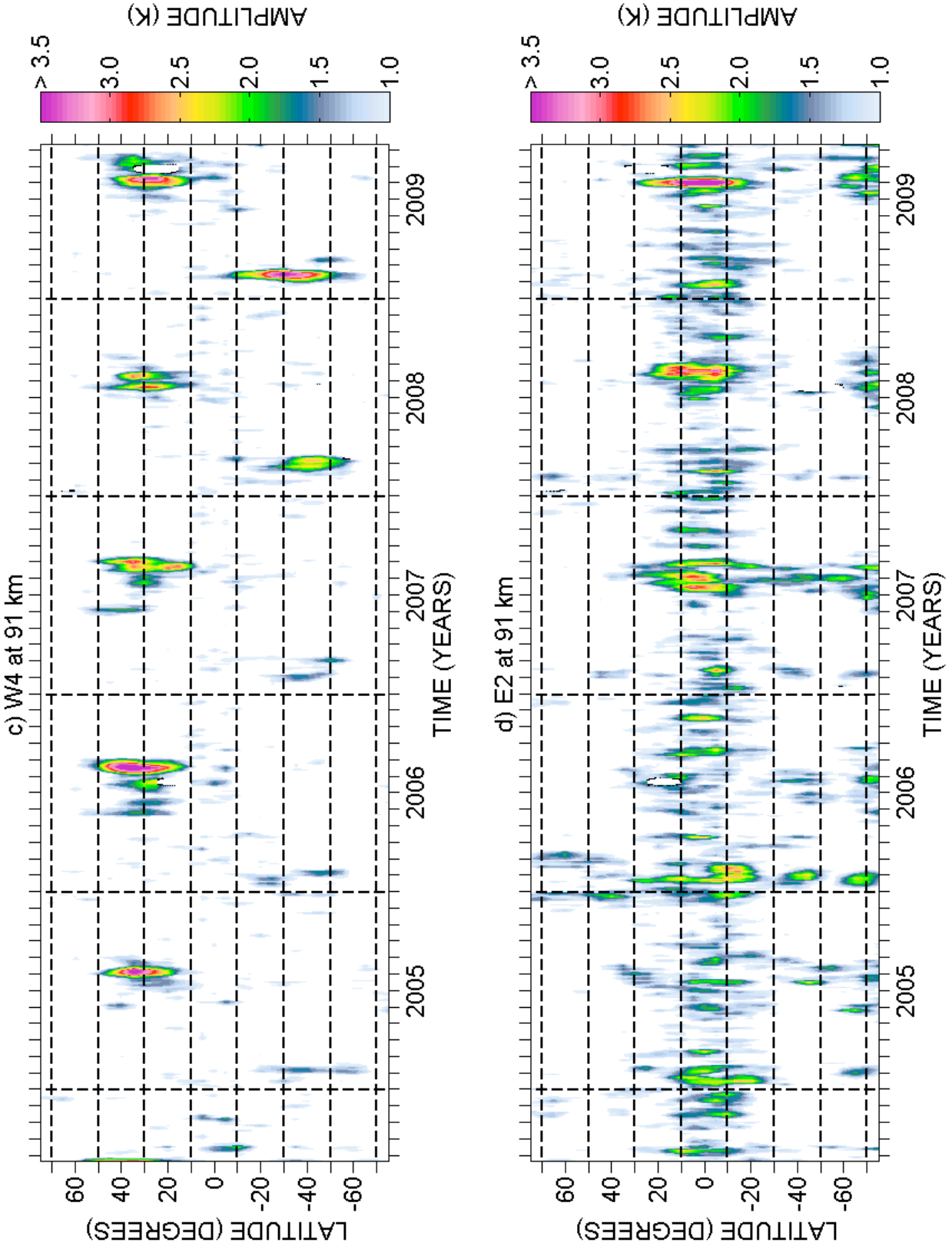

Figure 6.4: The temperature amplitude of 2-day planetary waves at a height of 91 km in the mesosphere as a function of latitude and time. Amplitudes below 1 K are not plotted. The results are shown for c) wavenumber W4 and d) E2.

only in 2008. For the rest of the years wave amplitudes are smaller, reaching only $\sim$ 2 K.

The W3 amplitude of Figure 6.4b include episodes where the wave amplitudes are significantly larger than those of the W2 component. A very clear seasonal behaviour is again evident and there are some significant differences in the wave between the Northern and Southern Hemispheres.

Considering firstly the Southern Hemisphere, it can be seen that the W3 reaches amplitudes in excess of 3 K in January of all years. This summertime wave activity extends from very close to the equator to the highest latitudes observed. The largest amplitudes generally occur at latitudes near 40°S. There is little evidence of significant W3 amplitude at other times of year in this hemisphere. Considerable inter-annual variability is evident. For example, in January 2006 wave amplitudes exceed 3.5 K for latitudes ranging from 25°S - 50°S. The peak amplitude is 12 K. In contrast, in January 2008 amplitudes never rise above 3.5 K and wave activity is confined to a relatively narrow range of latitudes from $\sim$ 20°S - 60°S. Note that the large-amplitude W3 wave event in January 2006 was extensively studied by Limpasuvan and Wu (2009).

In contrast to the Southern Hemisphere, significant W3 wave amplitudes occur in both summer and winter in the Northern Hemisphere. Wave amplitudes are quite variable and sometimes the winter maxima equal the summer ones. Amplitudes are rather less than in the Southern Hemisphere and peak amplitudes are usually only about 3 K. Peak amplitudes occur at latitudes of $\sim$ 30°N - 40°N. It is noticeable that when large W3 amplitudes occur in the Northern Hemisphere winter they occur simultaneously with the strong W3 activity in the Southern Hemisphere summer, suggesting significant inter-hemispheric propagation of the W3 wave under those conditions. Inter-annual variability is again evident. For example wave amplitudes in the summer of 2006 exceed 3 K whereas in summer 2005 they reach only $\sim$ 2.2 K.

The W4 component is presented in Figure 6.4c. Again, a strong seasonal cycle and clear inter-hemispheric differences are evident. In contrast to the W3, the largest amplitudes are observed in the Northern Hemisphere. Again, wave activity occurs in relatively short-lived bursts. These occur most strongly in Northern-Hemisphere summer (July - August) where wave amplitudes reach $\sim$ 3.5 K. Largest amplitudes occur between 30°N and 40°N and wave amplitudes are insignificant polewards of 60° N. The amplitude again varies from year to year. No significant W4 wave activity is evident in Northern-Hemisphere winter.

In the Southern Hemisphere, the W4 also occurs only in summer and is strongest in February of all years observed. W4 wave amplitudes are smaller than in the Northern Hemisphere with peak amplitudes ranging from 1.5 - 2.5 K, except for in 2009 where they reach 3.5 K. Again, strong inter-annual variability can be seen. For example, in February 2009 wave amplitudes reach 3.5 K, whereas in 2008 wave amplitudes are $\sim$ 2.2 K and for the rest of

the years the amplitude is < 1.5 K.

The E2 component is presented in Figure 6.4d. It has largest amplitudes at latitudes between 0° and ± 20°. The largest amplitude bursts occur around the summer and winter solstice. At high latitudes, E2 amplitudes generally maximise in winter. Again, a large degree of inter-annual variability is present. The winter polar E2 wave is also present in the Southern Hemisphere, peaking at amplitudes of over 2 K for each winter in the months of July - August.

We will now consider the results of a similar analysis applied at 56 km. Figure 6.5 presents temperature amplitudes for W2, W3, W4 and E2 in a similar fashion to the results in Figure 6.4, except in this case for a height of 56 km.

The W2 component, shown in Figure 6.5a, maximises at high latitudes in winter in both hemispheres. The wintertime maxima typically have durations of 3 - 4 months. Peak wave amplitudes are ~ 3 K or less. Within each winter season the amplitudes are quite variable with fluctuations in amplitude occurring on time scales as short as a few tens of days. This seasonal and latitudinal variability is quite different from that observed at ~ 91 km (Fig. 4a), where wave amplitudes peak at much lower latitudes. However, we believe this signal is almost certainly the result of aliasing from an E1 wave as described in Sect. 6.2.

The W3 component shown in Figure 6.5b reveals a generally similar seasonal cycle to that evident at 91 km. Again, wave amplitudes are largest in the Southern Hemisphere, where they exceed 3.5 K in three of the five summers observed. In contrast, Northern-Hemisphere W3 amplitudes generally reach only ~ 2 K. The W3 wave occurs in short-lived bursts in summer and maximises at middle latitudes in both hemispheres. The inter-annual variability appears to follow a similar pattern to that evident at 91 km. However, there is a noticeable difference in that significant wave amplitudes appear to occur at high latitudes in winter in both hemispheres. However, we believe that this high-latitude signal is a consequence of aliasing from the high-latitude E2 winter wave (see the discussion on aliasing in Sect. 6.2 and the results of Fig. 6.5d).

The W4 component is shown in Figure 6.5c. As with the W3 component, the seasonal behaviour is quite similar to that observed at 91 km. Again, as at 91 km, wave amplitudes are largest in the Northern Hemisphere. They are largest in short-lived bursts in summer and the amplitudes maximise at mid-latitudes. The pattern of inter-annual variability, however, is slightly different from that observed at 91 km. For instance, the W4 amplitude in Northern-Hemisphere summer of 2006 at 56 km is smaller than the amplitudes observed in either 2005 or 2007, whereas at 91 km the Northern-Hemisphere summer amplitudes in 2006 are the largest observed in any year of the data set.

The E2 component is shown in Figure 6.5d. Unlike the situation at 91 km (Fig. 6.4d) here

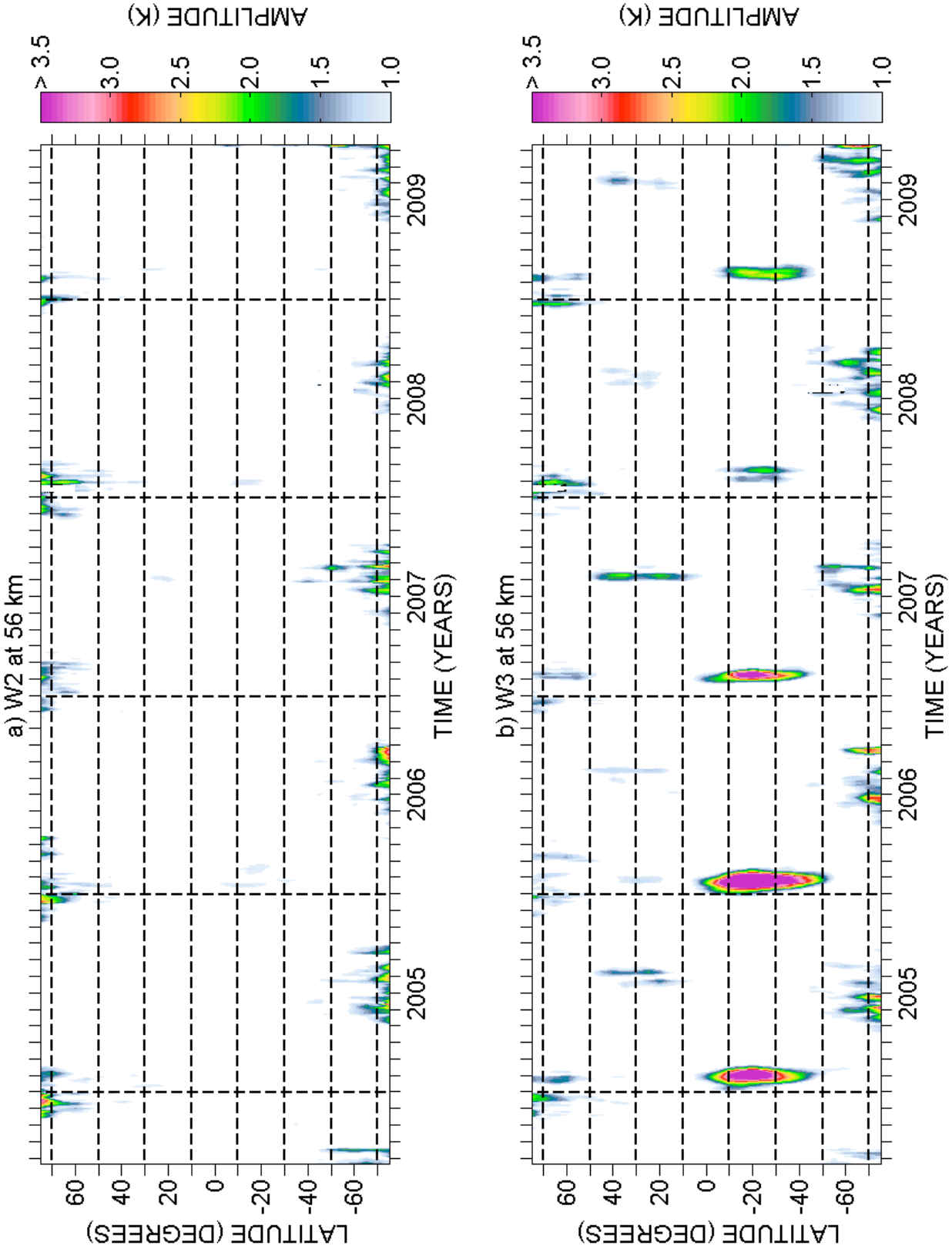

Figure 6.5: The temperature amplitude of 2-day planetary waves at a height of 56 km near the stratopause as a function of latitude and time. Amplitudes below 1 K are not plotted. The results are shown for a) wavenumber W2, and b) W3.

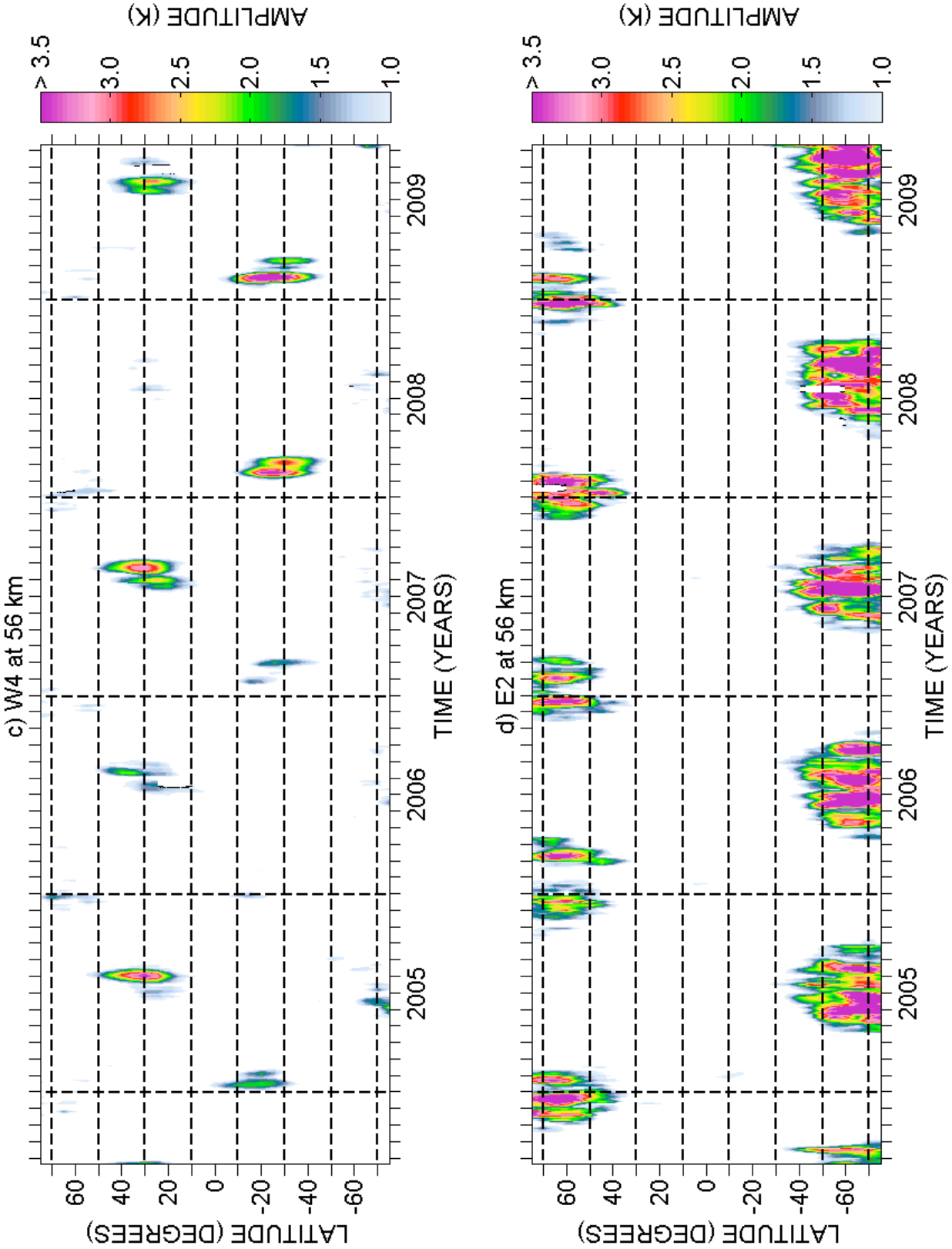

Figure 6.5: The temperature amplitude of 2-day planetary waves at a height of 56 km near the stratopause as a function of latitude and time. Amplitudes below 1 K are not plotted. The results are shown for c) wavenumber W4 and d) E2.

the E2 maximises at high latitudes in winter. It is almost entirely absent at low latitudes and in summer. Significant wave amplitudes occur from December - February in the Northern Hemisphere and May - September in the Southern Hemisphere. The onset and cessation of wave activity is quite abrupt in both hemispheres.

This wintertime, high-latitude E2 wave appears to be the same phenomenon identified by other authors (e.g., Nozawa et al., 2003a; Palo et al., 2007b; Sandford et al., 2008). Note that the high-latitude wintertime W3 of Fig. 6.5b almost certainly results from aliasing from this E2 wave.

To investigate the vertical structure of the waves, wave amplitudes as a function of time and height were considered. As examples of this analysis, Figure 6.6 presents the temperature amplitudes of W2, W3, W4 and E2 as functions of height and time. In the case of W2 (Fig. 6.6a) the data are presented for a latitude of 40°S since this is where the largest amplitudes occur. The results for W3, W4 and E2 are presented for latitudes of 40°S, 40°N and 70°S, respectively, because these wavenumbers maximise at those particular latitudes.

Considering the W2 results of Figure 6.6a, it can be seen that wave amplitudes are greatest between 80 and 100 km. Wave amplitudes are generally not significant below 70 km. The inter-annual variability evident in Figure 6.4a, is also evident in this presentation. However, the height at which maximum amplitude occurs is quite consistent from year to year.

The W3 results for a latitude of 40°S are shown in Figure 6.6b. The figure shows that wave amplitudes maximise at about 80 km in each year. The wave amplitudes go down to very small values, generally less than ~ 1.5 K, below 55 km. At the greatest heights observed the wave amplitudes appear to be declining. As in Figure 6.4b, large amplitudes occur only for a short time after the summer solstice and wave amplitudes are much smaller outside these times. Inter-annual variability is very strong e.g., in January 2006 wave amplitudes exceed 12 K whereas, in February 2008 and February 2009 wave amplitudes reach only about 5 K. Again, despite inter-annual variability in amplitude, the height at which amplitude maxima occur is remarkably consistent.

The results for W4 are shown for a latitude of 40°N in Figure 6.6c. As with the W3, the largest wave amplitudes occur in short bursts in late summer and are largely absent at other times of the year. Again, wave amplitudes display strong inter-annual variability. For example, wave amplitudes exceed 7 K in August 2006 but only reach ~ 4 K in July 2008. Despite this variability, the height of maximum amplitude is relatively consistent at about 75 km. Wave activity is evident at heights from about 55 km to the greatest height observed. As with the W3, the amplitudes reduce somewhat towards the greatest heights observed.

The E2 wave maximises at high latitudes as shown in Figure 6.5d. We will therefore consider the amplitude as a function of height for the E2 at 70° latitude rather than the 40° considered

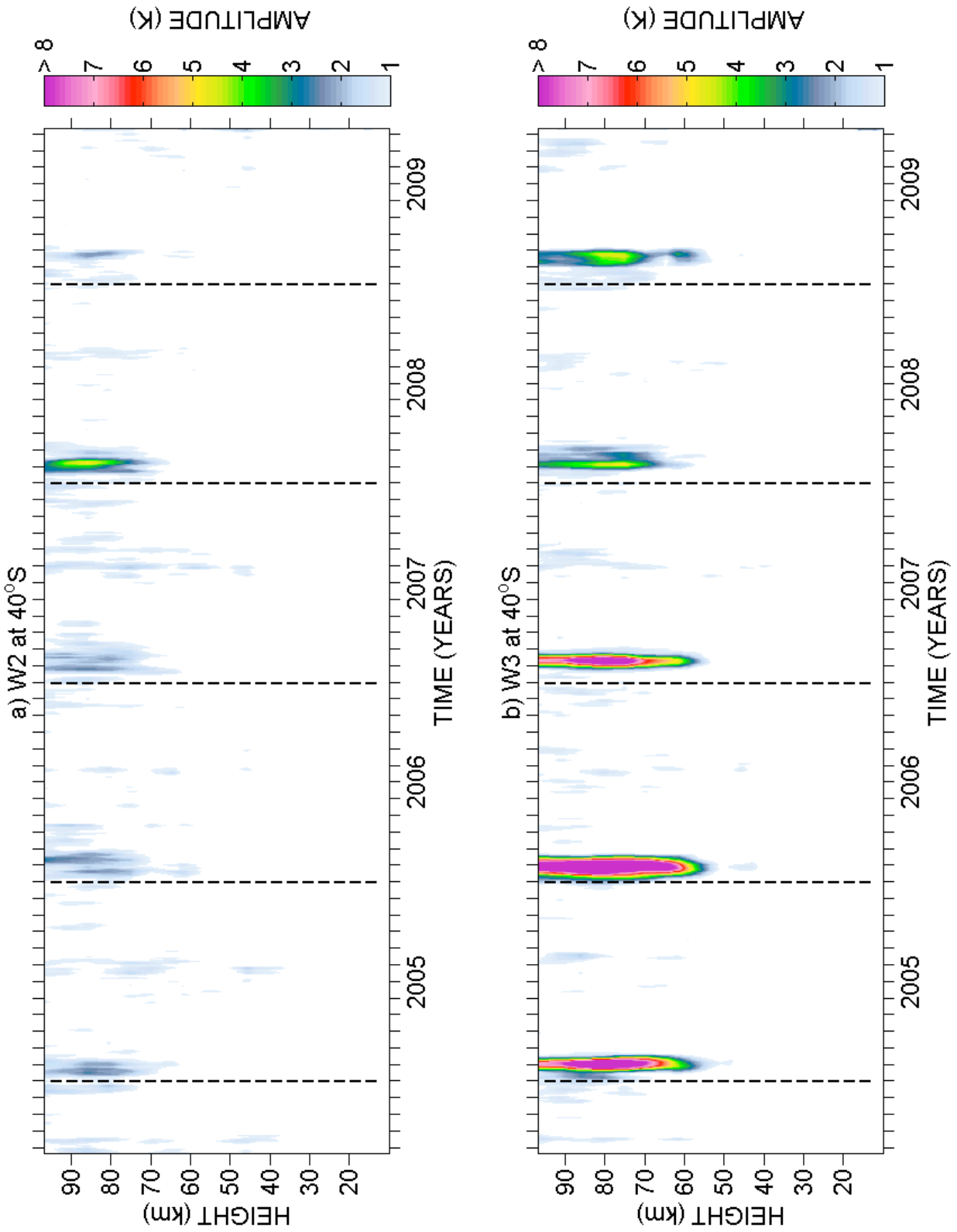

Figure 6.6: The temperature amplitude of 2-day planetary waves as a function of height and time. Amplitudes below 1 K are not plotted. The results are shown for a) wavenumber W2 at 40°S, b) W3 at 40 °S, c) W4 at 40°N and d) E2 at 70°S.

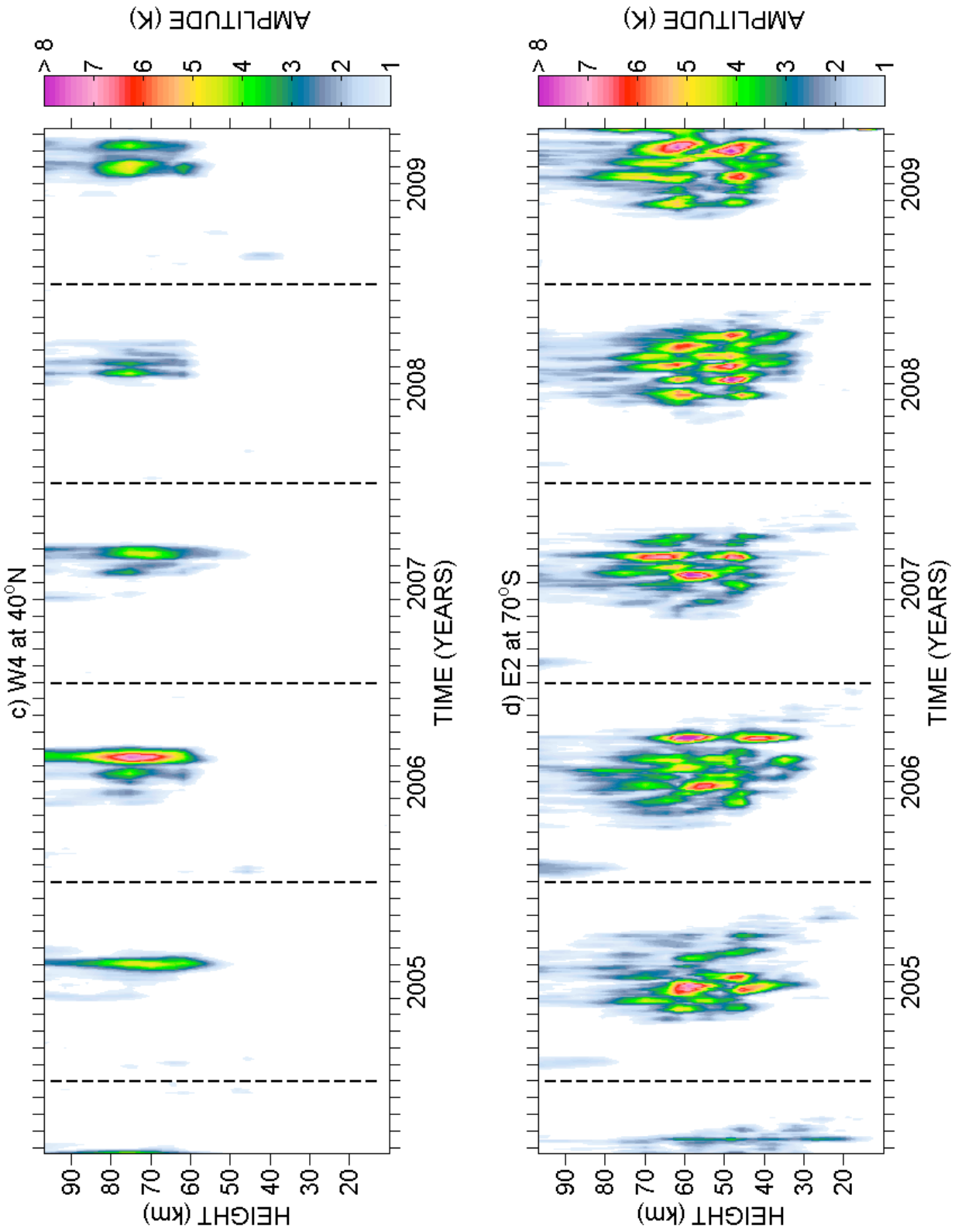

Figure 6.6: The temperature amplitude of 2-day planetary waves as a function of height and time. Amplitudes below 1 K are not plotted. The results are shown for a) wavenumber W2 at 40°S, b) W3 at 40 °S, c) W4 at 40°N and d) E2 at 70°S.

above. Figure 6.6d presents the E2 amplitudes at 70°S. It can be seen that the wave occurs in short bursts throughout the winter and spring months (June - September). Wave amplitudes maximise between 40 and 70 km, where they can reach $\sim$ 8 K. Above these heights the wave amplitudes reduce, but the wave is still clearly evident to heights of about 100 km. At these upper heights the amplitudes are generally about 2 K or less. It is this wintertime MLT-region wave activity at high latitude that has been reported in the radar and/or satellite studies of Nozawa et al. (e.g., 2003a) and Sandford et al. (2008).

In order to get a better understanding of the latitude-height structure of the various wavenumbers, the previous sets of data were combined into height-latitude contour plots for each month and then all the individual months were averaged to produce a set of composite months. Figure 6.7 presents the results of this composite-month, or superposed-epoch, analysis as plots of the temperature amplitude of the 2-day wave component wavenumbers as a function of height and latitude for the W2, W3, W4 wavenumbers, between 2004 and 2009 for January and July (plots for individual months and wavenumbers in the various years are not shown for reasons of space).

From the figure it is evident that the W2 temperature amplitude maximises in the upper heights observed, typically between 85 - 90 km. For example, the largest amplitudes observed are $\sim$ 2.2 K at heights near 80 km in the Southern Hemisphere in January at latitudes near 35°S. Northern Hemisphere amplitudes are somewhat smaller reaching to only about 1.5 K. There appears to be some penetration of the wave into the winter hemisphere from the Southern Hemisphere summer wave. There also appears to be significant W2 wave amplitudes around the stratopause at high latitudes in winter. For example, in the Northern-Hemisphere in January and in the Southern Hemisphere in July. However, as discussed in Sect. 6.2, this is most probably the aliased signature of a high-latitude E1 wave.

The mean W3 temperature amplitude maximises at mid-latitudes at heights of $\sim$ 80 km in summer in both hemispheres, i.e. similar to the heights at which the W2 maxima occur. W3 amplitudes are large, reaching up to 6 K in January in the Southern Hemisphere and 3 K in July in the Northern Hemisphere. This presentation highlights the fact noted earlier that the W3 wave amplitudes are significantly larger in the Southern Hemisphere than in the Northern Hemisphere. As with the W2 there also appears to be some penetration of the wave into the winter hemisphere from the Southern Hemisphere summer wave. The high-latitude W3 activity occurring at the winter stratopause is most probably a result of aliasing from the E2 wave as discussed in Sect. 6.2.

The W4 temperature amplitude maximises at a height of $\sim$ 70 - 80 km at mid-latitudes in summer in both hemispheres. The W4 wave thus maximises at a slightly lower height than that at which the W2 and W3 maximise. In contrast to the W2 and W3 components, the largest W4 amplitudes occur in the *Northern* Hemisphere where mean wave amplitudes exceed 3 K in July, whereas wave amplitudes are somewhat smaller in the Southern

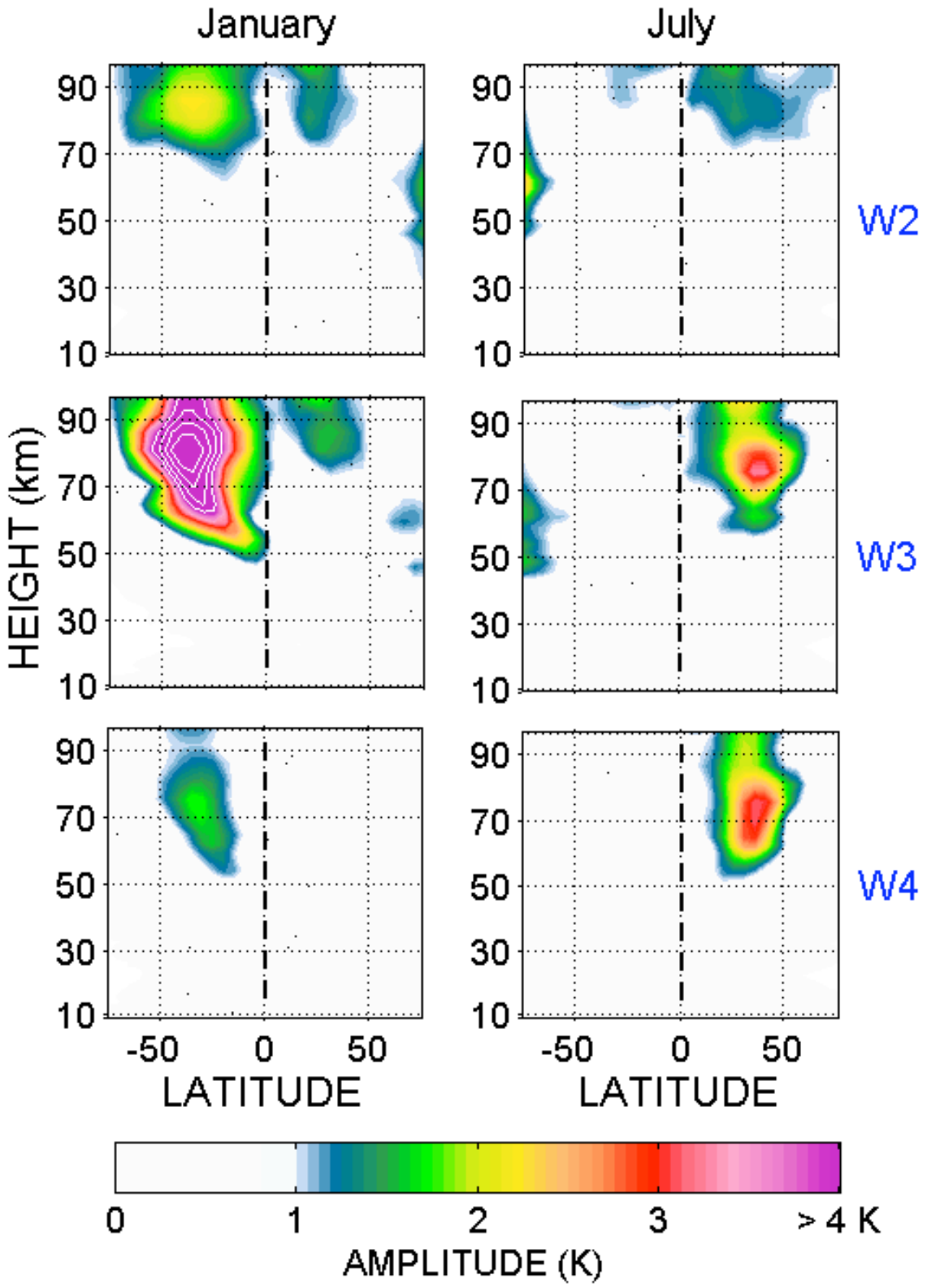

Figure 6.7: Composite year plots of 2-day wave temperature amplitudes as function of height and latitude in January and July for wavenumbers W2, W3 and W4. White contours are in steps of 0.5 K.

Hemisphere at 1.5 K.

Figure 6.7 suggests that there is some wave activity at high latitudes in *winter* for the W2 and W3 components; for example, in July in the Southern Hemisphere. However, as mentioned earlier we believe this high-latitude wintertime wave activity can in fact be explained as a result of the aliasing processes discussed in Sect. 6.2. There are two reasons for this conclusion.

Firstly, strong evidence that these high-latitude wintertime W3 signals are aliased is provided by the fact that their latitude and height structure are very similar to those of the larger-amplitude E2 wave observed simultaneously shown in Figure 6.8. In particular, the amplitude maxima occur just above and below 60 km and the waves are observed only at high wintertime latitudes. Critically, we also note that the results of Figure 6.3a suggest that such aliasing could occur strongly only at high-latitudes and can occur between E2 and W3 waves. We therefore conclude that these high-latitude wintertime W3 waves are primarily an aliased signature of the much stronger E2 wave.

Secondly, similar arguments to the above suggest that the high-latitude wintertime W2 signals are also aliased, in this case from an eastward propagating zonal wavenumber one oscillation (E1, shown in the upper right panel of Fig. 6.8). Again, the results of Fig 6.3b suggest that such aliasing could occur strongly at high latitudes between the E1 and W2 waves.

If we consider the full set of results presented above, we can identify several important features of the 2-day wave. These include:

1. The wave is a complex composed of W2, W3 and W4 components.

2. Aliasing from the winter-polar E2 wave is evident in the W3 component in this data set.

3. The seasonal and latitude-height structure of the W2, W3 and W4 waves are to first order similar, but do include some significant differences. For example, significant W2 and W3 amplitudes are evident from the equator to high latitudes in the Southern Hemisphere summer. This may simply reflect the larger amplitudes reached by the W2 and W3 in Southern Hemisphere summer.

4. The W2, W3 and W4 waves all reach maximum amplitudes at heights between 75 and 90 km.

5. There is a high degree of inter-annual variability and the peak amplitudes can vary by a factor of more than 3 from year to year.

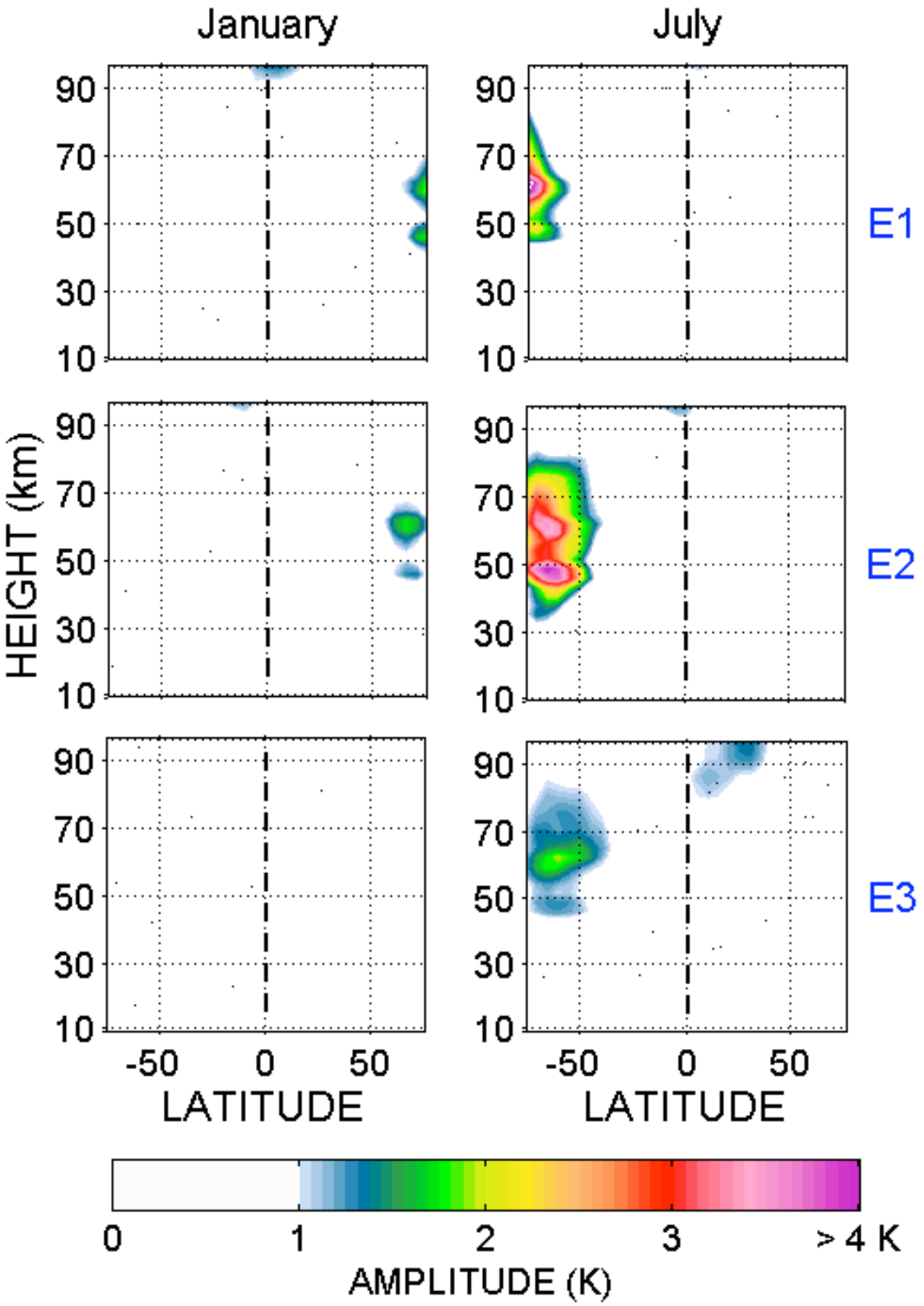

Figure 6.8: Composite year plots of 2-day wave temperature amplitudes as function of height and latitude in January and July for wavenumbers E1, E2 and E3. White contours are in steps of 0.5 K.

In order to investigate the differences between the climatologies of the W2, W3 and W4 waves, their behaviour was examined in more detail. Because these waves maximise in summer we will consider data from June to August in the Northern Hemisphere and December to February in the Southern Hemisphere. All the waves have largest amplitudes at heights between about 75 - 90 km so we will consider a height of 81 km. The particular question we will address is this, *how do the relative contributions to the 2-day wave complex of the W2, W3 and W4 components change over the course of a summer?* To do this, we calculated the wave amplitudes and periods using the least-squares method described in Sect. 6.2.

Firstly, we will consider the wave periods associated with wavenumbers W2, W3, W4 (identified above as the largest amplitude waves in summer). Figure 6.9 presents the wave periods of these particular wavenumbers as calculated from all available years of data and all latitudes at a height of 81 km as follows. In each hemisphere, for each twelve-day window described in Sect. 6.2 the wave period was calculated and recorded. The periods were then weighted against the amplitude of the wave and were then used to produce histograms of the frequency of occurrence of particular wave periods. Figure 6.9 presents the results of this analysis for the three wavenumbers W2, W3 and W4 calculated using only the summer data from each hemisphere. If we consider the figure we can see that all three components can occur with a range of periods. The W2 has periods generally between 44 and 51 hours. The W3 has periods generally between 48 and 52 hours. The W4 generally has shorter periods, usually less than 48 hours.

Secondly, we will consider the evolution over summer of the wave amplitudes associated with wavenumbers W2, W3, W4. Figure 6.10 presents the wave amplitudes of each component throughout the summer season for both hemispheres. The inter-hemispheric asymmetry evident in the earlier results is very clear in this figure. For example, the amplitude of the W3 is very much greater in the Southern Hemisphere than the Northern Hemisphere in 2004/2005, 2005/2006 and 2006/2007. Peak amplitudes reach 12 K in the summer of 2005/2006 in the Southern Hemisphere, whereas Northern Hemisphere amplitudes reach only 3 - 4 K. However, note that in the last two summers observed (2007/2008, 2008/2009) the Southern Hemisphere W3 amplitudes are in fact rather similar to those of the Northern Hemisphere. This appears to be the main cause of inter-annual variability, i.e., the main inter-annual variability comes from year-to-year fluctuations in the amplitude of the W3 component in the Southern Hemisphere.

In contrast, the amplitudes of the W2 and W4 components appear rather similar in the two hemispheres. The W2 amplitudes are generally less than about 3 K throughout the summer and the W4 amplitudes can reach as high as 6 K (e.g., 2006 in the Northern Hemisphere). The largest W3 amplitudes are in most summers quite short lived compared to the W4 component and so at the end of summer the W4 amplitudes are usually greater. This behaviour is seen in most years and is most prominent in, for example, the Northern Hemisphere summers of 2004, 2006, 2007 and 2009 and the Southern Hemisphere summers

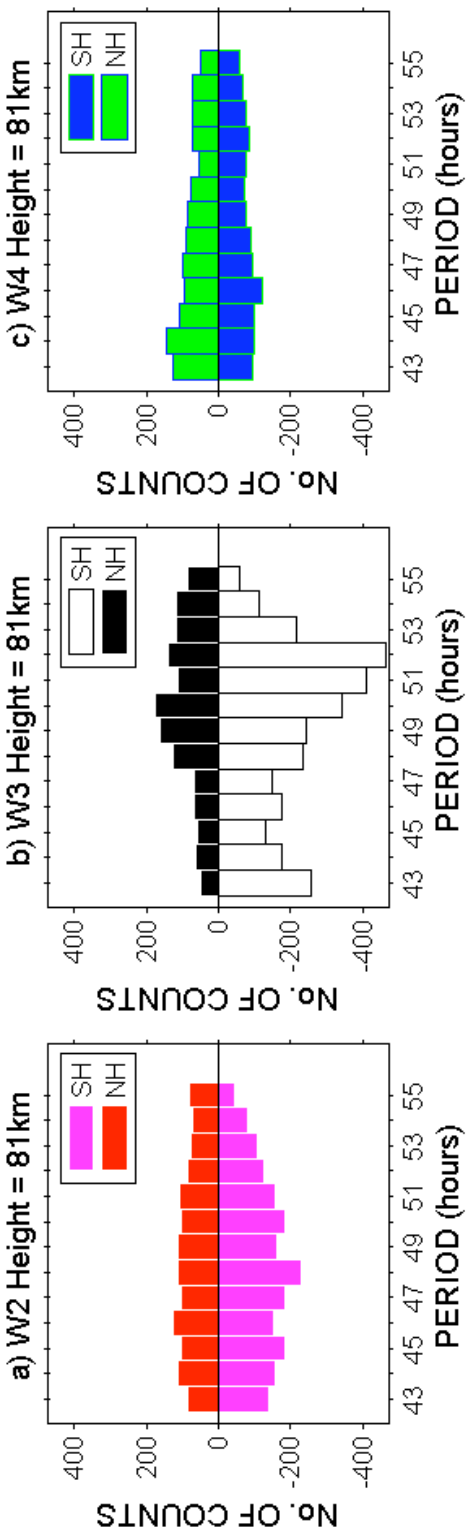

Figure 6.9: Histograms of wave period of zonal wavenumbers a) W2, b) W3 and c) W4. Data from summer only is used. In the Northern Hemisphere the data is from June, July and August and in the Southern Hemisphere the data are from December, January and February.

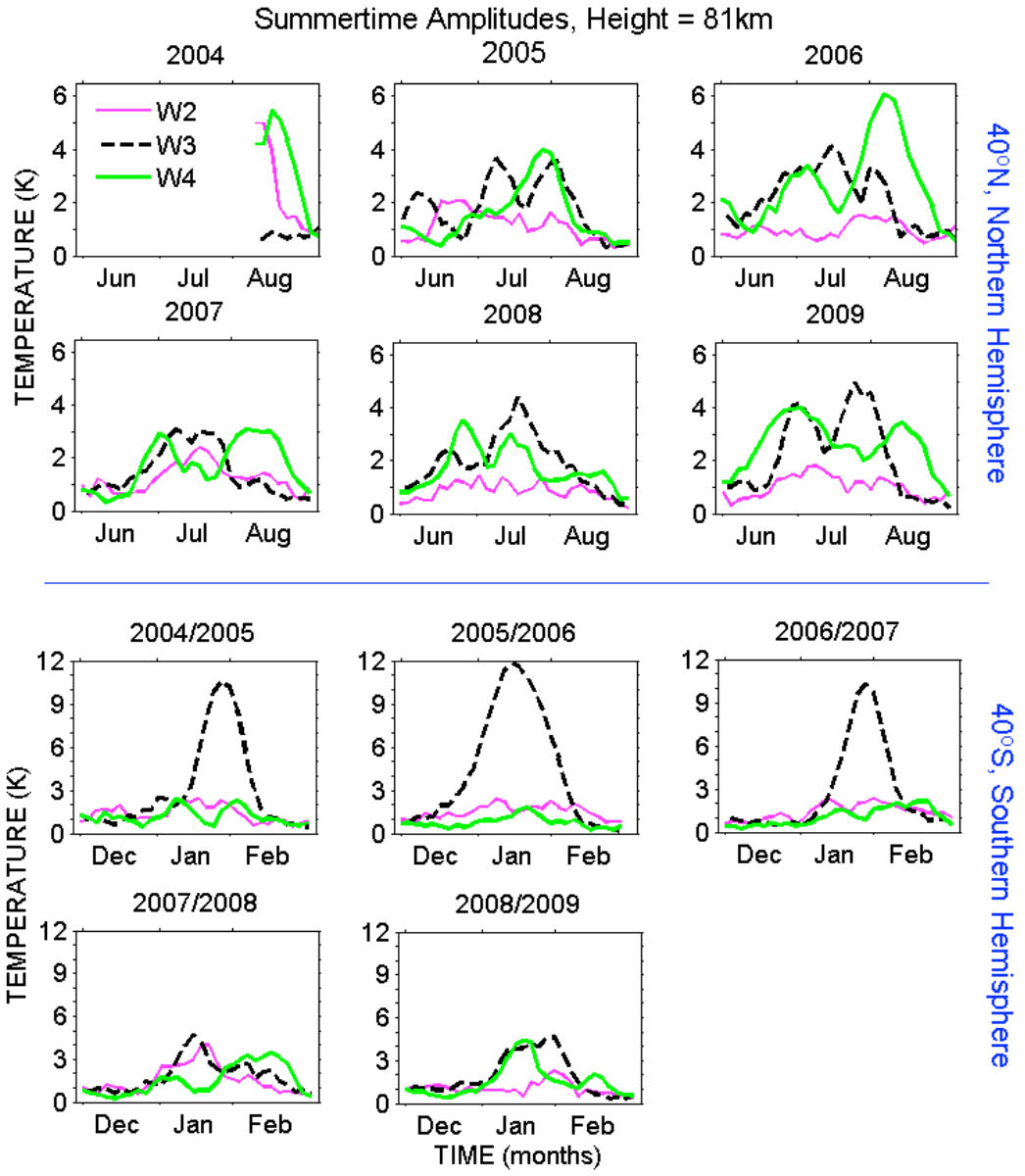

Figure 6.10: The amplitude of the component wavenumbers W2, W3 and W4 of the 2-day wave in summer at a height of 81 km. The top six panels show data from June - August from 2004 - 2009 at 40° in the Northern Hemisphere. The lower five panels show data from December - February 2004/5 to 2008/9 at 40° in the Southern Hemisphere.

of 2007/2008 and 2008/2009. In other words, in the middle of summer the 2-day wave is dominated by the W3 component, but by the end of summer it has become dominated by the W4 component.

To examine this behaviour in more detail we averaged the data regardless of the year to produce superposed-epoch summers for latitudes of 40°N and 40°S at a height of 81 km. Figure 6.11 presents this data for W2, W3 and W4 components with the data from each hemisphere presented on the same plot to enable comparison.

From the figures it can be seen that the mean W2 amplitudes are generally quite similar in both hemispheres although slightly larger in the Southern Hemisphere. The mean W3 component is again seen to be significantly larger in the Southern Hemisphere, 7.5 K c.f. ~ 3 K in the Northern Hemisphere. Further, W3 amplitudes appear to maximise slightly later in the summer in the Southern Hemisphere. Mean W4 amplitudes are significantly larger in the Northern Hemisphere throughout the summer. As noted earlier, W4 amplitudes remain large until well into late summer (Feb/Aug) where they then exceed the W3 amplitudes, resulting in a 2-day wave which is primarily a W4 oscillation at the end of summer. This is illustrated further in the case of the Northern Hemisphere in Fig. 6.11d, which presents the superposed-epoch results for all three wavenumbers, but only for the Northern Hemisphere. It can be seen that mean W3 amplitudes have declined to small values in August but that there is still apparent amplitude in the W4 component.

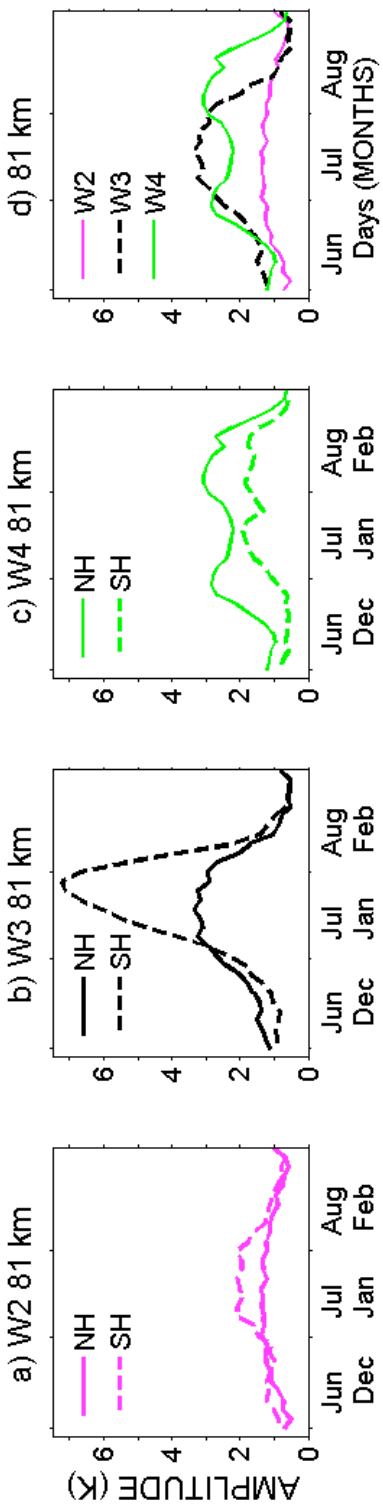

Figure 6.11: Composite year amplitudes of the component wavenumbers of the 2-day wave in summer at a height of 81 km for both hemispheres and for various wavenumbers.

6.4 Discussions

The global pattern of 2-day wave activity in terms of height, latitude and season presented above provides a planetary-scale overview of the structure of the 2-day wave. The ground-based observations described in Chapter 5 and Sect. 6.1, provide localised measurements that can be seen to fit with good agreement into this overarching context. In particular, the total level of 2-day wave amplitude (i.e. the sum of wave amplitudes from wavenumbers W2, W3 and W4) maximises after the summer solstice at mid-latitudes and in the upper mesosphere and is largest in the Southern Hemisphere.

A significant feature of our observations is the very different amplitudes and seasonal variation in amplitude exhibited by the W2, W3 and W4 components. A limited number of modelling studies have attempted to explain the relative contributions of different waves with periods near 2 days to the total of observed 2-day wave activity. Salby and Callaghan (2001) considered the growth of waves with periods near 2 days and wavenumbers of W1, W2, W3 and W4. Wave activity generated by instabilities near the wave's critical line was found to disperse globally into Rossby-gravity modes. In conditions of strong easterly winds around the solstice, the e-folding times for the growth in amplitude of the four wavenumbers W1 to W4 were found to be approximately > 40, > 40, 5 and 10 days, respectively.

These slow growth rates for the W1 and W2 may well explain the negligible W1 and small W2 amplitudes we observe and the larger solstitial amplitudes we observe for the W3 and W4. In the weaker easterlies of later summer (specifically, July) Salby and Callaghan (2001) found the W3 and W4 to amplify in the mesosphere at about the same rate. Again, this provides a plausible explanation for the comparable amplitudes of the W3 and W4 we frequently observe in late summer. We also note that the transition from a predominantly W3 to a W4 structure was also reported in the modelling study of Norton and Thuburn (1996). They speculated that the wavenumber 4 may originate from the spectrum of wavenumbers that can be excited by different zonal jet profiles, following the theoretical work of Plumb (1983). This transition to similar W3 and W4 amplitudes was also observed using satellite and ground-based radars in the boreal summer of 1994 by Riggin et al. (2004). They found that in the Northern Hemisphere, during summer, the W3 component had significant amplitudes during July and August. The W4 amplitudes exceeded those of the W3 in August, after the W3 had reduced from peak amplitudes. Our results show that this behaviour is representative of the 2-day wave in more than one year.

Salby and Callaghan (2001) reported that very modest changes in zonal mean wind could sharply alter growth rates but had little impact on wave period or structure. This sensitivity to subtle differences in background wind conditions may, in part, explain the dramatic inter-annual and inter-hemispheric differences in amplitude evident in the W3 and W4 components. McCormack et al. (2009) examined the 2-day wave in January of 2006 using

global synoptic fields in the Navy Operational Global Atmospheric Prediction System Advanced Level Physics, High Altitude (NOGAPS-ALPHA) forecasting assimilation system. They found evidence for a relationship between the disturbed Northern Hemisphere winter stratosphere and forcing of the 2-day wave in the Southern Hemisphere summer mesosphere. Variability of the planetary-wave activity in the winter hemisphere may thus influence 2-day wave amplitudes in the summer hemisphere and further contribute to the observed inter-annual variability.

The W4 was identified by Salby and Callaghan (2001) as a Rossby-gravity (4, 0) mode. They presented a solstitial geopotential-amplitude structure for this mode which suggests that in the summer mesosphere it reaches largest values from the tropics to middle/high latitudes at heights increasing from $\sim$ 80 km in the tropics to $\sim$ 90 km at higher latitudes. They suggested only limited penetration of this wave activity across the equator into the winter hemisphere. This is shown in Figure 6.12, which is Fig. 10, in Salby and Callaghan (2001). Our results (Figure 6.7) show that their model reproduces the gross features of the observed W4 structure (and actually show no evidence of significant penetration into the winter hemisphere). These similarities in structure between the modelled (4, 0) Rossby-gravity mode of Salby and Callaghan (2001) and the observed W4 reported here provides strong support for the suggestion that the W4 is in fact a (4, 0) Rossby-gravity mode.

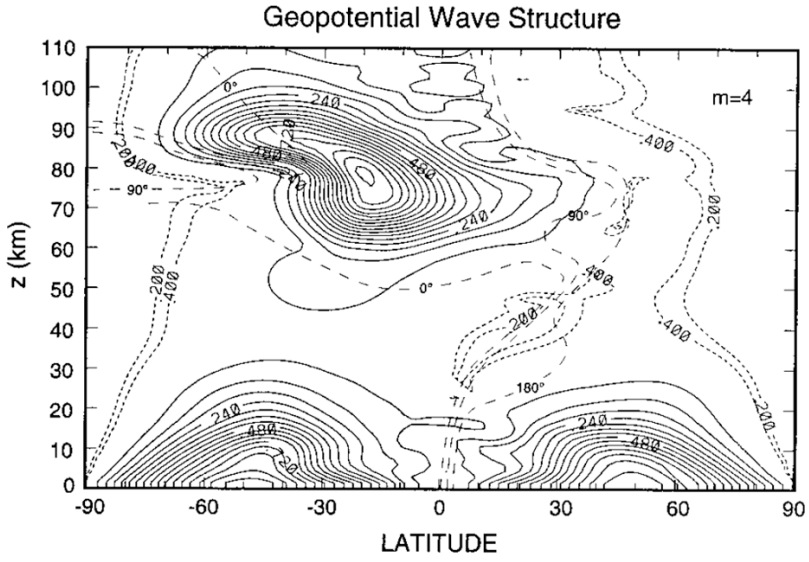

Figure 6.12: Geopotential amplitude (solid) and phase (dashed) corresponding to the fastest-growing pole of wavenumber 4 in January. After Salby and Callaghan (2001).

6.5 Final note

The work in this Chapter was extended to a further study in an international collaboration bringing together a number of complimentary measurements of the summertime 2-day wave. The focus of the study was to understand some of the causes of the short-term variability in 2-day wave amplitude. The data used in the study include a number of measurements made over Europe. These are OH temperature measurements from Wuppertal (51°N, 7°E) and Hohenpeißenberg (48°N, 11°E) and MF radar winds from Juliusruh (55°N, 13°E). EOS MLS temperatures were used to provide a global perspective.

This author's contribution to the experiment was the analysis of the Aura MLS data to determine the periods and amplitudes of the W2, W3 and W4 components of the 2-day wave observed over Europe in summer. These measurements were then combined with the OH measurements described above. This study also investigated the excitation mechanisms of the summertime 2-day wave by considering the role of baroclinic instability. A key result of this study was that, in the years observed, the amplitude of the 2-day wave often displayed three successive maxima (a triplet structure). This study has been published as: Offermann, D., P. Hoffmann, P. Knieling, R. Koppmann, J. Oberheide, D.M. Riggin, V.M. Tunbridge, and W. Steinbrecht. Quasi-Two Day Waves in the summer mesosphere: Triple structure of amplitudes and long-term development. *Journal of Geophysical Research-Atmospheres*, 116, D00P02, doi:10.1029/2010JD015051.

6.6 Conclusions

EOS Aura MLS temperatures were analysed from 2004 - 2009 in a latitude range of 70°N to 70°S. In both hemispheres, during the summer months, a large amplitude 2-day wave was observed with amplitudes reaching up to 12 K in the Southern Hemisphere. These large-amplitude summertime waves were then considered in more detail. A modelling study has shown that significant aliasing can occur between wavenumbers associated with the 2-day wave. We have identified aliasing from an E2 high-latitude wave as something which can give rise to a spurious high-latitude W3 signal. Note that high-latitude E2 2-day waves have been reported in a numbers of studies (e.g., Nozawa et al., 2003a; Sandford et al., 2008) and so such aliasing could potentially be misleading.

The data show that the summertime 2-day wave is a complex of wavenumbers W2, W3 and W4 in both hemispheres. The W3 and W4 are the dominant wavenumbers having the largest amplitudes throughout each summer compared with the W2 which has consistently smaller amplitudes.

In the Southern Hemisphere the W3 amplitudes are largest and the 2-day wave is therefore dominated by the W3 component with amplitudes reaching up to about 11 K in 3 of the 5 summers observed. When the W3 reaches such large amplitudes it is reasonably short lived, lasting only about one month. The W4 component does not reach amplitudes larger than 3 K during times of large W3 amplitudes making the 2-day wave predominantly a W3 wave during the summers of (2004/2005, 2005/2006, 2006/2007). During the summers of 2007/2008 and 2008/2009 the W3 reached amplitudes up to about 5 K only half that of the previous years. During this time the W4 had a similar amplitude making the resultant 2-day wave a mixture of W3 and W4 components. Despite the large degree of inter-annual variability in amplitudes, the structure of the waves in terms of height and latitude remains remarkably constant from year to year.

In the Northern Hemisphere the 2-day wave is a mixture of W2, W3 and W4 waves. The W4 wave has larger amplitudes in this hemisphere and in 2006 was the largest amplitude of all the wavenumbers, reaching amplitudes up to about 6 K.

In both hemispheres the W4 appears to be a longer-lived wave and persists to have large amplitudes once the W3 has died away. This is apparent in most years observed.

In this study we have found that the 2-day wave is nearly always a mixture of the W3 and W4 wavenumbers rather than just a W3 wave and that the W4 appears to be the (4, 0) normal mode.

Chapter 7

Suggestions for Future Work

Reviewing the work presented in this thesis a number of logical next steps can be identified to advance the science. These include;

1. Chapters 5 and 6 use climatological monthly variances and 12-day amplitudes to measure the variability of the 2-day wave. However, these analyses mask a lot of short-term variability of the wave and background winds. Both the radar and satellite instruments are capable of measuring shorter time scales and therefore a study of the short-term variability of the 2-day wave over the course of a season could be investigated. Such short-term variability may result from interactions with other planetary waves and fluctuations in the strength of forcing through instabilities and fluctuations in the propagation environment (mean winds) through which the wave propagates. These processes are still not well understood but can be explored through such short-term studies.

2. Some mesospheric data sets are now equal in length to or greater than the 11-year solar cycle. For instance, the mesospheric winds and temperatures measured by the Esrange radar span the period from late 1999 to the present and may continue for many years yet. Upper-atmospheric processes such as tides are known to be influenced by fluctuations in their forcing resulting from variations in the UV flux entering the atmosphere. Therefore, an investigation of the variability of atmospheric processes such as tides and planetary waves etc. over the course of a solar cycle could be explored.

3. Further to the studies of wave climatology and variability in Chapters 5 and 6, a study into the excitation mechanisms of the 2-day wave could be conducted by studying the barotrophic and baroclinic instabilities that occur during times of high variability of

the wave. This would allow a quantification of the relative roles of wave excitation and propagation in the observed total level of wave activity. These instabilities can be deduced from global observations of the wind/temperature fields of the middle atmosphere made by satellites, complemented by measurements of wind shear made by ground-based radars.

4. Chapter 6 revealed the significant role of the W4 (4, 0) Rossby-gravity mode particularly in the northern hemisphere. Modelling studies could be used to investigate the excitation of this particular mode and to establish the reasons behind its interhemispheric variability.

5. Chapters 5 and 6 are single instrument studies of the 2-day wave. This could be expanded into a multi-instrument experiments of the 2-day wave could be conducted to look at the long-term and short-term variability of the wave.

Bibliography

A. J. G. Baumgaertner, A. J. McDonald, R. E. Hibbins, D. C. Fritts, D. J. Murphy, and R. A. Vincent. Short-period planetary waves in the Antarctic middle atmosphere. *Journal of Atmospheric and Solar-Terrestrial Physics*, 70(10):1336–1350, 2008.

C. L. Beldon and N. J. Mitchell. Gravity waves in the mesopause region observed by meteor radar, 2: Climatologies of gravity waves in the Antarctic and Arctic. *Journal of Atmospheric and Solar-Terrestrial Physics*, 71(8-9):875–884, 2009. ISSN 1364-6826. doi: 10.1016/j.jastp.2009.03.009.

Z. Ceplecha, J. Borovicka, W. G. Elford, D. O. Revelle, R. L. Hawkes, V. Porubcan, and M. Simek. Meteor phenomena and bodies. *Space Science Reviews*, 84(3-4):327–471, 1998.

J. G. Charney and P. G. Drazin. Propagation of planetary-scale disturbances from the lower into the upper atmosphere. *Journal of Geophysical Research-Atmospheres*, 66(1):83–109, 1961.

R. R. Clark, A. C. Current, A. H. Manson, C. E. Meek, S. K. Avery, S. E. Palo, and T. Aso. Hemispheric properties of the 2-day wave from mesosphere lower-thermosphere radar observations. *Journal of Atmospheric and Terrestrial Physics*, 56(10):1279–1288, 1994. ISSN 0021-9169.

S. Close, S. M. Hunt, M. J. Minardi, and McKeen F. M. Meteor shower characterization at Kwajalein Missile Range. *Lincoln Laboratory Journal*, 12(1):33–44, 2000.

L. Coy, I. Stajner, A. M. DaSilva, J. Joiner, R. B. Rood, S. Pawson, and S. J. Lin. High-frequency planetary waves in the polar middle atmosphere as seen in a data assimilation system. *Journal of the Atmospheric Sciences*, 60(24):2975–2992, 2003.

R. L. Craig, R. A. Vincent, G. J. Fraser, and M. J. Smith. The quasi 2-day wave in the Southern Hemisphere mesosphere. *Nature*, 287(5780):319–320, 1980.

R. L. Craig, R. A. Vincent, S. P. Kingsley, and H. G. Muller. Simultaneous observations of the quasi 2-day wave in the northern and southern hemispheres. *Journal of Atmospheric and Terrestrial Physics*, 45(8-9):539–541, 1983.

V. I. Fomichev, A. I. Jonsson, J. De Grandpre, S. R. Beagley, C. McLandress, K. Semeniuk, and T. G. Shepherd. Response of the middle atmosphere to CO2 doubling: Results from the Canadian Middle Atmosphere Model. *Journal of Climate*, 20(7):1121–1144, April 1 2007. ISSN 0894-8755. doi: {10.1175/JCLI4030.1}.

J. M. Forbes and X. Zhang. Quasi 2-day oscillation of the ionosphere: A statistical study. *Journal of Atmospheric and Solar-Terrestrial Physics*, 59(9):1025–1034, 1997. ISSN 1364-6826.

J. M. Forbes, R. Guffee, X. Zhang, D. Fritts, D. Riggin, A. Manson, C. Meek, and R. A. Vincent. Quasi 2-day oscillation of the ionosphere during summer 1992. *Journal of Geophysical Research-Space Physics*, 102(A4):7301–7305, 1997. ISSN 0148-0227.

Forbes, J. M. *Tidal and Planetary Waves*. American Geophysical Union, 1995. ISBN 0-87590-044-5.

D. C. Fritts, J. R. Isler, R. S. Lieberman, M. D. Burrage, D. R. Marsh, T. K. Nakamura, T. Tsuda, and R. A. Vincent. Two-day wave structure and mean flow interactions observed by radar and high resolution doppler imager. *Journal of Geophysical Research-Atmospheres*, 104(D4):3953–3969, 1999.

D. C. Fritts, D. Janches, and W. K. Hocking. Southern Argentina Agile Meteor Radar: Initial assessment of gravity wave momentum fluxes. *Journal of Geophysical Research-Atmospheres*, 115, 2010. ISSN 0148-0227. doi: 10.1029/2010JD013891.

M Gadsden. The secular changes in noctilucent cloud occurrence: Study of a 31-year sequence to clarify the causes. In Chakrabarty, DK and Gupta, SP, editor, *Middle Atmosphere: Changes and Electrodynamics*, volume 20 of *Advances in Space Research*, pages 2097–2100, 1997. ISBN 0-08-043308-1. C2.1 and C2.3 Symposia of COSPAR Scientific Commission C on Middle Atmosphere - Changes and Electrodynamics, at the 31st COSPAR Scientific Assembly, BIRMINGHAM, ENGLAND, JUL 14-21, 1996.

R. R. Garcia and S. Solomon. A numerical-model of the zonally averaged dynamical and chemical structure of the middle atmosphere. *Journal of Geophysical Research-Oceans and Atmospheres*, 88(C2):1379–1400, February 1983.

R. R. Garcia, R. Lieberman, J. M. Russell, and M. G. Mlynczak. Large-scale waves in the mesosphere and lower thermosphere observed by saber. *Journal of the Atmospheric Sciences*, 62(12):4384–4399, Dec 2005. ISSN 0022-4928.

M. A. Geller. Dynamics of the middle atmosphere. *Space Science Reviews*, 34(4):359–375, 1983. ISSN 0038-6308.

M. Glass, J. L. Fellous, M. Massebeuf, A. Spizzichino, I. A. Lysenko, and Y. I. Portniaghin. Comparison and interpretation of results of simultaneous wind measurements in lower thermosphere at Garchy (France) and Obninsk (USSR) by meteor radar technique. *Journal of Atmospheric and Terrestrial Physics*, 37(8):1077–1087, 1975. ISSN 0021-9169.

S. Gurubaran, S. Sridharan, T. K. Ramkumar, and R. Rajaram. The mesospheric quasi-2-day wave over Tirunelveli (8.7 degrees N). *Journal of Atmospheric and Solar-Terrestrial Physics*, 63(10):975–985, 2001.

T. J. Harris and R. A. Vincent. The quasi-2-day wave observed in the equatorial middle atmosphere. *Journal of Geophysical Research-Atmospheres*, 98(D6):10481–10490, 1993.

J. H. Hecht, R. L. Walterscheid, L. J. Gelinas, R. A. Vincent, I. M. Reid, and J. M. Woithe. Observations of the phase-locked 2-day wave over the Australian sector using medium-frequency radar and airglow data. *Journal of Geophysical Research-Atmospheres*, 115, 2010. ISSN 0148-0227. doi: 10.1029/2009JD013772.

W. K. Hocking, B. Fuller, and B. Vandepeer. Real-time determination of meteor-related parameters utilizing modern digital technology. *Journal of Atmospheric and Solar-Terrestrial Physics*, 63(2-3):155–169, 2001. 1364-6826 doi: DOI: 10.1016/S1364-6826(00)00138-3.

P. Hoffmann, G. von Cossart, and W. Singer. Dynamical influences on PMSE and NLC derived from radar and lidar measurements at ALOMAR. *14th ESA symposium on european rocket and balloon programmes and related research*, 437:305–308, 1999. ISSN 0379-6566.

P. Hoffmann, W. Singer, and D. Keuer. Variability of the mesospheric wind field at middle and Arctic latitudes in winter and its relation to stratospheric circulation disturbances. *Journal of Atmospheric and Solar-Terrestrial Physics*, 64(8-11):1229–1240, 2002. ISSN 1364-6826.

P. Hoffmann, M. Rapp, R. Latteck, A. Serafimovich, and W. Singer. Multiple layer PMSE structures: Statistical results from six years of PMSE observations and possible physical explanations of their observed properties. *16th ESA symposium on european rocket and balloon programmes and related research, proceedings*, 530:315–320, 2003. ISSN 0379-6566.

P. Hoffmann, M. Rapp, A. Serafimovich, and R. Latteck. On the occurrence and formation of multiple layers of polar mesosphere summer echoes. *Geophysical Research Letters*, 32 (5), 2005. ISSN 0094-8276. doi: 10.1029/2004GL021409.

P. Hoffmann, A. Serafimovich, D. Peters, P. Dalin, R. Goldberg, and R. Latteck. Inertia gravity waves in the upper troposphere during the MaCWAVE winter campaign - Part 1: Observations with collocated radars. *Annales Geophysicae*, 24(11):2851–2862, 2006. ISSN 0755-0685.

P. Hoffmann, W. Singer, D. Keuer, W. K. Hocking, M. Kunzec, and Y. Murayama. Latitudinal and longitudinal variability of mesospheric winds and temperatures during stratospheric warming events. *Journal of Atmospheric and Solar-Terrestrial Physics*, 69(17-18): 2355–2366, 2007. ISSN 1364-6826. doi: 10.1016/j.jastp.2007.06.010.

P. Hoffmann, E. Becker, W. Singer, and M. Placke. Seasonal variation of mesospheric waves at northern middle and high latitudes. *Journal of Atmospheric and Solar-Terrestrial Physics*, 72(14-15):1068–1079, 2010. ISSN 1364-6826. doi: 10.1016/j.jastp.2010.07.002.

S. S. Hough. On the application of harmonic analysis to the dynamical theory of the tides. Part I. On Laplace's "Oscillations of the First Species," and on the dynamics of the ocean currents. *Philosophical Transactions of the Royal Society of London Series a-Mathematical and Physical Sciences*, A189(7):201–257, 1897.

S. S. Hough. On the application of harmonic analysis to the dynamical theory of tides, Part II, On the general integration if Laplace's dynamical equations. *Philosophical Transactions of the Royal Society of London Series a-Mathematical and Physical Sciences*, A191:139–185, 1898.

John T. Houghton. *The Physics of Atmospheres*. Cambridge University Press, second edition, 1989. ISBN 0-521-33956-1.

C. Jacobi, R. Schminder, and D. Kurschner. The quasi 2-day wave as seen from D1 LF wind measurements over Central Europe (52 degrees N, 15 degrees E) at Collm. *Journal of Atmospheric and Solar-Terrestrial Physics*, 59(11):1277–1286, 1997.

C. Jacobi, R. Schminder, and D. Kurschner. Non-linear interaction of the quasi 2-day wave and longterm oscillations in the summer midlatitude mesopause region as seen from LF D1 wind measurements over Central Europe (Collm, 52 degrees N, 15 degrees E). *Journal of Atmospheric and Solar-Terrestrial Physics*, 60(12):1175–1191, 1998.

M. Y. Kulikov. Theoretical investigation of the influence of a quasi-2-day wave on nonlinear photochemical oscillations in the mesopause region. *Journal of Atmospheric and Solar-Terrestrial Physics*, 112(D2), 2007. ISSN 0148-0227.

C. La Hoz, Havnes O., L. I. Naesheim, and D. L. Hysell. Observations and theories of polar mesospheric summer echoes at a bragg wavelength of 16 cm. *Journal of Geophysical Research*, 111(D04203):1–19, 2006. doi: doi:10.1029/2005JD006044.

L. R. Lait and J. L. Stanford. Fast, long-lived features in the polar stratosphere. *Journal of the Atmospheric Sciences*, 45(24):3800–3809, 1988.

T. Li, C. Y. She, S. E. Palo, Q. Wu, H. L. Liu, and M. L. Salby. Coordinated lidar and TIMED observations of the quasi-two-day wave during August 2002-2004 and possible quasi-biennial oscillation influence. *Advances in Space Research*, 41(9):1462–1470, 2008.

R. S. Lieberman. Eliassen-palm fluxes of the 2-day wave. *Journal of the Atmospheric Sciences*, 56(16):2846–2861, 1999.

V. Limpasuvan and D. L. Wu. Two-day wave observations of UARS Microwave Limb Sounder mesospheric water vapor and temperature. *Journal of Geophysical Research-Atmospheres*, 108(D10), 2003.

V. Limpasuvan and D. L. Wu. Anomalous two-day wave behavior during the 2006 austral summer. *Geophysical Research Letters*, 36, 2009.

V. Limpasuvan, C. B. Leovy, and Y. J. Orsolini. Observed temperature two-day wave and its relatives near the stratopause. *Journal of the Atmospheric Sciences*, 57(11):1689–1701, 2000.

V. Limpasuvan, D. L. Wu, M. J. Schwartz, J. W. Waters, Q. Wu, and T. L. Killeen. The two-day wave in EOS MLS temperature and wind measurements during 2004-2005 winter. *Geophysical Research Letters*, 32(17), 2005.

N. J. Livesey and W. V. Snyder. EOS MLS retrieval processes algorithm theoretical basis. Version 2.0 D-16159, Jet Propulsion Laboratory Document, Jet Propulsion Laboratory, California Institude of Technology, Pasadena, California, 91109-8099, 2004.

N. J. Livesey, W. Van Snyder, W. G. Read, and P. A. Wagner. Retrieval algorithms for the EOS Microwave Limb Sounder (MLS). *Ieee Transactions on Geoscience and Remote Sensing*, 44(5):1144–1155, 2006.

N. J. Livesey, W. G. Read, A. Lambert, R. E. Cofield, D. T. Cuddy, L. Froidevaux, R. A. Fuller, R. F. Jarnot, J. H. Jiang, Y. B. Jiang, B. W. Knosp, L. J. Kovalenko, H. M. Pickett, H. C. Pumphrey, M. L. Santee, M. J. Schwartz, P. C. Stek, P. A. Wagner, J. W. Waters, and D. L. Wu. Version 2.2 level 2 data quality and description document. Version 2.2 D-33509, Jet Propulsion Laboratory Document, Jet Propulsion Laboratory, California Institude of Technology, Pasadena, California, 91109-8099, May 2007.

J. London. *Radiative Energy Sources and Sinks in the Stratosphere and Mesosphere*. Proceedings of the NATO Advanced Study Institute on Atmospheric Ozone: Its Variation and Human Influences, 1980.

M. S. Longuet-Higgins. The eigenfunctions of Laplace's tidal equations over a sphere. *Philosophical Transactions of the Royal Society of London Series a-Mathematical and Physical Sciences*, 262(1132):511–607, February 29 1968.

Y. Luo, A. H. Manson, C. E. Meek, C. K. Meyer, M. D. Burrage, D. C. Fritts, C. M. Hall, W. K. Hocking, J. MacDougall, D. M. Riggin, and R. A. Vincent. The 16-day planetary waves: multi-MF radar observations from the arctic to equator and comparisons with the HRDI measurements and the GSWM modelling results. *Annales Geophysicae*, 20(5): 691–709, 2002. Times Cited: 17.

A. H. Manson, C. E. Meek, T. Chshyolkova, S. K. Avery, D. Thorsen, J. W. MacDougall, W. Hocking, Y. Murayama, K. Igarashi, S. P. Namboothiri, and P. Kishore. Longitudinal and latitudinal variations in dynamic characteristics of the MLT (70-95 km): a study involving the CUJO network. *Annales Geophysicae*, 22(2):347–365, 2004a.

A. H. Manson, C. E. Meek, C. M. Hall, S. Nozawa, N. J. Mitchell, D. Pancheva, W. Singer, and P. Hoffmann. Mesopause dynamics from the Scandinavian triangle of radars within the PSMOS-DATAR Project. *Annales Geophysicae*, 22(2):367–386, 2004b.

J. P. McCormack, S. D. Eckermann, K. W. Hoppel, and R. A. Vincent. Amplification of the quasi-two day wave through nonlinear interaction with the migrating diurnal tide. *Geophysical Research Letters*, 37, 2010. ISSN 0094-8276. doi: 10.1029/2010GL043906.

J. P. McCormack, L. Coy, and K. W. Hoppel. Evolution of the quasi 2-day wave during January 2006. *Journal of Geophysical Research-Atmospheres*, 114, OCT 28 2009. ISSN 0148-0227. doi: {10.1029/2009JD012239}.

C. E. Meek and A. H. Manson. Summer planetary-scale oscillations: Aura MLS temperature compared with ground-based radar wind. *Annales Geophysicae*, 27(4):1763–1774, 2009.

C. E. Meek, A. H. Manson, S. J. Franke, W. Singer, P. Hoffmann, R. R. Clark, T. Tsuda, T. Nakamura, M. Tsutsumi, M. Hagan, D. C. Fritts, J. Isler, and Y. I. Portnyagin. Global study of Northern Hemisphere quasi-2-day wave events in recent summers near 90 km altitude. *Journal of Atmospheric and Terrestrial Physics*, 58(13):1401–1411, 1996.

A. W. Merkel, D. W. Rusch, S. E. Palo, J. M. Russell, and S. M. Bailey. Mesospheric planetary wave effects on global PMC variability inferred from AIM-CIPS and TIMED-SABER for the northern summer 2007 PMC season. *Journal of Atmospheric and Solar-Terrestrial Physics*, 71(3-4):381–391, 2009. ISSN 1364-6826.

E. Merzlyakov, D. Pancheva, N. Mitchell, J. M. Forbes, Y. I. Portnyagin, S. Palo, N. Makarov, and H. G. Muller. High- and mid-latitude quasi-2-day waves observed simultaneously by four meteor radars during summer 2000. *Annales Geophysicae*, 22(3): 773–788, 2004.

N. J. Mitchell and C. L. Beldon. Gravity waves in the mesopause region observed by meteor radar: 1. a simple measurement technique. *JOURNAL OF ATMOSPHERIC AND SOLAR-TERRESTRIAL PHYSICS*, 71(8-9):866–874, 2009. ISSN 1364-6826. doi: 10.1016/j.jastp.2009.03.011.

N. J. Mitchell, P. J. S. Williams, A. G. Beard, G. R. Buesnel, and H. G. Muller. Non-linear planetary tidal wave interactions in the lower thermosphere observed by meteor radar. *Annales Geophysicae-Atmospheres Hydrospheres and Space Sciences*, 14(3):364–366, Mar 1996. ISSN 0992-7689.

N. J. Mitchell, D. Pancheva, H. R. Middleton, and M. E. Hagan. Mean winds and tides in the arctic mesosphere and lower thermosphere. *Journal of Geophysical Research-Space Physics*, 107(A1), 2002.

NJ Mitchell and VSC Howells. Vertical velocities associated with gravity waves measured in the mesosphere and lower thermosphere with the EISCAT VHF radar. *Annales Geophysicae-Atmospheres Hydrospheres and Space Sciences*, 16(10):1367–1379, OCT 1998. ISSN 0992-7689. 8th EISCAT Scientific Workshop, LEICESTER, ENGLAND, JUN 23-27, 1997.

R. J. Morris, A. R. Klekociuk, and D. A. Holdsworth. Low latitude 2-day planetary wave impact on austral polar mesopause temperatures: revealed by a January diminution in PMSE above Davis, Antarctica. *Geophysical Research Letters*, 36, 2009. ISSN 0094-8276.

H. G. Muller. Long-period meteor wind oscillations. *Philosophical Transactions of the Royal Society of London Series a-Mathematical and Physical Sciences*, 271(1217):585–598, 1972.

H. G. Muller and L. Nelson. Traveling quasi 2-day wave in meteor region. *Journal of Atmospheric and Terrestrial Physics*, 40(6):761–766, 1978. ISSN 0021-9169.

W. A. Norton and J. Thuburn. The two-day wave in a middle atmosphere GCM. *Geophysical Research Letters*, 23(16):2113–2116, 1996.

S. Nozawa, S. Imaida, A. Brekke, C. M. Hall, A. Manson, C. Meek, S. Oyama, K. Dobashi, and R. Fujii. The quasi 2-day wave observed in the polar mesosphere. *Journal of Geophysical Research-Atmospheres*, 108(D2), 2003a.

S. Nozawa, H. Iwahashi, A. Brekke, C. M. Hall, C. Meek, A. Manson, S. Oyama, Y. Murayama, and R. Fujii. The quasi 2-day wave observed in the polar mesosphere: Comparison of the characteristics observed at Tromso and Poker Flat. *Journal of Geophysical Research-Atmospheres*, 108(D24), 2003b.

S. Nozawa, A. Brekke, S. Maeda, T. Aso, C. M. Hall, Y. Ogawa, S. C. Buchert, J. Rottger, A. D. Richmond, R. Roble, and R. Fujii. Mean winds, tides, and quasi-2 day wave in the polar lower thermosphere observed in European Incoherent Scatter (EISCAT) 8 day run data in November 2003. *Journal of Geophysical Research-Space Physics*, 110(A12), 2005.

D. Offermann, P. Hoffmann, P Knieling, R. Koppmann, J. Oberheide, D. M. Riggin, V. M. Tunbridge, and W. Steinbrecht. Quasi-two day waves in the summer mesosphere: Triple structure of amplitudes and long-term development. *Journal of Geophysical Research-Atmospheres*, 2011. doi: 10.1029/2010JD014801. in press.

S. E. Palo and S. K. Avery. Observations of the quasi-two-day wave in the middle and lower atmosphere over Christmas Island. *Journal of Geophysical Research-Atmospheres*, 101 (D8):12833–12846, 1996.

S. E. Palo, R. G. Roble, and M. E. Hagan. Middle atmosphere effects of the quasi-two-day wave determined from a General Circulation Model. *Earth Planets and Space*, 51(7-8): 629–647, 1999. International Symposium on Dynamics and Structure of the Mesopause Region MAR 16-21, 1998 KYOTO UNIV, KYOTO, JAPAN.

S. E. Palo, J. M. Forbes, X. Zhang, J. M. Russell, and M. G. Mlynczak. An eastward propagating two-day wave: Evidence for nonlinear planetary wave and tidal coupling in the mesosphere and lower thermosphere. *Geophysical Research Letters*, 34(7), 2007a. Times Cited: 2.

S. E. Palo, J. M. Forbes, X. Zhang, J. M. Russell, and M. G. Mlynczak. An eastward propagating two-day wave: Evidence for nonlinear planetary wave and tidal coupling in the mesosphere and lower thermosphere. *Geophysical Research Letters*, 34(7), 2007b. ISSN 0094-8276. doi: 10.1029/2006GL027728.

D. Pancheva, N. J. Mitchell, A. H. Manson, C. E. Meek, C. Jacobi, Y. Portnyagin, E. Merzlyakov, W. K. Hocking, J. MacDougall, W. Singer, K. Igarashi, R. R. Clark, D. M. Riggin, S. J. Franke, D. Kurschner, A. N. Fahrutdinova, A. M. Stepanov, B. L. Kashcheyev, A. N. Oleynikov, and H. G. Muller. Variability of the quasi-2-day wave observed in the MLT region during the PSMOS campaign of June-August 1999. *Journal of Atmospheric and Solar-Terrestrial Physics*, 66(6-9):539–565, 2004. International Symposium on the Dynamics and Chemistry of the MLT Region OCT 04-08, 2002 Foz do Iguacu, BRAZIL.

D. V. Pancheva, A. G. Beard, and N. J. Mitchell. Nonlinear interactions between planetary waves in the mesosphere/lower-thermosphere region. *Journal of Geophysical Research*, 105(A1):157 – 170, 2000.

L. Pfister. Baroclinic instability of easterly jets with applications to the summer mesosphere. *Journal of the Atmospheric Sciences*, 42(4):313–330, 1985.

A. Phillips. Simultaneous observations of the quasi 2-Day wave at Mawson, Antarctica, and Adelaide, South-Australia. *Journal of Atmospheric and Terrestrial Physics*, 51(2): 119–124, 1989.

R. A. Plumb. Baroclinic instability of the summer mesosphere - a mechanism for the quasi-2-day wave. *Journal of the Atmospheric Sciences*, 40(1):262–270, 1983.

R. A. Plumb, R. A. Vincent, and R. L. Craig. The quasi-2-day wave event of January 1984 and its impact on the mean mesospheric circulation. *Journal of the Atmospheric Sciences*, 44(20):3030–3036, 1987.

A. J. Prata. The 4-day wave. *Journal of the Atmospheric Sciences*, 41(1):150–155, 1984.

D. M. Riggin, R. S. Lieberman, R. A. Vincent, A. H. Manson, C. E. Meek, T. Nakamura, T. Tsuda, and Y. I. Portnyagin. The 2-day wave during the boreal summer of 1994. *Journal of Geophysical Research-Atmospheres*, 109(D8), 2004.

C. D. Rodgers and A. J. Prata. Evidence for a traveling 2-day wave in the middle atmosphere. *Journal of Geophysical Research-Oceans and Atmospheres*, 86(NC10):9661–9664, 1981.

M. Rojas and W. Norton. Amplification of the 2-day wave from mutual interaction of global rossby-gravity and local modes in the summer mesosphere. *Journal of Geophysical Research-Atmospheres*, 112(D12114), 2007.

M. L. Salby. Rossby normal modes in nonuniform background configurations, part 1: Simple fields. *Journal of the Atmospheric Sciences*, 38(9):1803–1826, 1981a.

M. L. Salby. Rossby normal modes in nonuniform background configurations, part 2: Equinox and solstice conditions. *Journal of the Atmospheric Sciences*, 9(9):1827–1840, 1981b.

M. L. Salby. Sampling theory for asynoptic satellite-observations .2. fast fourier synoptic mapping. *Journal of the Atmospheric Sciences*, 39(11):2601–2614, 1982a. ISSN 0022-4928.

M. L. Salby. Sampling theory for asynoptic satellite-observations .1. space-time spectra, resolution, and aliasing. *Journal of the Atmospheric Sciences*, 39(11):2577–2600, 1982b. ISSN 0022-4928.

M. L. Salby. Survey of planetary-scale travelling waves - the state of theory and observations. *Reviews of Geophysics*, 22(2):209–236, 1984.

M. L. Salby and P. F. Callaghan. Seasonal amplification of the 2-day wave: Relationship between normal mode and instability. *Journal of the Atmospheric Sciences*, 58(14):1858–1869, 2001.

M. L. Salby and P. F. Callaghan. Interaction of the 2-day wave with solar tides. *Journal of Geophysical Research-Atmospheres*, 113(D14), 2008.

M. L. Salby and R. G. Roper. Long-period oscillations in the meteor region. *Journal of the Atmospheric Sciences*, 37(1):237–244, 1980.

M.L. Salby. *Fundamentals of atmospheric physics*, volume 61 of *International geophysics series*. Academic Press, illustrated edition, 1996. ISBN 9780126151602.

D. J. Sandford and N. J. Mitchell. Lunar tides in the mesosphere over Ascension Island (8 degrees S, 14.4 degrees W). *Annales Geophysicae*, 25(1):9–12, 2007. ISSN 0755-0685.

D. J. Sandford, H. G. Muller, and N. J. Mitchell. Observations of lunar tidesin the mesosphere and lower thermosphere at Arctic and middle latitudes. *Atmospheric Chemistry and Physics*, 6:4117–4127, 2006.

D. J. Sandford, N. J. Mitchell, R. A. Vincent, and D. J. Murphy. The lunar tides in the Antarctic mesosphere and lower thermosphere. *Journal of Atmospheric and Solar-Terrestrial Physics*, 69(17-18):2219–2237, 2007. ISSN 1364-6826. doi: 10.1016/j.jastp.2007.04.010.

D. J. Sandford, M. J. Schwartz, and N. J. Mitchell. The wintertime two-day wave in the polar stratosphere, mesosphere and lower thermosphere. *Atmospheric Chemistry and Physics*, 8(3):749–755, 2008.

M. R. Schoeberl, A. R. Douglass, E. Hilsenrath, P. K. Bhartia, R. Beer, J. W. Waters, M. R. Gunson, L. Froidevaux, J. C. Gille, J. J. Barnett, P. E. Levelt, and P. DeCola. Overview of the EOS Aura mission. *Ieee Transactions on Geoscience and Remote Sensing*, 44(5):1066–1074, 2006.

M. J. Schwartz, A. Lambert, G. L. Manney, W. G. Read, N. J. Livesey, L. Froidevaux, C. O. Ao, P. F. Bernath, C. D. Boone, R. E. Cofield, W. H. Daffer, B. J. Drouin, E. J. Fetzer, R. A. Fuller, R. F. Jarnot, J. H. Jiang, Y. B. Jiang, B. W. Knosp, K. Kruger, J. L. F. Li, M. G. Mlynczak, S. Pawson, J. M. Russell, M. L. Santee, W. V. Snyder, P. C. Stek, R. P. Thurstans, A. M. Tompkins, P. A. Wagner, K. A. Walker, J. W. Waters, and D. L. Wu. Validation of the Aura microwave limb sounder temperature and geopotential height measurements. *Journal of Geophysical Research-Atmospheres*, 113(D15), 2008.

H. Teitelbaum and F. Vial. On tidal variability induced by nonlinear-interaction with planeatry-waves. *Journal of Geophysical Research-Space Physics*, 96(A8):14169–14178, 1991. ISSN 0148-0227.

T. Thayaparan, W. K. Hocking, and J. MacDougall. Amplitude, phase, and period variations of the quasi 2-day wave in the mesosphere and lower thermosphere over London, Canada (43 degrees N, 81 degrees W), during 1993 and 1994. *Journal of Geophysical Research-Atmospheres*, 102(D8):9461–9478, 1997.

G. E. Thomas. Is the polar mesosphere the miner's canary of global change? *Thermosphere-Ionosphere-Middle Atmosphere Coupling and Dynamics*, 18(3):149–158, 1995. ISSN 0273-1177.

T. Tsuda, S. Kato, and R. A. Vincent. Long period wind oscillations observed by the Kyoto meteor radar and comparison of the quasi-2-day wave with Adelaide Hf radar observations. *Journal of Atmospheric and Terrestrial Physics*, 50(3):225–230, 1988.

V. M. Tunbridge and N. J. Mitchell. The two-day wave in the Antarctic and Arctic mesosphere and lower thermosphere. *Atmospheric Chemistry and Physics*, 9(17):6377 – 6388, 2009.

Geoffrey K. Vallis. *Atmospheric and Oceanic Fluid Dynamics*. Cambridge University Press, fifth edition, 2010. ISBN 978-0-521-84969-2.

R. L. Walterscheid and R. A. Vincent. Tidal generation of the phase-locked 2-day wave in the Southern Hemisphere summer by wave-wave interactions. *Journal of Geophysical Research-Atmospheres*, 101(D21):26567–26576, 1996. ISSN 0148-0227.

W. E. Ward, D. Y. Wang, B. H. Solheim, and G. G. Shepherd. Observations of the two-day wave in WINDII data during January, 1993. *Geophysical Research Letters*, 23(21): 2923–2926, 1996.

J. W. Waters, L. Froidevaux, R. F. Jarnot, W. G. Read, H. M. Pickett, R. S. Harwood, R. E. Cofield, M. J. Filipiak, D. A. Flower, N. J. Livesey, G. L. Manney, H. C. Pumphrey, M. L. Santee, P.H. Siegel, and D. L. Wu. An overview of the EOS MLS experiment. Version 2.0 D-15745, Jet Propulsion Laboratory, 2004.

J. W. Waters, L. Froidevaux, R. S. Harwood, R. F. Jarnot, H. M. Pickett, W. G. Read, P. H. Siegel, R. E. Cofield, M. J. Filipiak, D. A. Flower, J. R. Holden, G. K. K. Lau,

N. J. Livesey, G. L. Manney, H. C. Pumphrey, M. L. Santee, D. L. Wu, D. T. Cuddy, R. R. Lay, M. S. Loo, V. S. Perun, M. J. Schwartz, P. C. Stek, R. P. Thurstans, M. A. Boyles, K. M. Chandra, M. C. Chavez, G. S. Chen, B. V. Chudasama, R. Dodge, R. A. Fuller, M. A. Girard, J. H. Jiang, Y. B. Jiang, B. W. Knosp, R. C. LaBelle, J. C. Lam, K. A. Lee, D. Miller, J. E. Oswald, N. C. Patel, D. M. Pukala, O. Quintero, D. M. Scaff, W. Van Snyder, M. C. Tope, P. A. Wagner, and M. J. Walch. The Earth Observing System Microwave Limb Sounder (EOS MLS) on the Aura satellite. *Ieee Transactions on Geoscience and Remote Sensing*, 44(5):1075–1092, 2006.

D. L. Wu, P. B. Hays, W. R. Skinner, A. R. Marshall, M. D. Burrage, R. S. Lieberman, and D. A. Ortland. Observations of the quasi 2-day wave from the High-Resolution Doppler Imager on UARS. *Geophysical Research Letters*, 20(24):2853–2856, 1993.

D. L. Wu, E. F. Fishbein, W. G. Read, and J. W. Waters. Excitation and evolution of the quasi-2-day wave observed in UARS/MLS temperature measurements. *Journal of the Atmospheric Sciences*, 53(5):728–738, 1996.

D. L. Wu, M. J. Schwartz, J. W. Waters, V. Limpasuvan, Q. A. Wu, and T. L. Killeen. Mesospheric doppler wind measurements from Aura Microwave Limb Sounder (MLS). *Advances in Space Research*, 42(7):1246–1252, 2008.

D. L. Wu, P. B. Hays, and W. R. Skinner. A least-squares method for spectral-analysis of space-time series. *Journal of the Atmospheric Sciences*, 52(20):3501–3511, OCT 15 1995. ISSN 0022-4928.

Y. Yamada. Horizontal structure of the geomagnetic 2-day variation. *Journal of Geophysical Research-Space Physics*, 114, 2009. ISSN 0148-0227.

P. T. Younger, I. Astin, D. J. Sandford, and N. J. Mitchell. The sporadic radiant and distribution of meteors in the atmosphere as observed by VHF radar at Arctic, Antarctic and equatorial latitudes. *ANNALES GEOPHYSICAE*, 27(7):2831–2841, 2009. ISSN 0992-7689.